ISSN 2518-7198 (Print)
ISSN 2663-5089 (Online)

BULLETIN
OF THE KARAGANDA UNIVERSITY

PHYSICS
Series

2026 • Volume 31 • Issue 2(122)

ISSN 2663-5089 (Online)
ISSN 2518-7198 (Print)
Индексі 74616
Индекс 74616

ҚАРАҒАНДЫ УНИВЕРСИТЕТІНІҢ ХАБАРШЫСЫ

ВЕСТНИК КАРАГАНДИНСКОГО УНИВЕРСИТЕТА

BULLETIN OF THE KARAGANDA UNIVERSITY

ФИЗИКА сериясы

Серия ФИЗИКА

PHYSICS Series

2026

31-том • 2(122)-шығарылым
Том 31 • Выпуск 2(122)
Volume 31 • Issue 2(122)

1996 жылдан бастап шығады
Издается с 1996 года
Founded in 1996

Жылына 4 рет шығады
Выходит 4 раза в год
Published 4 times a year

Қарағанды / Караганда / Karaganda
2026

Баспагер: **«Академик Е.А. Бөкетов атындағы Қарағанды ұлттық зерттеу университеті» КеАҚ**
Мекенжайы: 100024, Қазақстан, Қарағанды қ., Университет к-сі, 28
E-mail: vestnikku@gmail.com; karabekova71@mail.ru. *Web-site*: https://phs.buketov.edu.kz

Қарағанды университетінің хабаршысы. «Физика» сериясы. — 2026. — 31-т., 2(122)-шығ. — 99 б. — ISSN 2518-7198 (Print). ISSN 2663-5089 (Online).

Меншік иесі: «Академик Е.А. Бөкетов атындағы Қарағанды ұлттық зерттеу университеті» КеАҚ.

Қазақстан Республикасы Мәдениет және ақпарат министрлігінде тіркелген. 05.12.2025 ж. № KZ56VPY00135985 қайта есепке қою туралы куәлігі.

Басуға 23.06.2026 ж. қол қойылды. Пішімі 60×84 1/8. Қағазы офсеттік. Көлемі 12,37 б.т. Таралымы 200 дана. Бағасы келісім бойынша. Тапсырыс № 70.

«Академик Е.А. Бөкетов атындағы Қарағанды ұлттық зерттеу университеті» КеАҚ баспасының баспаханасында басылып шықты.
100024, Қазақстан, Қарағанды қ., Университет к-сі, 28. Тел. (7212) 35-63-16.
E-mail: printed@karnu-buketov.edu.kz

Издатель: **НАО «Карагандинский национальный исследовательский университет имени академика Е.А. Букетова»**

Адрес: 100024, Казахстан, г. Караганда, ул. Университетская, 28
E-mail: vestnikku@gmail.com; karabekova71@mail.ru. *Web-site*: https://phs.buketov.edu.kz

Вестник Карагандинского университета. Серия «Физика». — 2026. — Т. 31, вып. 2(122). — 99 с. — ISSN 2518-7198 (Print). ISSN 2663-5089 (Online).

Собственник: НАО «Карагандинский национальный исследовательский университет имени академика Е.А. Букетова».

Зарегистрирован Министерством культуры и информации Республики Казахстан. Свидетельство о постановке на переучет № KZ56VPY00135985 от 05.12.2025 г.

Подписано в печать 23.06.2026 г. Формат 60×84 1/8. Бумага офсетная. Объем 12,37 п.л. Тираж 200 экз. Цена договорная. Заказ № 70.

Отпечатано в типографии издательства НАО «Карагандинский национальный исследовательский университет им. акад. Е.А. Букетова». 100024, Казахстан, г. Караганда, ул. Университетская, 28.
Тел. (7212) 35-63-16. E-mail: printed@karnu-buketov.edu.kz

Publisher: **NLC "Karaganda National Research University named after academician Ye.A. Buketov"**
Postal address: 28, Universitetskaya Str., Karaganda, 100024, Kazakhstan
E-mail: vestnikku@gmail.com; karabekova71@mail.ru. *Web-site*: https://phs.buketov.edu.kz

Bulletin of the Karaganda University. "Physics" Series. — 2026. — Vol. 31, Iss. 2(122). — 99 p. — ISSN 2518-7198 (Print). ISSN 2663-5089 (Online).

Proprietary: NLC "Karaganda National Research University named after academician Ye.A. Buketov".

Registered by the Ministry of Culture and Information of the Republic of Kazakhstan. Rediscount certificate No. KZ56VPY00135985 dated 05.12.2025.

Signed in print 23.06.2026. Format 60×84 1/8. Offset paper. Volume 12,37 p.sh. Circulation 200 copies. Price upon request. Order № 70.

Printed in the Publishing house of NLC "Karaganda National Research University named after academician Ye.A. Buketov". 28 University St., Karaganda 100024, Kazakhstan. Tel. (7212) 35-63-16.
E-mail: printed@karnu-buketov.edu.kz

МАЗМҰНЫ – СОДЕРЖАНИЕ – CONTENTS

КОНДЕНСАЦИЯЛАНҒАН КҮЙДІҢ ФИЗИКАСЫ
ФИЗИКА КОНДЕНСИРОВАННОГО СОСТОЯНИЯ
PHYSICS OF THE CONDENSED MATTER

ТЕХНИКАЛЫҚ ФИЗИКА
ТЕХНИЧЕСКАЯ ФИЗИКА
TECHNICAL PHYSICS

ЖЫЛУФИЗИКАСЫ ЖӘНЕ ТЕОРИЯЛЫҚ ЖЫЛУТЕХНИКАСЫ
ТЕПЛОФИЗИКА И ТЕОРЕТИЧЕСКАЯ ТЕПЛОТЕХНИКА
THERMOPHYSICS AND THEORETICAL THERMOENGINEERING

Article

UDC 621.315.592, 621.03

https://doi.org/10.31489/2026PH2/6-12

Received: 13.01.2026
Accepted: 13.03.2026

E.R. Hasanov[1, 2], Sh.G. Khalilova[2, 1✉], R.K. Mustafayeva[1]

[1]*Baku State University, Baku, Azerbaijan;*
[2]*Institute of Physics, Baku, Azerbaijan*

Unstable Waves in Two-Valley Semiconductors in the Presence of a Temperature Gradient and External Electric and Magnetic Field

A theory of unstable wave excitation in a two-valley semiconductor subjected to a temperature gradient and constant external electric and magnetic fields is developed. The effects of the external electric field, the temperature gradient, the magnetic field generated within the sample by hydrodynamic motion, and the electric field arising from charge-carrier redistribution are taken into account. It is shown that the sample size plays an important role in the excitation of unstable waves. The frequency of hydrodynamic waves is shown to be twice that of the thermomagnetic waves excited in the sample. Analytical expressions for the frequencies and growth rates of the unstable waves are obtained. Analytical conditions for the external magnetic field required to excite hydrodynamic unstable waves are derived, and the ranges of the external electric field corresponding to wave excitation are determined. It is established that the transition time of charge carriers from the lower valley to the upper valley is shorter than the transition time from the upper valley to the lower valley. The analysis is based on a linear theory and assumes that carrier mobilities differ only slightly from their equilibrium values. For the first time, the electric field generated within the semiconductor is taken into account, demonstrating the feasibility of developing new Gunn-effect devices, including generators and amplifiers. The proposed mechanisms are consistent with available experimental data on the Gunn effect. It is also shown that the combined action of a temperature gradient and an external magnetic field can facilitate the design and optimization of high-frequency devices and amplifiers.

Keywords: thermomagnetic waves, growth, frequency, increment, dynamics, carrier concentration, characteristic frequencies, characteristic electric field, Gunn effect, semiconductor

✉*Corresponding author*: Khalilova, Shahla, shahlaganbarova@gmail.com

Introduction

In GaAs semiconductors, the energy spectrum of charge carriers at a wave vector value $k = 0$ has two minima. Between the two minima, the energy gap has a value of $\Delta = 0.36$ eV. In the presence of an external electric field $\vec{E}$, charge carriers (in this case, electrons) receive energy from the electric field in order $\sim eEl$ (e refer to the elementary charge, l refer to the mean free path) and, using this energy, move into a high energy band. The mobility of charge carriers is $\mu_1 >> \mu_2$ (because $m_1^* << m_2^*$).

As one moves from the first valley to the second, the total current decreases. At certain values of the external electric field, the sample begins to emit energy at a certain frequency. This effect was first observed by

the English scientist Gunn and is therefore called the Gunn effect [1]. In 1963, he discovered that the electric field $E \sim 2 \div 3 \cdot 10^3$ V/cm causes oscillations in the sample at certain values.

The electric current E_{kr}, following the electric field value $E \geq E_{kr}$, oscillates at a frequency of $\omega \sim 10^9 \div 10^{11}$ Hz. When the external electric field becomes greater than E_{kr} of the sample, it begins to emit energy, and the sample becomes an energy source. Based on the Gunn effect, amplifiers and generators were developed, which are called Gunn devices. The theory of the Gunn effect was developed in [1–4], and the physical basis of the effect was clarified. The energy spectrum of charge carriers in GaAs at Muller indices of [100] has the form (Fig. 1).

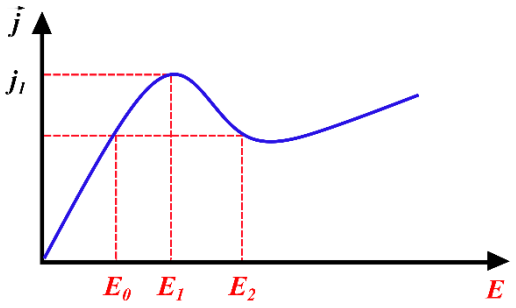

Figure 1. A plot of electric current as a function of the electric field

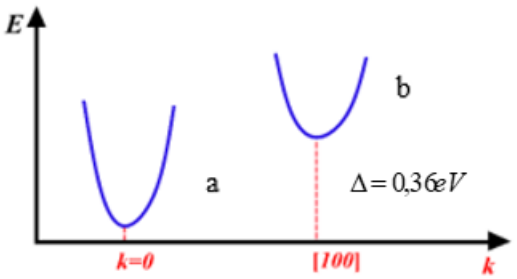

Figure 2. A plot of the energy of charge carriers as a function of the wave vector

The GaAs sample is assumed to be pure and free of impurities. Therefore, electrons are the only charge carriers, and their total concentration remains constant

$$n = n_1 + n_2 = const\ . \tag{1}$$

The Gunn effect theory in the presence of an external magnetic field was first developed in [5] and it was proven that if there is an external magnetic field $\vec{H}$, current oscillations begin at lower electric field values, i.e., $E \sim 2 \div 3 \cdot 10^2$ V/cm.

This is due to the fact that electrons in the presence of a magnetic field twist and are quickly distributed non-uniformly throughout the sample. In 1963, it was demonstrated in [6] that the hydrodynamic motion of charge carriers in the presence of a temperature gradient generates a new wave, called a thermomagnetic wave. In [6] the frequency of the thermomagnetic wave was calculated and the cause of its occurrence was determined.

In [7–9] it was demonstrated that thermomagnetic waves can be excited in solids, and this wave does not interact with sound waves. In [6] an expression for the effective electric field in a medium was obtained.

$$\vec{E}^* = \vec{E} + \frac{[\upsilon H]}{c} + \frac{T}{c}\frac{\nabla n}{n}. \tag{2}$$

Here $\vec{E}$ refer to the external electric field, refer to the electric field generated as a result of hydrodynamic movements with velocity $\vec{\upsilon}$, and $\frac{T}{c}\frac{\nabla n}{n}$ refer to the electric field due to the redistribution of charge carriers within the medium.

The Gunn effect was studied in the presence of an electric field E. A theoretical study in the presence of external electric and magnetic fields was conducted in [5].

However, no theoretical study has been conducted taking electric fields (2) into account.

In this theoretical work, we will investigate the oscillations of physical quantities in GaAs semiconductors, taking into account electric fields (2), the presence of a constant temperature gradient, and an external magnetic field H_0. We will analyze the conditions for the emergence of unstable waves within the sample and the relationship of the excited waves to the thermomagnetic wave.

Materials and Methods

Under the influence of external forces (this is $\vec{H}, \vec{E}, \vec{\nabla}T$), the charge carrier moves from the first valley (Fig. 2) to the second valley in time τ_{12}, and the reverse transition from the second valley to the first valley takes time τ_{21}. Therefore, the continuity equation in each valley is [9]:

$$\begin{aligned} &\frac{\partial n_1}{\partial t} + \operatorname{div} \vec{j}_1 = \frac{n_1}{\tau_{12}}; \\ &\frac{\partial n_2}{\partial t} + \operatorname{div} \vec{j}_2 = \frac{n_2}{\tau_{21}}. \end{aligned} \tag{3}$$

Considering that the total concentration of charge carriers is constant, this is

$$n = n_1 + n_2 = const; \tag{4}$$

$$n_1' = -n_2', \tag{5}$$

$\vec{j}_1$ and $\vec{j}_2$ the current flow density in both valleys [9]:

$$\begin{aligned} \vec{j}_1 &= n_1\mu_1 E^* + n_1\mu_1'\left[E^*\vec{H}\right] - \alpha_1\left[\vec{\nabla}T\vec{H}\right] - \alpha_1'\vec{\nabla}T; \\ \vec{j}_2 &= n_2\mu_2 E^* + n_2\mu_2'\left[E^*\vec{H}\right] - \alpha_2\left[\vec{\nabla}T\vec{H}\right] - \alpha_2'\vec{\nabla}T. \end{aligned} \tag{6}$$

The relationship between the magnetic field and the electric field is determined by Maxwell's equation

$$\frac{\partial \vec{H}}{\partial t} = -c \operatorname{rot} E^*, \tag{7}$$

c refers to speed of light.

Taking into account (4) from (3), we easily find

$$\operatorname{div} \vec{j} = \left(\frac{1}{\tau_{12}} - \frac{1}{\tau_{21}}\right) n_1'. \tag{8}$$

Where $\vec{j} = \vec{j}_1 + \vec{j}_2$.

Substituting (6) into (8), we easily obtain:

$$\begin{aligned} &\operatorname{div}\left\{\sigma\vec{E}^* + \frac{\sigma}{c}\left[vH\right] + \frac{T}{e}\left(\frac{\sigma_1}{n_{10}} - \frac{\sigma_2}{n_{20}}\right)\nabla n_1 + \sigma'\left[E^*H\right] + \frac{T}{e}\left(\frac{\sigma_1}{n_{10}} - \frac{\sigma_2}{n_{20}}\right)\left[\nabla n_1 H\right] - \alpha\nabla T - \alpha'\left[\vec{\nabla}T\vec{H}\right]\right\} = \\ &= \left(\frac{1}{\tau_{12}} - \frac{1}{\tau_{21}}\right) n_1'. \end{aligned} \tag{9}$$

Where $\sigma = \left(\frac{n_1\mu_1 + n_2\mu_2}{e}\right), \sigma_1 = \frac{n_1\mu_1}{e}, \sigma_2 = \frac{n_2\mu_2}{e}, \sigma' = \left(\frac{n_1\mu_1' + n_2\mu_2'}{e}\right), \alpha = \alpha_1 + \alpha_2, \alpha' = \alpha_1' + \alpha_2'$.

Determining from Maxwell's equations

$$\vec{j}_1 + \vec{j}_2 = \frac{\varepsilon c}{4\pi} \operatorname{rot} \vec{H}.$$

Let's put $\vec{j}_1$ and $\vec{j}_2$ from (6), and we easily obtain an equation of the following type:

$$\vec{x} = \vec{a} + \left(\vec{b}\vec{x}\right), \vec{x} = \vec{E}^*. \tag{10}$$

Due to the cumbersome nature of the expression $\vec{a}$ and $\vec{b}$, we will not write out the vectors.

By multiplying equation (10) once as a vector $\vec{E}^*$ and a second time as a scalar $\vec{E}^*$ with a weak magnetic field (this is $\mu_{10}H_0 << c$), we easily obtain

$$\vec{E}^* = -\frac{\left[\upsilon H\right]}{c} - \Lambda'\left[\nabla T H\right] + \frac{c}{4\pi\sigma} \operatorname{rot} H + \frac{T}{e}\left(\frac{1}{n_{10}} - \frac{1}{n_{20}}\right)\nabla n' + \Lambda\vec{\nabla}T. \tag{11}$$

Where $\Lambda' = \frac{\alpha'\sigma - \sigma'\alpha}{\sigma^2}$ refer to Nernst-Ettingshausen coefficient

$$\Lambda = \frac{\alpha}{\sigma}, \alpha = \alpha_1 + \alpha_2, \alpha' = \alpha_1' + \alpha_2';$$

$$\vec{E}^* = \frac{T}{e\gamma}\left(\frac{1}{n_{10}} - \frac{1}{n_{20}}\right) i\vec{k} n_1' + \Lambda \nabla T \frac{\vec{E}_0 E^*}{E_0^2};$$

$$\vec{E}_0 E^* = \frac{T}{e\gamma}\left(\frac{1}{n_{10}} - \frac{1}{n_{20}}\right) i\vec{k}\vec{E}_0 n_1' + \frac{\Lambda \vec{\nabla} T \vec{E}_0}{E_0^2} \vec{E}_0 E^*; \tag{12}$$

$$\gamma = 1 + \frac{\vec{k}\vec{\upsilon}}{\omega} - \frac{2\omega_T}{\omega} - i\frac{c^2 k^2}{4\pi\sigma}.$$

To obtain the dispersion equation for the frequency of the excited waves inside the sample, equations (9, 10, 11) must be solved simultaneously.

We linearize equations (9, 10, 11) with respect to the physical quantities as follows:

$$\vec{E}^* = E_0^* + E^{*'}, E^{*'} << E_0^*, \vec{H} = \vec{H}_0 + \vec{H}', \vec{H}' << \vec{H}_0, n_1 = n_{10} + n_1', n_1' << n_{10} \tag{13}$$

and the total current flow

$$\vec{j} = \vec{j}_0 + \vec{j}'.$$

We select the following coordinate system: $\vec{H}_0 = \vec{k} H_{oz}, \vec{E}_o = \vec{i} E_{0x}, \vec{\nabla} T = \vec{i} \nabla_x T$, $\vec{i}, \vec{k}$ — unit vector.

Considering conditions (13) from (9, 10, 11), after algebraic calculations:

$$j_x' = \sigma_0 E_x^{*'} + E_0 \sigma' + \frac{\sigma_0}{c}\left(\upsilon_{0y} H_z' - \upsilon_{0z} H_y'\right) + E_1 i\left(\frac{\sigma_1}{n_{10}} - \frac{\sigma_2}{n_{20}}\right) n_1' + \sigma_0' E_y^{*'} +$$
$$+ E_1 \frac{k_y}{k_x} i\left(\frac{\sigma_1}{n_{10}} - \frac{\sigma_2}{n_{20}}\right) H_0 n' - \Lambda\delta\nabla_x T \frac{E_x^{*'}}{E_0}, \tag{14}$$

$$E_1 = \frac{T}{e} k_x;$$

$$j_y' = \sigma E_y^{*'} - \frac{\sigma_0 H_0}{c}\upsilon_x' - \frac{\sigma' H_0}{c}\upsilon_{x0} + E_1 \frac{k_y}{k_x} i\left(\frac{\sigma_1}{n_{10}} - \frac{\sigma_2}{n_{20}}\right) n_1' + \sigma_0' E_*^{*'} - E_1\left(\frac{\sigma_1}{n_{10}} - \frac{\sigma_2}{n_{20}}\right) n_1' = 0; \tag{15}$$

$$j_z' = \sigma E^{*'} + \frac{\sigma_0}{c}\left(\upsilon_{x0} H_y' - \upsilon_{y0} H_x'\right) + E_1 \frac{k_z}{k_x} i\left(\frac{\sigma_1}{n_{10}} - \frac{\sigma_2}{n_{20}}\right) n_1' + \sigma_0' \frac{E_0}{H_0} H_y' - \alpha \nabla_x T H_y' = 0; \tag{16}$$

$$H_x' = \frac{c}{\omega}\left(k_y E_z^{*'} - k_z E_y^{*'}\right),\ H_y' = \frac{c}{\omega}\left(k_z E_x^{*'} - k_x E_z^{*'}\right),\ H_z' = \frac{c}{\omega}\left(k_x E_y^{*'} - k_y E_x^{*'}\right). \tag{17}$$

At

$$H_0 = \frac{c}{\mu_{10}} \frac{L_y}{L_x} \frac{n_{20}}{n_{10}}. \tag{18}$$

The dispersion equation has the form:

$$\left(\Omega + ik_x\upsilon_{10}\right)\omega^2 + \left[\Omega\left(\vec{k}\vec{\upsilon}_0 - 2\omega_T\right) + k_x\upsilon_{10}\frac{c^2k^2}{4\pi\sigma_0} + i\left(k_x\upsilon_{10}\vec{k}\vec{\upsilon}_0 - k_x\upsilon_{10}2\omega_T - \Omega\frac{c^2k^2}{4\pi\sigma}\right) -\right.$$
$$\left. - k_x^2\upsilon_1\upsilon_{oy}\eta\left(\frac{n_{10}}{n_{20}} + i\eta\right)\right]\omega - k_x^2\upsilon_{10}\upsilon_{oy}\left(\frac{n_{10}}{n_{20}} + i\eta\right)\left(\vec{k}\vec{\upsilon}_0 - 2\omega_T - i\frac{c^2k^2}{4\pi\sigma_0}\right) = 0; \tag{19}$$

$$\Omega = k_x\upsilon_1\frac{n_{10}}{n_{20}} - \eta k_x\upsilon_1 - \omega(\tau).$$

At $\vec{k}\vec{\upsilon}_0 = -2\omega_T$

$$\left(\Omega + ik_x\upsilon_{10}\right)\omega^2 + \left[k_x\upsilon_{10}\frac{c^2k^2}{4\pi\sigma_0} - i\left(k_x^2\upsilon_1\upsilon_{0y}\eta^2 + \Omega\frac{c^2k^2}{4\pi\sigma}\right) - k_x^2\upsilon_1\upsilon_{oy}\eta\frac{n_{10}}{n_{20}}\right]\omega - \\ -k_x^2\upsilon_{10}\upsilon_{oy}\left(i\frac{n_{10}}{n_{20}} - i\eta\right)\frac{c^2k^2}{4\pi\sigma_0} = 0. \tag{20}$$

At

$$\frac{c^2k^2}{4\pi\sigma_0}E_0 = k_x\upsilon_{oy}\eta E_1\frac{n_{10}}{n_{20}}. \tag{21}$$

At $\tau_{12} = \frac{\upsilon_{oy}}{E_0\mu_{10}}\frac{4\pi\sigma_0}{c^2k^2}$ solution of (20) is

$$\omega_0 = k_x\upsilon_{0y}\left[\left(\frac{c^2k^2}{\upsilon_{0y}4\pi\sigma}\frac{n_{10}}{2n_{20}}\right)^2 - \frac{E_1}{2E_0}\eta^2\right];$$

$$\omega_1 = k_x\upsilon_{0y}\left(\frac{c^2k^2}{\upsilon_{0y}4\pi\sigma}\frac{n_{10}}{2n_{20}}\right)^{1/2}.$$

This is $\omega_0 < \omega_1$.

In this case, the growing wave of a hydrodynamic nature has a greater increment than the frequency of propagation of this wave.

Results and Discussion

Thus, when a two-valley GaAs semiconductor is exposed to external energy, magnetic fields and a temperature gradient with a specific direction, a hydrodynamic wave is excited instead of a thermomagnetic electromagnetic wave. The excited wave is growing, and with increasing electromagnetic wave frequency, the frequency of this wave increases. The sample size can be any value, and the ratio to the concentrations is $\frac{n_{10}}{n_{20}} > 1$. The transition time from the first valley to the second valley satisfies the condition $\tau_{12} < \tau_{21}$. The magnetic field has specific values and satisfies the condition

$$\mu_{10}H_0 << c.$$

The frequency of hydrodynamic waves is twice that of thermomagnetic waves. The electric field, under increasing conditions of excited waves, has a certain range. During unstable states of the sample, the electric field must exceed a certain characteristic field, this is $E_0 > \Lambda\nabla_x T$.

Conclusion

The direction of the external electric field and the temperature gradient are the same. The direction of the external magnetic field is perpendicular to the electric field of the temperature gradient. All theoretical calculations were performed for oscillations of physical quantities within the sample. Thus, internal instability was theoretically investigated. When oscillations of physical quantities are released externally, that is, when current oscillations in the circuit begin (i.e., external instability) and energy is emitted from the sample, the sample's resistance decreases. To calculate the oscillation frequency during external instability, it is necessary to calculate the impedance with a real frequency and a complex wave vector. This problem requires a different type of theoretical calculation. Taking into account the temperature gradient and external magnetic field simplifies the process of manufacturing high-frequency devices and amplifiers.

References

1 Gunn, J.B. (1964). Current instabilities and potential distribution in GaAs and InP. *Plasma Effects in Solids*, 199–207.

2 Gurevich, L.E. (1963). Thermomagnetic waves and excitation of the magnetic field in nonequlibrium plasmas. *JETP*, 44, 548–555.

3 Sarcan, F., Mutlu, S., Perkitel, I., & Demir, I. (2025). Enhanced light emission characteristic of an InP-waveguided planar InGaAs Gunn diode. *Materials Science in Semiconductor Processing, 197,* 109713. DOI: 10.1016/j.mssp.2025.109713

4 García-Sánchez, S., Pérez, S., Íñiguez-De-la-Torre, I., García-Vasallo, B., & Huo, L. (2025). Avoiding avalanche breakdown in planar GaN Gunn diodes by means of a substrate contact. *Journal of Physics D: Applied Physics, 58*(1), 015112. DOI: 10.1088/1361-6463/ad809

5 Chirkova, L.V., Skubnevsky, E.V., Ermagambetov, K.T., & Arinova, E.T. (2016). Nonliner phenomena and instability in semiconductors. *Bulletin of the University of Karaganda — Physics*, 1, 39–45.

6 Gafel, H.S. (2022). Fractional order study of the impact of a photo thermal wave on a semiconducting medium under magnetic field and thermoplastic theories. *Information Science Letter, 11*, 629–638.

7 Alfven, G., & Felthammar, K. (1967). *Space Electrodynamics*, 2nd ed. Oxford University Press, 156 p.

8 Kong, A. (1990). *Electromagnetic Wave Theory*, 2nd ed. John Wiley&Sons, Inc., New York, 677 p.

9 Hasanov, E.R., Khalilova, Sh.G., & Mustafayeva, R.K. (2021). Instability In Two GaAs Valley Semiconductors In Electric And Magnetic Fields. *International Journal on "Technical and Physical Problems of Engineering", 1*(14), 229–232.

10 Hasanov, E.R., Khalilova, Sh.G., & Mustafayeva, R.K. (2025). Transverse and longitudinal thermomagnetic waves in conducting media. *Bulletin of the University of Karaganda — Physics*, 3, 51–58. DOI: https://doi.org/10.31489/2025ph3/51-58

11 Hasanov, E.R., Khalilova, Sh.G., & Mustafayeva, R.K. (2024). Excitation of transverse and longitudinal thermomagnetic waves in anisotropic conducting media in the presence of a temperature gradient $\vec{\nabla}T$ without an external magnetic field H. *Bulletin of the University of Karaganda — Physics*, 2, 43–52. DOI: https://doi.org/10.31489/2024ph2/43-52

Э.Р. Гасанов, Ш.Г. Халилова, Р.Г. Мустафаева

Температура градиенті және сыртқы электр мен магнит өрістері бар жағдайда екі аңғарлы жартылай өткізгіштердегі тұрақсыз толқындар

Жартылай өткізгіштердің көрсетілген екі аңғарында белгілі бір бағыттағы температура градиенті және белгілі бір бағыттағы сыртқы тұрақты электр және магнит өрістері болған жағдайда қозатын тұрақсыз толқындардың теориясы жасалды. Сыртқы электр өрісінің, температура градиентінің, гидродинамикалық қозғалыстар нәтижесінде үлгі ішінде пайда болатын магнит өрісінің, сондай-ақ заряд тасымалдаушылардың қайта таралуынан туындайтын ішкі электр өрісінің әсерлері ескерілді. Тұрақсыз толқындардың қозуында үлгінің өлшемі маңызды рөл атқаратыны көрсетілді. Гидродинамикалық толқындардың жиілігі аталған үлгі ішінде қозатын термомагниттік толқындардың жиілігінен екі есе жоғары екені дәлелденді. Пайда болатын тұрақсыз толқындардың жиілігі мен өсіміне арналған аналитикалық өрнектер алынды. Гидродинамикалық табиғаттағы тұрақсыз толқындарды қоздыру үшін қажетті сыртқы магнит өрісінің аналитикалық өрнектері анықталды. Бұл толқындарды қоздыруға арналған сыртқы энергетикалық өрістің аралықтары белгіленді. Заряд тасымалдаушылардың төменгі аңғардан жоғарғы аңғарға өту уақыты екінші аңғардан бірінші аңғарға қарағанда қысқа екені айқындалды. Сызықтық теория құрылып, тасымалдаушылардың қозғалғыштығы олардың тепе-теңдік мәндерінен шамалы ғана айырмашылығы бар деп қабылданды. Алғаш рет осы жартылай өткізгіш ішінде туындайтын электр өрісін есепке алу жаңа Ганн аспаптарын, яғни генераторлар мен күшейткіштерді жасау мүмкіндігінің практикалық жүзеге асырылатынын көрсетті. Жұмыста сипатталған мұндай аспаптарды жасау мүмкіндіктері Ганн эффектісі бойынша тәжірибелік деректермен толық сәйкес келеді. Температура градиенті мен сыртқы магнит өрісін ескеру жоғары жиілікті құрылғылар мен күшейткіштерді жасауға мүмкіндік беретіні көрсетілді.

Кілт сөздер: термомагниттік толқындар, өсу, жиілік, инкремент, динамика, тасымалдаушылар концентрациясы, сипаттамалық жиіліктер, сипаттамалық электр өрісі, Ганн эффектісі, жартылай өткізгіш

Э.Р. Гасанов, Ш.Г. Халилова, Р.Г. Мустафаева

Нестабильные волны в двухдолинейных полупроводниках в присутствии температурного градиента и внешнего электрического и магнитного поля

Разработана теория возбуждения неустойчивых волн в присутствии температурного градиента заданного направления, а также внешних постоянных электрического и магнитного полей заданного направления в двух указанных долинах полупроводников. Учтено влияние внешнего электрического поля, температурного градиента, магнитного поля, возникающего внутри образца вследствие гидро-

динамических движений, а также влияние электрического поля, возникающего внутри образца вследствие перераспределения носителей заряда. Показано, что размер образца играет важную роль при возбуждении неустойчивых волн. Доказано, что частота гидродинамических волн в два раза выше частоты термомагнитных волн, возбуждаемых внутри указанного образца. Получены аналитические выражения для частоты и инкремента возникающих неустойчивых волн. Определены аналитические выражения для внешнего магнитного поля, необходимого для возбуждения неустойчивых волн гидродинамической природы. Установлены интервалы внешнего энергетического поля для возбуждения этих волн. Установлено, что переход носителей заряда из нижней долины в верхнюю происходит быстрее, чем переход из второй долины в первую. Построена линейная теория, при этом предполагалось, что подвижности носителей заряда незначительно отличаются от их равновесных значений. Впервые учет электрического поля, генерируемого внутри данного полупроводника, демонстрирует практическую возможность создания новых приборов Ганна, то есть генераторов и усилителей. Возможности создания таких приборов, описанные в работе, полностью согласуются с экспериментальными данными по эффекту Ганна. Показано, что учет температурного градиента и внешнего магнитного поля способствует созданию высокочастотных приборов и усилителей.

Ключевые слова: термомагнитные волны, рост, частота, инкремент, динамика, концентрация носителей, характерные частоты, характерное электрическое поле, эффект Ганна, полупроводник

Information about the authors

Hasanov, Eldar Rasul — PhD in Physics, Associate Professor of Department of Solid State Physics, Baku State University, Leader of Department of Encyclopedia and Terminologyб Institute of Physics, Baku, Azerbaijan; e-mail: egasanov065@gmail.com; ORCID ID: https://orcid.org/0009-0009-6900-6148

Khalilova, Shahla Ganbar (*corresponding author*) — PhD in Physics, Leading researcher of Department of Encyclopedia and Terminology, Institute of Physics, Teacher of Department of Structure of Matter, Baku State University, Baku, Azerbaijan; e-mail: shahlaganbarova@gmail.com; ORCID ID: https://orcid.org/0000-0002-1032-2746

Mustafayeva, Rugiyya Kerem — PhD, Leading teacher, Department of Solid State Physics, Baku State University, Baku, Azerbaijan; e-mail: ruhi-qrk@mail.ru; ORCID ID: https://orcid.org/0009-0005-2342-5399

Article

UDC 669.715:621.357.7:620.3

https://doi.org/10.31489/2026PH2/13-26

Received: 09.03.2026
Accepted: 21.05.2026

K.K. Kombayev, G.S. Moldabayeva✉, Y.A. Kozhakhmetov,
G.K. Uazyrkhanova, Y.Y. Tabiyeva, D.N. Kakimzhanov

D. Serikbayev East Kazakhstan Technical University, Ust-Kamenogorsk, Kazakhstan

Structural and Phase State and Mechanical Properties of PEO Coatings on Al–Si Alloys with Al_2O_3 and SiO_2 Nanoparticles

This paper presents the results of a comprehensive investigation of the structural, phase, and mechanical properties of plasma electrolytic oxidation (PEO) coatings formed on the surface of EN AC-45000 (AlSi6Cu4) aluminium–silicon alloy in an electrolyte containing Al_2O_3 and SiO_2 nanoparticles. The aim of the study was to determine the effect of electrolyte nanomodification on the morphology, phase composition, and microhardness of PEO coatings. The PEO process was carried out in a NaOH-based aqueous electrolyte with the addition of aluminium and silicon oxide nanoparticles. The microstructure and morphology of the coatings were investigated using optical and scanning electron microscopy. The elemental and phase composition was determined by energy-dispersive analysis and X-ray diffraction. The mechanical properties were evaluated by measuring the microhardness using the Vickers method, while the tribological performance was assessed using the ball-on-disk method under dry sliding conditions. The results showed that a two-layer oxide coating was formed on the alloy surface, consisting of a dense inner α-Al_2O_3 barrier layer and a porous outer layer predominantly composed of γ-Al_2O_3. The incorporation of nanoparticles contributed to coating densification, reduced porosity, and promoted a more uniform distribution of micro-arc discharges. After PEO treatment, the surface microhardness increased from 65–80 HV to approximately 245–250 HV, representing more than a threefold increase. The coatings also exhibited a stable tribological response, characterized by a higher yet stable coefficient of friction and improved wear resistance compared to the untreated alloy. These results demonstrate the high potential of nanomodified PEO for enhancing the operational performance of aluminium–silicon alloys.

Keywords: plasma electrolytic oxidation; aluminium–silicon alloy; PEO coating; Al_2O_3 nanoparticles; SiO_2 nanoparticles; microstructure; microhardness

✉Corresponding author: Moldabayeva, Gulzhaz, gmoldabaeva@edu.ektu.kz

Introduction

The development of modern materials and surface treatment technologies plays a key role in improving the performance characteristics of products made of aluminium alloys, which are widely used in the automotive and mechanical engineering industries [1–3]. In recent years, special attention has been paid to plasma-assisted surface treatment methods, one of which is plasma electrolytic oxidation (PEO). This method makes it possible to form strong, wear-resistant, and corrosion-resistant oxide coatings on the surface of aluminium alloys, thereby improving the durability and reliability of structures [4–6].

In recent years, increasing research efforts have been directed toward the development of composite and nanocomposite PEO coatings aimed at further improving functional properties. In particular, the incorporation of ceramic nanoparticles into the electrolyte has been widely investigated as an effective strategy to modify coating growth behavior, discharge characteristics, and final microstructure. Recent studies have demonstrated that the addition of nanoparticles such as Al_2O_3 and SiO_2 can reduce coating porosity, influence discharge intensity, and enhance hardness and corrosion resistance of PEO coatings [7]. For example, it has been shown that nanoparticle-assisted PEO processes can lead to the formation of denser oxide layers with improved tribological performance due to particle incorporation and microstructural refinement.

At present, research in the field of PEO is actively developing; however, there remain a number of open questions related to controlling the structural and phase composition and the service properties of coatings when they are modified with nanoparticles. The addition of Al_2O_3 and SiO_2 nanoparticles to the electrolyte makes it possible to significantly alter the microstructure and porosity of the oxide layer and, consequently, its mechanical and tribological characteristics [8]. Two main approaches are typically distinguished in nano-

particle-assisted PEO processing: ex situ and in situ methods. In the ex situ approach, pre-synthesized nanoparticles are introduced into the electrolyte and incorporated into the coating during plasma discharges, whereas in the in situ approach, nanoparticles or reinforcing phases are formed directly during plasma-chemical reactions in the discharge channels. Comparative studies indicate that both approaches influence coating growth kinetics, discharge behavior, and phase formation, although the efficiency of particle incorporation depends on electrolyte composition, particle size, and electrical regime parameters [9]. Despite the considerable interest in this issue, the literature lacks comprehensive data on the effect of such nanocomposites on PEO coatings of aluminium–silicon alloys, particularly in the case of the EN AC-45000 (AlSi6Cu4) alloy.

The relevance of the topic is determined by both its theoretical and practical significance. Understanding the mechanisms governing the formation of two-layer coatings and the influence of nanoparticles on phase composition is important not only for advancing fundamental knowledge in surface engineering but also for developing materials with enhanced performance for industrial applications. The selection of the EN AC-45000 alloy is motivated by its widespread use and its typical aluminium–silicon microstructure, which makes the research results applicable to a range of technologically important aluminium alloys [10–13].

In view of the above, the aim of this work is to investigate the structure, phase composition, and microhardness of Al–Si alloys in the initial state and after PEO treatment of the AlSi6Cu4 alloy surface with the addition of nanoparticles.

Thus, conducting studies on the structural and phase state as well as the mechanical properties of PEO coatings on Al–Si alloys modified with Al_2O_3 and SiO_2 nanoparticles is a timely and relevant research direction, capable of contributing both to the development of the scientific foundation and to the practical application of surface treatment of aluminium materials.

Materials and Methods

Studies of the structure, morphology, and mechanical properties of PEO coatings on aluminium alloys were carried out at the VERITAS Center of Excellence and the Smart Engineering Competence Center of the D. Serikbayev East Kazakhstan Technical University Research Center. A specially prepared 10 wt.% aqueous NaOH solution was used as the electrolyte, providing mild passivation of the aluminium surface and high electrical conductivity of the solution, which contributed to the stable formation of oxide coatings in the plasma electrolytic regime. It should be noted that the indicated concentration corresponds to 100 g/L; however, the effective chemical activity of the electrolyte was controlled by continuous cooling and intensive circulation, which significantly reduced local overheating and suppressed excessive chemical dissolution of the aluminium substrate. In addition, the rapid formation of an initial barrier oxide film under applied voltage limited direct contact between the metal and the alkaline solution, thereby preventing catastrophic etching prior to the onset of micro-arc discharges. Such conditions ensured a transition from conventional anodic oxidation to the plasma electrolytic regime within a short time.

Plasma electrolytic oxidation with the addition of Al_2O_3 and SiO_2 nanoparticles was carried out using an experimental setup (Fig. 1*a*). The discharge system consisted of an aluminium alloy anode and a cathodic container filled with the electrolyte, ensuring a closed electrical circuit between the sample and the electrolyte. A pulsed power supply with a wide range of current, voltage, and pulse frequency control was used, which made it possible to optimize the discharge regime for obtaining uniform and structurally dense oxide coatings [14].

The process (Fig. 1*b*) was characterized by significant heat generation in the discharge zone, which required continuous circulation of the electrolyte. This hydrodynamic regime also contributed to stabilizing the chemical environment near the sample surface and preventing localized alkaline attack. The circulation was provided by a hydrodynamic generator and a pump, ensuring effective mixing of the solution, dispersion of nanoparticles throughout the electrolyte volume, and a stable PEO discharge regime. To prevent aggregation and sedimentation of Al_2O_3 and SiO_2 nanoparticles, continuous electrolyte circulation and hydrodynamic mixing were maintained throughout the entire process. Prior to treatment, the electrolyte containing nanoparticles was mechanically stirred to achieve a homogeneous suspension. These measures ensured uniform nanoparticle distribution and minimized particle agglomeration during the oxidation process. Electrolyte cooling was carried out in a heat exchanger with external heat removal, which made it possible to maintain the operating temperature within a specified range [15].

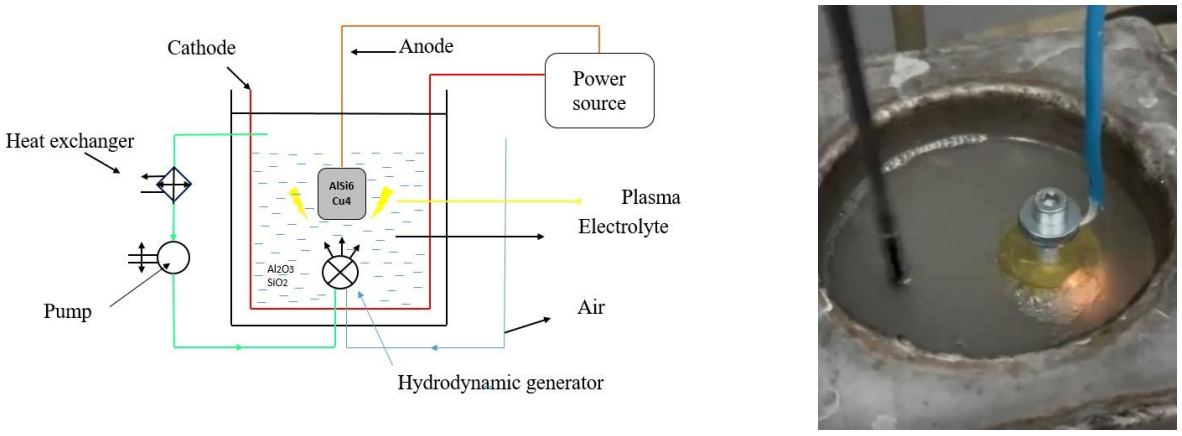

a) PEO diagram

b) PEO process

Figure 1. Schematic diagram of the experimental setup and the PEO process of the Al–Si alloy

The hydrodynamic generator provides electrolyte circulation, effective dispersion of nanoparticles, and stability of the plasma electrolytic process. The PEO parameters and operating regimes were selected based on preliminary optimization and literature-supported practices for the formation of high-quality oxide layers, as presented in Table 1. The plasma electrolytic oxidation process was carried out under galvanostatic–potentiostatic pulsed conditions. In addition to the applied voltage (400–450 V), the current density was maintained in the range of 1.2–1.5 A/dm². The pulse duty cycle was 20–30 %, with a pulse frequency of 1500–1600 Hz. The process was conducted in a bipolar pulsed mode with controlled current–voltage regulation to ensure stable micro-discharge formation.

Table 1

Main PEO treatment parameters of Al–Si alloy samples

Parameter	Value / regime	Note
Electrolyte	Aqueous NaOH solution with Al_2O_3 and SiO_2 nanoparticles	Nanoparticle concentration: 10–15 g L^{-1}
Voltage	400–450 V	Pulsed mode
Pulse frequency	1500–1600 Hz	Ensuring uniform layer formation
Current density	1.2–1.5 A/dm²	Controlled operating parameter in galvanostatic-pulsed mode
Duty cycle	20–30 %	Pulse duration / off-time ratio
Pulse mode	Bipolar pulsed	Provides stable micro-discharge regime
Treatment time	20–30 min	Actual coating: ~1.8–2.2 μm; thermal zone: ~20–30 μm
Electrolyte temperature	25–30 °C	Maintained by the cooling system
Cathode / Anode	Steel / aluminium specimen	Standard discharge configuration

It should be noted that, under the selected pulsed conditions (relatively low duty cycle and controlled energy input per pulse), the coating growth rate was intentionally limited, resulting in the formation of a relatively thin (~1.8–2.2 μm) but dense oxide layer, accompanied by a thermally affected subsurface zone extending up to ~20–30 μm (Fig. 3*d*), as confirmed by cross-sectional SEM analysis. Although the pulse frequency of 1500–1600 Hz may appear relatively low compared to some high-frequency PEO systems, it was selected based on preliminary optimization to ensure stable micro-arc discharge formation and sufficient energy input per pulse. This frequency range provides a balance between discharge intensity, coating growth rate, and thermal control of the electrolyte. In contrast to conventional PEO regimes, where higher duty cycles and continuous discharge activity lead to coating thicknesses of tens of micrometers, the present processing parameters promote shorter and more localized microdischarges, which restrict excessive coating growth while enhancing structural densification. As a result, instead of forming thick coatings typical of conventional PEO (30–50 μm), a thin (~1.8–2.2 μm) but dense oxide layer is produced, while the main energy impact is distributed within a deeper thermally affected zone (~20–30 μm). The aluminium–silicon alloy

EN AC-45000 (AlSi6Cu4), in accordance with the specifications of EN 1706 / ISO 3522, was used as the main material under investigation. The chemical composition of the alloy is presented in Table 2. This alloy was selected due to its widespread application in the automotive and mechanical engineering industries, which is attributed to the combination of high strength, adequate corrosion resistance, and good machinability. This distinction between the oxide layer thickness and the thermally modified subsurface region is clearly observed in the cross-sectional SEM image (Fig. 3*d*) and explains the apparent discrepancy with conventional PEO thickness values reported in the literature.

Such processing conditions allow the formation of coatings with improved density and reduced porosity despite their relatively small thickness, due to the predominance of localized energy dissipation and subsurface thermal modification rather than continuous coating growth.

Table 2

Chemical composition of the EN AC-45000 (AlSi6Cu4) alloy, wt.%

Element	Si	Cu	Fe	Mn	Mg	Cr	Ni	Zn	Pb	Sn	Ti	Others	Al (balance)
Min.	5.0	3.0	–	0.20	–	–	–	–	–	–	–	–	Remainder
Max.	7.0	5.0	1.0	0.65	0.55	0.15	0.45	2.00	0.30	0.15	0.25	0.05	Remainder

Samples of the EN AC-45000 alloy were mechanically cut to dimensions of 10×10×45 mm (Fig. 2*a*), mounted in Bakelite holders, ground using abrasive discs with progressively finer grit sizes, and finally polished with aluminium oxide and silicon dioxide suspensions to obtain a mirror-like surface. This preparation procedure minimizes mechanical surface damage and enables the acquisition of clear microstructural images under microscopic observation (Fig. 2*b*).

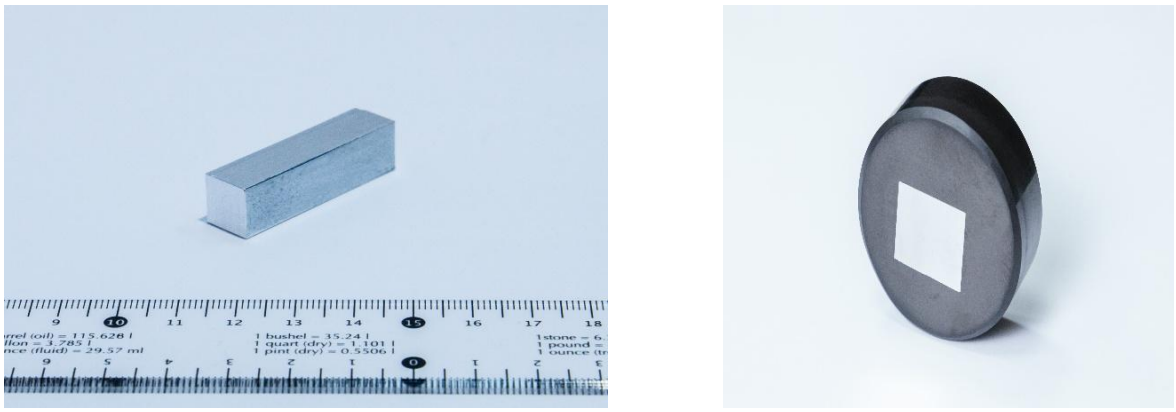

(*a*) mechanically cut specimen (*b*) surface after grinding and polishing

Figure 2. Sample preparation for PEO coatings on Al–Si alloys with Al_2O_3 and SiO_2 nanoparticles

The surface and microstructure of the coatings were studied using optical microscopy with an Olympus BX51 microscope to evaluate microstructural features, grain-phase composition, and coating thickness.

Using scanning electron microscopy (SEM) with a JEOL JSM-6390LV instrument equipped with an INCA Energy energy-dispersive microanalysis system (Oxford Instruments) to obtain surface images and elemental distribution maps, as well as to perform chemical analysis of local regions and phase areas.

The microhardness of the coatings was measured using a DuraScan 20 tester according to the Vickers method with a diamond four-sided indenter (apex angle of 136°). A load of 100 g (0.98 N) was applied with a dwell time of 30 s for each measurement. These measurements made it possible to evaluate the hardness distribution through the coating thickness and the effect of nanoparticles on the mechanical properties.

All process parameters, including voltage, current density, pulse frequency, and duty cycle, were kept constant during the experiments to ensure reproducibility of the results. The selected regime parameters are consistent with previously reported PEO studies on Al–Si alloys and were chosen to achieve stable discharge behavior and uniform coating formation. To evaluate the tribological behaviour of the coatings, sliding wear tests were carried out using the ball-on-disk method (Anton Paar TRB^3 tribometer) under dry conditions at room temperature in accordance with the ASTM G99 standard. A 100Cr6 hardened steel ball (6 mm in diameter) was used as the counterbody. The tests were performed under a normal load of 5 N, a linear sliding

speed of 0.05 m/s, and a total sliding distance of 100 m. The friction coefficient was continuously recorded during the tests. Prior to testing, the samples were ultrasonically cleaned in ethanol and dried in air. Each experiment was repeated at least three times to ensure reproducibility. The selected testing parameters provided stable contact conditions and enabled a reliable comparison of the tribological behaviour of the initial alloy and the PEO-treated samples.

Results and Discussion

Figure 3*a* shows the SEM microstructure of the AlSi6Cu4 alloy in the as-received condition. The structure is mainly composed of a primary aluminium matrix (α-Al), forming a continuous coarse-grained phase. Eutectic silicon (Si) inclusions, as well as intermetallic particles of the copper-containing θ-Al_2Cu phase, are uniformly distributed within the matrix and along grain boundaries. The presence of these phases, including the copper-bearing intermetallics, is consistent with the chemical composition of the EN AC-45000 alloy and is further confirmed by the XRD patterns, where characteristic peaks of Al, Si, and θ-Al_2Cu are clearly identified. The α-Al matrix appears as a light, continuous phase with a grain size of approximately 5–15 μm, providing the primary load-bearing capacity of the material.

The dark silicon-rich Si inclusions exhibit a finely dispersed morphology, predominantly globular-plate-like in shape, and are located both within the α-Al grains and along their boundaries, forming a characteristic eutectic network. The intermetallic θ-Al_2Cu phase is observed in the form of bright, elongated and plate-like particles, predominantly segregated along the grain boundaries of the α-phase. The presence of this phase is associated with the copper content in the alloy and plays a significant role in the formation of strength characteristics due to dispersion strengthening of the matrix. The substantial volume fraction and distinct crystallinity of these θ-Al_2Cu particles ensure their reliable detection during X-ray diffraction analysis.

Figure 3*b* presents a SEM image of the surface of the AlSi6Cu4 alloy after plasma electrolytic oxidation. As a result of the PEO process, a multiphase oxide coating is formed, the structure of which is governed by local micro-arc discharges and the electrolyte composition. Analysis of the morphology and contrast allows the identification of the main phases and structural components. The dominant phase of the dense barrier layer is α-Al_2O_3, which forms in regions of high-temperature discharges (T > 2000 °C). This phase is characterized by high density and low porosity, providing high mechanical strength and strong adhesion of the coating to the aluminium matrix. It is important to note that due to the relatively small thickness of the PEO layer (approx. 2 μm), the X-ray beam effectively penetrates through the coating into the substrate. Consequently, the XRD patterns of the treated samples represent a superposition of the oxide phases and the underlying alloy, including the characteristic peaks of the θ-Al_2Cu phase, which remains chemically stable in the bulk of the material during the process.

Compared to the surface layer, the barrier zone exhibits a more homogeneous and compact microstructure. In the outer porous layer, γ-Al_2O_3 predominates, forming under less intense discharges and rapid cooling of the molten material. This phase is characterized by a fine-grained morphology, which appears in SEM images as uniformly distributed "granular" regions. In contrast to α-Al_2O_3, γ-Al_2O_3 exhibits a higher defect density and a more developed surface, which facilitates the incorporation of electrolyte-derived species. In addition, embedded SiO_2 and Al_2O_3 nanoparticles originating from the electrolyte are present within the coating during the PEO process. These nanoparticles are predominantly localized in the pores and intergranular regions of the outer layer, forming a dispersion-strengthened structure. The presence of copper-containing intermetallics within the substrate also affects the coating composition; as the oxide layer grows, fragments of the θ-Al_2Cu phase can be partially incorporated into the porous layer or remain at the interface, contributing to the overall diffraction signal. Compared to coatings produced without nanoparticle additives, a more uniform filling of pores and a reduction in their effective diameter are observed, which potentially enhance the hardness and wear resistance of the layer. The crystalline nature of these retained and incorporated phases ensures that they are detectable by XRD, even when partially masked by the amorphous or nanocrystalline components of the oxide matrix.

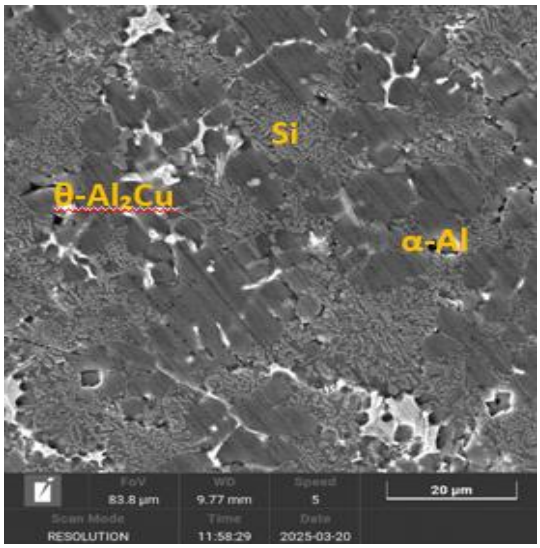

(*a*) in the as-received condition

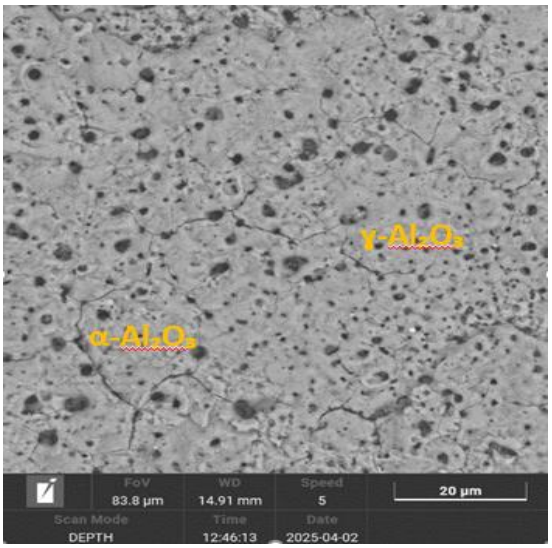

(*b*) after PEO treatment

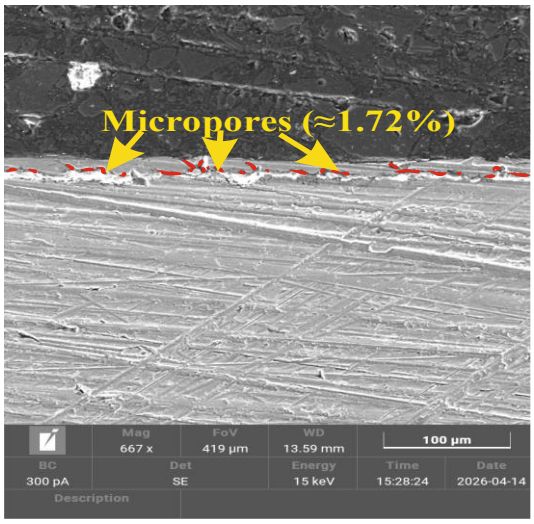

(*c*) initial cross section

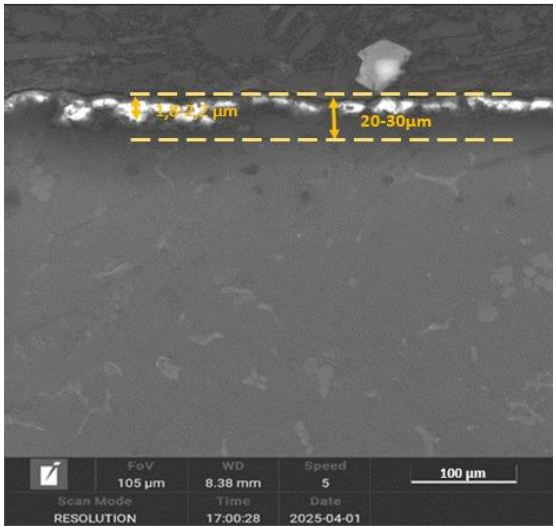

(*d*) cross section after PEO treatment

Figure 3. SEM analysis of the microstructure of the AlSi6Cu4 alloy

It should be noted that a similar multiphase structure is observed in the cross section of the sample (Fig. 3*c*), consisting of a dominant α-Al matrix with uniformly distributed eutectic Si inclusions and θ-Al_2Cu particles, which are predominantly localized along intergranular boundaries. This indicates structural homogeneity of the material not only at the surface but also throughout the sample thickness, as well as the absence of pronounced textural heterogeneity within the alloy volume. Such homogeneity is crucial for the correlation between SEM and XRD data, as the X-ray penetration depth typically exceeds the thickness of the surface layer, capturing the phase composition of the underlying substrate. To quantitatively evaluate the coating quality, porosity analysis was performed using Imaging Solution software. The cross-sectional SEM images were processed via binarization and thresholding techniques to ensure statistical accuracy. The results reveal rare, rounded micropores with diameters of approximately 1–3 µm, predominantly located along intergranular boundaries. The measured volume fraction of porosity is 1.72 % (Fig. 3*c*), which indicates a high degree of material consolidation. The α-Al grain boundaries are clearly defined and enriched with secondary phases of Si and θ-Al_2Cu, indicating segregation processes occurring during solidification and subsequent cooling. The volume fraction of the α-phase exceeds 70 %, while the fraction of eutectic silicon and intermetallic compounds is estimated at 20–25 %. Overall, the microstructure is characterized by a typical multiphase organization of cast Al–Si–Cu alloys, consisting of α-Al + Si + θ-Al_2Cu phases with localized concentrations of intermetallics along grain boundaries. This structure provides a combination of increased strength while maintaining moderate ductility of the material.

In the cross section after PEO treatment (Fig. 3*d*), a significant change in the morphology and size of structural elements is observed compared to the initial state of the alloy, which is attributed to the action of high-temperature plasma micro-arc discharges. A distinct oxide coating is formed on the substrate surface with a thickness of approximately 1.8–2.2 μm. High-magnification SEM imaging and EDS line-scan analysis clearly identify the boundary of this layer, which is enriched with SiO_2 and Al_2O_3 nanoparticles from the electrolyte. It should be emphasized that, in addition to this relatively thin oxide coating, a significantly thicker thermally affected zone (~20–30 μm) is formed in the near-surface region of the substrate, as shown in Figure 3*d*. This zone is associated with intensive thermal and plasma-chemical effects during micro-arc discharges and reflects structural modification of the aluminium matrix without complete oxidation. Given that the information-depth of Cu-Kα radiation in aluminium alloys typically ranges from 50 to 80 μm, the XRD analysis inevitably captures the structural data from both the thin PEO coating and the extensive thermally affected zone of the substrate. This explains why the XRD patterns contain strong signals from the substrate phases (Al, Si, and θ-Al_2Cu) despite the presence of the surface oxide. In the near-surface region of the substrate, partial redistribution of Si and Cu and local modification of α-Al grains are observed, indicating the thermal and plasma-chemical effects of the PEO process. The inner zone of the coating contains dispersed inclusions of Si- and Cu-containing phases inherited from the AlSi6Cu4 substrate and partially oxidised during treatment. In SEM images, these inclusions appear as dark particles with sizes of approximately 0.5–1.5 μm, uniformly distributed throughout the barrier layer. Compared to the surface of the initial alloy, a finer and more stable dispersion of these phases is observed after PEO due to element redistribution during micro-arc discharges. The presence of the θ-Al_2Cu phase, which the reviewer correctly noted as a significant component of the substrate (3–5 % Cu), is explicitly identified in the XRD patterns alongside the Al and Si peaks. This confirms that the PEO treatment, while modifying the surface, does not eliminate the primary alloying intermetallics in the volume of the material sampled by X-ray. Analysis of grain size and porosity indicates that γ-Al_2O_3 grains and embedded nanoparticles are distributed fairly uniformly over the surface. Fine pores with sizes of approximately 200–500 nm are formed, creating a branched network for nanoparticle fixation. At the same time, craters with diameters of 1–2 μm are formed in regions of intense discharges, where local accumulation of Si and Cu is observed. Compared with less energy-intensive PEO regimes, these areas are characterised by increased surface roughness; however, they contribute to additional alloying of the coating with elements from the substrate. Additional EDS analysis of the cross section confirms the presence of an oxygen-rich oxide layer and a gradual compositional transition within the thermally affected zone, which supports the distinction between the coating and the modified substrate region. Thus, PEO treatment of the AlSi6Cu4 alloy results in the formation of a hierarchical multiphase structure, including a dense α-Al_2O_3 barrier layer and a porous γ-Al_2O_3 surface layer modified with SiO_2 and Al_2O_3 nanoparticles, as well as dispersed Cu- and Si-containing phases. Despite the relatively high applied voltage, the limited thickness of the oxide layer is attributed to the selected pulsed processing conditions (low duty cycle and controlled energy input), which restrict coating growth while promoting structural densification. The XRD results are therefore a comprehensive representation of this hierarchical system, clearly resolving the oxide phases of the coating and the metallic/intermetallic phases (α-Al, Si, and θ-Al_2Cu) of the modified substrate. Compared to the initial state of the alloy, the resulting coating exhibits a more developed microstructure, increased phase distribution uniformity, and potentially improved mechanical and tribological properties.

To confirm the results obtained from SEM analysis and to more accurately identify the phase transformations occurring in the surface layer of the alloy as a result of plasma electrolytic oxidation, X-ray diffraction analysis was performed. Figure 4 presents the results of the phase composition analysis of the sample after PEO obtained by X-ray diffraction using a X'Pert PRO diffractometer with Cu Kα radiation ($\lambda K\alpha 1 = 1.54060$ Å, $\lambda K\alpha 2 = 1.54443$ Å). The diffraction pattern was recorded in the 2θ range of 20.01–89.99° with a step size of 0.02° and a counting time of 2 s per point, in continuous scanning mode at room temperature (25 °C). It should be noted that the diffraction pattern of the initial alloy is characterized predominantly by reflections of the aluminium matrix, whereas after PEO treatment the formation of additional phases associated with the development of the oxide coating is observed. Figure 4 shows the experimental diffraction profile with the positions of the detected peaks indicated and superimposed reference reflections of the phases identified through database search and comparison.

The main intense peaks at $2\theta \approx 38.66°$, 44.88°, 65.31°, and 78.40° correspond to the crystalline aluminium (Al) phase, indicating the preservation of the metallic substrate beneath the oxide layer. At the same time, weak and medium-intensity reflections are observed, evidencing the presence of aluminium oxide

phases, including α-Al_2O_3 and a complex oxide phase, as well as trace amounts of silicon (Si) characteristic of the AlSi6Cu4 alloy.

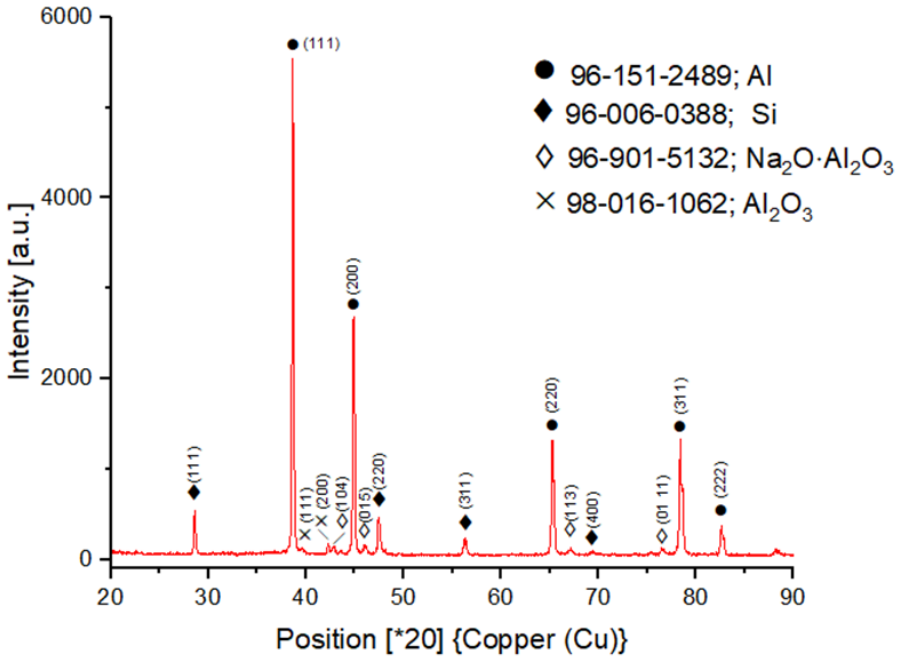

Figure 4. X-ray diffraction analysis of the AlSi6Cu4 alloy sample after plasma electrolytic oxidation (PEO)

The appearance of oxide phases is in good agreement with the SEM analysis results, which confirm the formation of a PEO coating with a developed micro- and nanoscale structure. The presence of nanoparticles and defect-rich crystalline regions within the oxide layer accounts for the relatively low intensity and partial mismatch of certain diffraction reflections. At the same time, the formation of corundum-type phases (α-Al_2O_3) is of fundamental importance, since corundum is characterized by high hardness, wear resistance, and thermal stability, which directly determines the enhanced mechanical and protective properties of the PEO coating.

Table 3 presents the results of the phase analysis of X-ray diffraction data for the AlSi6Cu4 alloy treated by plasma electrolytic oxidation (PEO). Phase identification was performed using the search-and-match method by comparing the experimental diffraction pattern with reference database cards.

Table 3

Phase analysis of the AlSi6Cu4 alloy after PEO treatment

PDF-card	Count	Compound name	Scale factor	Phase	Chemical formula
96–151–2489	70	1512488	0.641	α-Al	Al
96–901–5132	27	9015131	0.006	Na-aluminate (β-type)	$Na_2O·Al_2O_3$
98–006–0388	40	Silicon	0.029	α-Si	Si
98–016–1062	–	Aluminium oxide	0.089	α-Al_2O_3	Al_2O_3

The main identified phase is α-Al (PDF card No. 96–151–2489), which is characterized by the highest match count and the maximum scale factor. This indicates the dominant presence of the aluminium matrix of the alloy, which is retained after PEO treatment. The phase previously denoted as β-Al_2O_3 is more accurately described as a sodium-containing aluminate ($Na_2O·Al_2O_3$), formed due to the use of a NaOH-based electrolyte during the PEO process. Therefore, it does not represent a pure aluminium oxide phase but rather a Na-aluminate compound.

The presence of α-Si (PDF card No. 98–006–0388) confirms the chemical composition of the initial AlSi6Cu4 alloy and is associated with silicon phase precipitates characteristic of aluminium-silicon casting alloys. The small scale factor indicates its secondary role in the formation of the diffraction pattern. The absence of distinct γ-Al_2O_3 reflections in the XRD patterns can be attributed to its nanocrystalline or poorly ordered structure, peak broadening, and possible overlap with other diffraction signals. In addition, γ-Al_2O_3

is typically present in small amounts within the outer porous layer of PEO coatings and may not be clearly detected by XRD.

The α-Al_2O_3 phase (PDF card No. 98–016–1062) is marked as having a strong mismatch, which may be attributed to low crystallinity, a high defect density, or an amorphous-crystalline state of the PEO layer. Nevertheless, its presence further confirms the formation of a protective oxide coating on the alloy surface during the PEO process.

Thus, X-ray diffraction analysis in combination with SEM data demonstrates that plasma electrolytic oxidation results in the formation of a multiphase oxide coating on the surface of the AlSi6Cu4 alloy. The structure of the sample after PEO treatment consists of an aluminium matrix with silicon inclusions and a developed oxide layer based on aluminium compounds, including nanostructured oxide phases. The formation of such phases, which are characteristic of PEO coatings, leads to enhanced mechanical and service properties of the material, in accordance with the expected structural and phase transformations of aluminium alloys after PEO treatment.

During PEO, the formation of the oxide layer occurs mainly due to melting and intense oxidation of the liquid metal. Micro-arc discharges that melt the metal arise in microscopic channels penetrating the oxide layer. Prior to this, vapour-gas bubbles are formed within the microchannels. These transient plasma–gas cavities act as localized reactors, facilitating the interaction between nanoparticles and the molten oxide matrix. We assume that solid Al_2O_3 and SiO_2 nanoparticles, carrying a negative electric charge, enter these bubbles and are accelerated by the electric field to velocities sufficient for easy penetration into the walls and bottom of the microchannels. In the case of Al_2O_3 nanoparticles, their high melting point and chemical compatibility with the alumina matrix promote their incorporation as a reinforcing phase without significant phase transformation. In contrast, SiO_2 nanoparticles may undergo partial amorphization or interact with aluminium oxide, contributing to the formation of defect-rich or aluminosilicate-like regions, which can enhance pore sealing and structural uniformity of the coating. Due to friction and heating upon impact, the nanoparticles lose electrons and acquire a positive charge. All these processes lead to sparking on the nanoparticles embedded in the layer, resulting in a reduction of the micro-arc initiation voltage. Therefore, microscopic electric arcs persist for a longer duration, and the number of such microdischarges increases. This explains why, for the same processing time, a larger volume of metal is oxidized when nanoparticles are added to the electrolyte, and the overall process becomes more uniform. Accordingly, a greater amount of equilibrium and hard constituents is formed within the layer, making it more homogeneous, dense, and harder, while its protective properties against wear and corrosion are enhanced. As a result, an oxide layer with a new set of properties is obtained, which meets more stringent mechanical and corrosion resistance requirements compared to a conventional oxide layer and is therefore capable of operating under more severe conditions.

In the initial state, the microhardness of the alloy is 65–80 HV, which is typical for the AlSi6Cu4 alloy with a predominance of a soft α-Al matrix and dispersed Si and θ-Al_2Cu inclusions (Fig. 5). Such a microstructure, as established by SEM analysis, provides moderate strength and ductility; however, the absence of hard surface phases results in relatively low microhardness values.

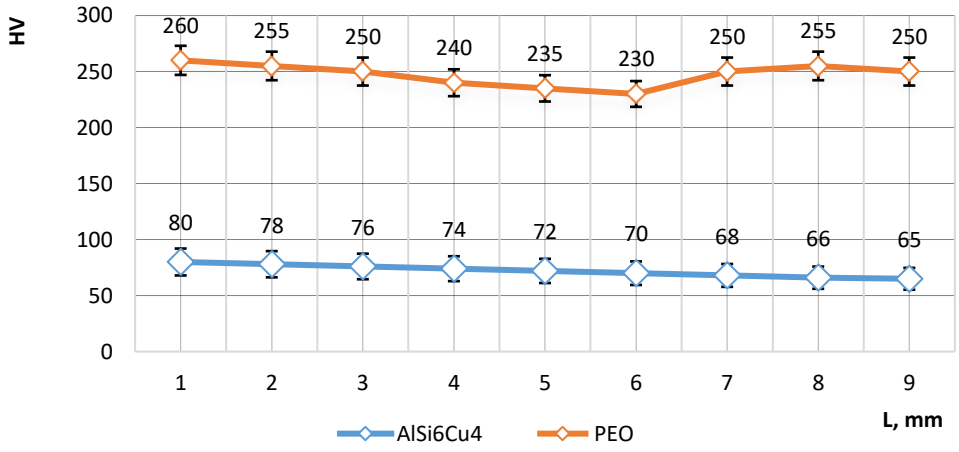

Figure 5. Microhardness values of the AlSi6Cu4 alloy

After plasma electrolytic oxidation, the average microhardness increases to approximately 245–250 HV, i.e., more than threefold. This strengthening is associated with the formation of a multiphase oxide coating consisting of a dense α-Al_2O_3 barrier layer and an outer porous layer based on γ-Al_2O_3, as confirmed by SEM observations and X-ray diffraction analysis. The presence of a corundum-like α-Al_2O_3 phase, which exhibits high hardness, is a key factor contributing to the increased resistance to localized plastic deformation.

It should be noted that the obtained microhardness values are lower than those typically reported for thick PEO coatings containing α-Al_2O_3 (800–1400 HV). This difference is primarily attributed to the relatively small thickness of the oxide layer (~1.8–2.2 μm), which leads to a significant influence of the softer aluminium substrate on the measured values. In addition, the α-Al_2O_3 phase is likely localized within individual microdischarge regions rather than forming a continuous layer, while the coating is predominantly composed of γ-Al_2O_3 with a higher defect density. Furthermore, the presence of a developed porous structure, as observed in SEM images, also contributes to the reduction of the effective microhardness. An additional contribution to the increase in microhardness is provided by the incorporation of SiO_2 and Al_2O_3 nanoparticles, as well as dispersed Si- and Cu-containing phases detected within the PEO layer. The mechanism of their incorporation into the coating through microchannels formed by micro-arc discharges leads to structural densification, a reduction in porosity, and the formation of a more uniform and harder oxide layer. The increased duration and density of microdischarges in the presence of nanoparticles promote the formation of a greater amount of thermodynamically stable and rigid oxide phases. Thus, the observed increase in microhardness after PEO is a direct consequence of the structural and phase transformations revealed by SEM and XRD analyses and confirms the formation of a dense, homogeneous, and mechanically strong oxide layer with enhanced wear and corrosion protection properties, although the measured values represent the combined response of the thin oxide layer and the underlying substrate rather than the intrinsic hardness of bulk α-Al_2O_3.

To further evaluate the functional performance of the obtained coatings, tribological tests were carried out using the ball-on-disk method in accordance with the ASTM G99 standard. The tests were performed using an Anton Paar TRB³ pin-on-disk tribometer (operating in ball-on-disk mode) with a 100Cr6 steel ball (6 mm in diameter) as the counterbody. The experiments were conducted under a normal load of 5 N, a linear sliding speed of 5 cm/s (0.05 m/s), and a total sliding distance of 100 m under dry sliding conditions at room temperature. The evolution of the friction coefficient as a function of sliding distance for the initial AlSi6Cu4 alloy and the PEO-treated sample is presented in Figure 6.

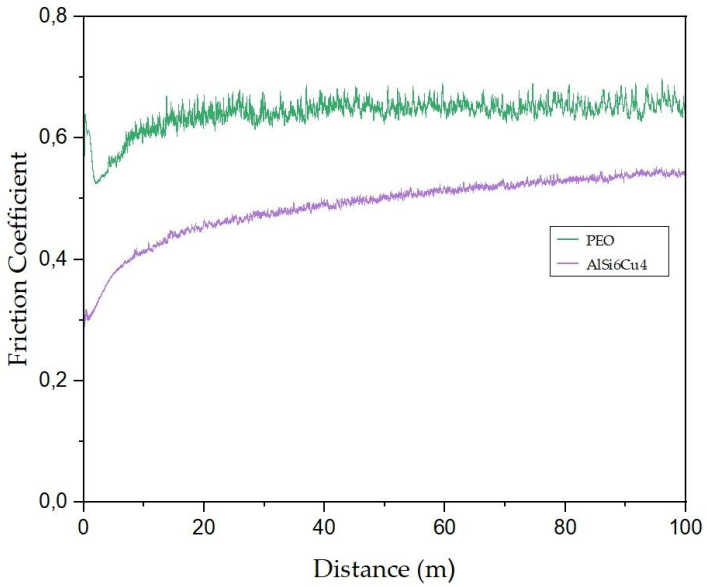

Figure 6. Evolution of the friction coefficient as a function of sliding distance for the initial AlSi6Cu4 alloy and after plasma electrolytic oxidation (PEO) treatment

As shown in Figure 6, the initial alloy exhibits a relatively low and gradually increasing friction coefficient, ranging from approximately 0.22 to 0.52, which is typical for aluminium alloys with a soft α-Al matrix

and is commonly associated with adhesive wear mechanisms. In contrast, the PEO-treated sample demonstrates a higher friction coefficient (approximately 0.40–0.72), characterized by an initial running-in stage followed by a quasi-stable regime. Such behaviour is consistent with PEO coatings reported in the literature and is attributed to increased surface roughness, the presence of a developed porous morphology, and the formation of hard oxide phases, primarily α-Al_2O_3 and γ-Al_2O_3.

It should be noted that a higher friction coefficient does not necessarily indicate inferior tribological performance. On the contrary, oxide ceramic coatings formed by plasma electrolytic oxidation typically exhibit increased friction due to their rough and hard surface, while simultaneously providing improved resistance to material removal. In the present case, the stabilization of the friction coefficient after the running-in stage suggests the formation of a mechanically stable contact interface.

The incorporation of Al_2O_3 and SiO_2 nanoparticles into the coating structure contributes to microstructural densification and a reduction in effective porosity, which may enhance the load-bearing capacity of the surface layer and improve its resistance to deformation during sliding. However, it should be emphasized that a quantitative assessment of wear resistance requires additional analysis of wear tracks and wear rates.

Thus, the obtained tribological results (Fig. 6) are in good agreement with the microstructural and phase analysis and indicate that the nanomodified PEO coating forms a stable frictional response under sliding conditions, which is a prerequisite for improved wear performance.

Conclusion

As a result of the conducted study, the high efficiency of plasma electrolytic oxidation of the aluminium–silicon alloy EN AC-45000 (AlSi6Cu4) with the addition of Al_2O_3 and SiO_2 nanoparticles to the electrolyte has been confirmed. It has been established that PEO treatment leads to the formation of a relatively thin (~1.8–2.2 μm) hierarchically organized two-layer oxide coating, accompanied by a thermally affected subsurface zone (~20–30 μm), consisting of a dense barrier layer based on α-Al_2O_3 and an outer porous layer predominantly composed of γ-Al_2O_3, modified with nanoparticles and dispersed Si- and Cu-containing phases.

It has been shown that the introduction of nanoparticles into the electrolyte significantly affects the kinetics and stability of micro-arc discharges, promoting an increase in their density and duration, which ensures more uniform surface oxidation and densification of the coating structure. This results in reduced effective porosity, improved microstructural homogeneity, and a higher fraction of stable oxide phases.

It was experimentally established that the surface microhardness of the alloy after PEO increases by more than three times—from 65–80 HV in the initial state to approximately 245–250 HV—indicating a significant strengthening effect of the coating-substrate system. Despite the presence of a corundum-like α-Al_2O_3 phase, its contribution to the overall hardness is limited due to the small coating thickness, partial phase distribution, and residual porosity of the outer layer. The obtained data confirm the proposed concept of the possibility of targeted control of the structural and phase state of PEO coatings through nanomodification of the electrolyte.

The tribological tests performed using the ball-on-disk method demonstrated that the nanomodified PEO coatings exhibit a stable frictional response characterized by an initial running-in stage followed by a quasi-steady regime. Although the friction coefficient of the coated samples (approximately 0.40–0.72) is higher compared to the initial alloy (approximately 0.22–0.52), this behaviour is typical for ceramic oxide layers and is associated with increased surface roughness and the presence of hard α-Al_2O_3 and γ-Al_2O_3 phases. At the same time, a ~25–35 % reduction in wear track width was observed for the PEO-treated samples, indicating improved resistance to material removal. These results confirm that the formation of a dense oxide layer and its modification with Al_2O_3 and SiO_2 nanoparticles contribute to enhanced tribological performance of the Al–Si alloy. The practical significance of this work lies in the possibility of applying nanomodified PEO coatings to enhance the wear and corrosion resistance of aluminium–silicon alloys used under conditions of increased mechanical and thermal loads. Further work may focus on optimization of nanoparticle parameters and long-term performance evaluation under real operating conditions.

Acknowledgment

This research was funded by the Ministry of Science and Higher Education of the Republic of Kazakhstan, within the framework of the grant project AP23490089 “Development and research of scientific and technological fundamentals of plasma electrolytic oxidation of the surface of Al–Si alloys with the participation of Al_2O_3 and SiO_2 nanoparticles” and BR24992854 “Development and implementation of competitive

science-based technologies to ensure sustainable development of mining and metallurgy industry East Kazakhstan region".

References

1 Yeshmanova G.B. Plasma electrolytic oxidation technology for producing protective coatings of aluminum alloys / G.B. Yeshmanova, D.U. Smagulov, C. Blawert // Complex use of mineral resources. — 2021. — 317(2). — 78–93. https://doi.org/10.31643/2021/6445.21.

2 Sowa M. (2021). Corrosion inhibitor-modified plasma electrolytic oxidation coatings on 6061 aluminum alloy / M. Sowa, M. Wala, A. Błacha-Grzechnik, A. Maciej, A. Kazek-Kęsik, A. Stolarczyk, W. Simka // Materials. — 2021. — 14(3). — Article 619. https://doi.org/10.3390/ma14030619.

3 Dzhurinskiy D.V. Surface modification of aluminum 6061-O alloy by plasma electrolytic oxidation to improve corrosion resistance properties / D.V. Dzhurinskiy, S.S. Dautov, P.G. Shornikov, I.S. Akhatov // Coatings. — 2021. — 11(1). — Article 4. https://doi.org/10.3390/coatings11010004.

4 Peng Z. Wear and corrosion resistance of plasma electrolytic oxidation coatings on 6061 Al alloy in electrolytes with aluminate and phosphate / Z. Peng, H. Xu, S. Liu, Y. Qi, J. Liang // Materials. — 2021. — 14(14). — Article 4037. https://doi.org/10.3390/ma14144037.

5 Famiyeh L. Plasma electrolytic oxidation coatings on aluminum alloys: Microstructures, properties, and applications / L. Famiyeh, X. Huang // Modern Concepts in Material Science. — 2019. — 2(1). — Article 000526. https://doi.org/10.33552/MCMS.2020.02.000526.

6 Егоркин В.С. Формирование твердых, износостойких ПЭО-покрытий на сплаве алюминия АМг3 [Электронный ресурс] / В.С. Егоркин, И.Е. Вялый, С.Л. Синебрюхов, С.В. Гнеденков // Вестник ДВО РАН. — 2015. — № 4. — С. 53–61. Режим доступа: https://cyberleninka.ru/article/n/formirovanie-tverdyh-iznosostoykih-peo-pokrytiy-na-splave-alyuminiya-amg3.

7 Nadimi M. Influence of SiO_2 nanoparticles incorporating into ceramic coatings generated by PEO on aluminium alloy: Morphology, adhesion, corrosion, and wear resistance / M. Nadimi, C. Dehghanian, A. Etemadmoghadam // Materials Today Communications. — 2022. — 31. — 103587. https://doi.org/10.1016/j.mtcomm.2022.103587.

8 Uazyrkhanova G. High-frequency plasma electrolytic oxidation of an Al–Si alloy: Influence of Al_2O_3 and SiO_2 additives on coating microstructure and tribological performance / G. Uazyrkhanova, A. Sagidugumar, Y. Kozhakhmetov, G. Moldabayeva, D. Kaliyev, S. Rudenko, N. Kantay // Materials. — 2025. — 18(23). — Article 5334. https://doi.org/10.3390/ma18235334.

9 Lu X. Plasma electrolytic oxidation coatings with particle additions — A review / X. Lu, M. Mohedano, C. Blawert, E. Matykina, R. Arrabal, K.U. Kainer, M.L. Zheludkevich // Surface and Coatings Technology. — 2016. — 307 (Part C). — 1165–1182. https://doi.org/10.1016/j.surfcoat.2016.08.055.

10 Козлов И.А. Плазменное электролитическое оксидирование магниевых сплавов (обзор) / И.А. Козлов, С.С. Виноградов, К.Г. Тарасова, Н.В. Кулюшина, В.А. Манченко // Авиационные материалы и технологии. — 2019. — № 1(54). — С. 23–36. https://doi.org/10.18577/2071-9140-2019-0-1-23-36.

11 Yerokhin A.L. Plasma electrolysis for surface engineering / A.L. Yerokhin, X. Nie, A. Leyland, A. Matthews, S.J. Dowey. // Surface and Coatings Technology. — 1999. — 122. — 73–93. https://doi.org/10.1016/S0257-8972(99)00441-7.

12 Popova N.A. Influence of surface quenching on morphology and phase composition of ferritic–pearlitic steel / N.A. Popova, E.L. Nikonenko, E.E. Tabieva, G.K. Uazyrkhanova, V.E. Gromov // Izvestiia. Ferrous Metallurgy. — 2020. — 63(11-12). — 915–921. https://doi.org/10.17073/0368-0797-2020-11-12-915-921.

13 Kombayev K. Experimental and mathematical modelling investigation of plasma electrolytic oxidation (PEO) for surface hardening of 20Ch steel / K. Kombayev, F. Khoshnaw, G. Uazyrkhanova, G. Moldabayeva // Materials. — 2024. — 17(24). — Article 6043. https://doi.org/10.3390/ma17246043.

14 Kombayev K. Improving wear resistance by electrolyte-plasma hardening of corrosion-resistant steel of the tip / K. Kombayev, A. Kim, G. Sypainova, D. Yelemanov // Journal of Applied Engineering Science. — 2023. — 21(3). — 810–819. https://doi.org/10.5937/jaes0-42291.

15 Fernández-López P. Plasma electrolytic oxidation (PEO) as a promising technology for the development of high-performance coatings on cast Al–Si alloys: A review / P. Fernández-López, S.A. Alves, J.T. San-Jose, E. Gutierrez-Berasategui, R. Bayón // Coatings. — 2024. — 14(2). — Article 217. https://doi.org/10.3390/coatings14020217.

К.К. Комбаев, Г.С. Молдабаева, Е.А. Кожахметов,
Г.К. Уазырханова, Е.Е. Табиева, Д.Н. Кәкімжанов

Al_2O_3 және SiO_2 нанобөлшектері бар Al–Si қорытпаларының ПЭО-жабындарының құрылымдық-фазалық күйі және механикалық қасиеттері

Жұмыста Al_2O_3 және SiO_2 нанобөлшектері қосылған электролитте EN AC-45000 (AlSi6Cu4) алюминий-кремний қорытпасының бетінде алынған плазмалық-электролиттік оксидтік (ПЭО)

жабындардың құрылымдық-фазалық және механикалық қасиеттерін кешенді зерттеу нәтижелері ұсынылған. Зерттеудің мақсаты — электролит наномодификациясының ПЭО-жабындарының морфологиясына, фазалық құрамына және микроқаттылығына әсерін анықтау. ПЭО үрдісі NaOH негізіндегі сулы электролитте жүргізілді, оған алюминий мен кремний оксидтерінің нанобөлшектері енгізілді. Жабындардың микроқұрылымы мен морфологиясы оптикалық және сканерлеуші электрондық микроскопия әдістерімен зерттелді, элементтік және фазалық құрамы энергодисперсиялық талдау және рентгендік дифракция әдісімен анықталды. Механикалық қасиеттері Виккерс әдісі бойынша микроқаттылықты өлшеу арқылы бағаланды. Зерттеу нәтижесінде қорытпа бетінде тығыз ішкі тосқауыл қабатынан (α-Al_2O_3) және γ-Al_2O_3 негізіндегі кеуекті сыртқы қабаттан тұратын екі қабатты оксидтік жабын қалыптасатыны анықталды. Нанобөлшектердің енгізілуі жабын құрылымының тығыздалуына, кеуектіліктің төмендеуіне және микродоғалық разрядтардың біркелкі жүруіне ықпал етеді. ПЭО-өңдеуден кейін беткі микроқаттылықтың 65–80 HV-дан ~245–250 HV-ға дейін, яғни үш еседен астам артқаны көрсетілді. Алынған нәтижелер алюминий-кремний қорытпаларының пайдалану қасиеттерін арттыру үшін наномодификацияланған ПЭО-әдісінің жоғары тиімділігін дәлелдейді.

Кілт сөздер: плазмалық-электролиттік оксидтеу, алюминий-кремний қорытпасы, ПЭО-жабыны, Al_2O_3 нанобөлшектері, SiO_2 нанобөлшектері, микроқұрылым, микроқаттылық

К.К. Комбаев, Г.С. Молдабаева, Е.А. Кожахметов,
Г.К. Уазырханова, Е.Е. Табиева, Д.Н. Какимжанов

Структурно-фазовые состояние и механические свойства ПЭО-покрытий Al–Si сплавов с наночастицами Al_2O_3 и SiO_2

В данной работе представлены результаты комплексного исследования структурно-фазовых и механических свойств плазменно-электролитных оксидных (ПЭО) покрытий, полученных на поверхности алюминиево-кремниевого сплава EN AC-45000 (AlSi6Cu4) в электролите, модифицированном наночастицами Al_2O_3 и SiO_2. Целью исследования являлось определение влияния наномодификации электролита на морфологию, фазовый состав и микротвёрдость ПЭО-покрытий. Процесс ПЭО проводился в водном электролите на основе NaOH, в который были введены наночастицы оксидов алюминия и кремния. Микроструктура и морфология покрытий исследовались методами оптической и сканирующей электронной микроскопии, элементный и фазовый состав определялись с помощью энергодисперсионного анализа и рентгеновской дифракции. Механические свойства оценивались путём измерения микротвёрдости по методу Виккерса. В результате исследования установлено, что на поверхности сплава формируется двухслойное оксидное покрытие, состоящее из плотного внутреннего барьерного слоя (α-Al_2O_3) и пористого внешнего слоя на основе γ-Al_2O_3. Введение наночастиц способствует уплотнению структуры покрытия, снижению пористости и более равномерному протеканию микродуговых разрядов. Показано, что после ПЭО-обработки поверхностная микротвёрдость увеличивается с 65–80 HV до ~245–250 HV, то есть более чем в три раза. Полученные результаты подтверждают высокую эффективность наномодифицированного ПЭО-метода для повышения эксплуатационных свойств алюминиево-кремниевых сплавов.

Ключевые слова: плазменно-электролитическое оксидирование, алюминиево-кремниевый сплав, ПЭО-покрытие, наночастицы Al_2O_3, наночастицы SiO_2, микроструктура, микротвердость

References

1 Yeshmanova, G.B., Smagulov, D.U., & Blawert, C. (2021). Plasma electrolytic oxidation technology for producing protective coatings of aluminum alloys. *Complex use of mineral resources, 317*(2), 78–93. https://doi.org/10.31643/2021/6445.21.

2 Sowa, M., Wala, M., Błacha-Grzechnik, A., Maciej, A., Kazek-Kęsik, A., Stolarczyk, A., & Simka, W. (2021). Corrosion inhibitor-modified plasma electrolytic oxidation coatings on 6061 aluminum alloy. *Materials, 14*(3), Article 619. https://doi.org/10.3390/ma14030619.

3 Dzhurinskiy, D.V., Dautov, S.S., Shornikov, P.G., & Akhatov, I.S. (2021). Surface modification of aluminum 6061-O alloy by plasma electrolytic oxidation to improve corrosion resistance properties. *Coatings, 11*(1), Article 4. https://doi.org/10.3390/coatings11010004.

4 Peng, Z., Xu, H., Liu, S., Qi, Y., & Liang, J. (2021). Wear and corrosion resistance of plasma electrolytic oxidation coatings on 6061 Al alloy in electrolytes with aluminate and phosphate. *Materials, 14*(14), Article 4037. https://doi.org/10.3390/ma14144037.

5 Famiyeh, L., & Huang, X. (2019). Plasma electrolytic oxidation coatings on aluminum alloys: Microstructures, properties, and applications. *Modern Concepts in Material Science, 2*(1), Article 000526. https://doi.org/10.33552/MCMS.2020.02.000526.

6 Egorkin, V.S., Vyaliy, I.E., Sinebryukhov, S.L., & Gnedenkov, S.V. (2015). Formirovanie tverdykh, iznosostoikikh PEO-pokrytii na splave aliuminiia AMg3 [Formation of the hard, wear-resistant PEO-coatings on aluminum alloy AMg3]. *Vestnik Dalnevostochnogo otdeleniia Rossiiskoi akademii nauk — Vestnik of the Far East Branch of the Russian Acsdemy of Sciences*, 4, 53–61. Retrieved from https://cyberleninka.ru/article/n/formirovanie-tverdyh-iznosostoykih-peo-pokrytiy-na-splave-alyuminiya-amg3.

7 Nadimi, M., Dehghanian, C., & Etemadmoghadam, A. (2022). Influence of SiO_2 nanoparticles incorporating into ceramic coatings generated by PEO on aluminium alloy: Morphology, adhesion, corrosion, and wear resistance. *Materials Today Communications*, *31*, 103587. https://doi.org/10.1016/j.mtcomm.2022.103587

8 Uazyrkhanova, G., Sagidugumar, A., Kozhakhmetov, Y., Moldabayeva, G., Kaliyev, D., Rudenko, S., & Kantay, N. (2025). High-frequency plasma electrolytic oxidation of an Al–Si alloy: Influence of Al_2O_3 and SiO_2 additives on coating microstructure and tribological performance. *Materials, 18*(23), Article 5334. https://doi.org/10.3390/ma18235334.

9 Lu, X., Mohedano, M., Blawert, C., Matykina, E., Arrabal, R., Kainer, K.U., & Zheludkevich, M.L. (2016). Plasma electrolytic oxidation coatings with particle additions — A review. *Surface and Coatings Technology, 307* (Part C), 1165–1182. https://doi.org/10.1016/j.surfcoat.2016.08.055.

10 Kozlov, I.A., Vinogradov, S.S., Tarasova, K.G., Kulyushina, N.V., & Manchenko, V.A. (2019). Plazmennoe elektrolitcheskoe oksidirovanie magnievykh splavov (obzor) [Plasma electrolytic oxidation of magnesium alloys (review)]. *Aviatsionnye materialy i tekhnologii — Aviation Materials and Technologies*, 1(54), 23–36. https://doi.org/10.18577/2071-9140-2019-0-1-23-36.

11 Yerokhin, A.L., Nie, X., Leyland, A., Matthews, A., & Dowey, S.J. (1999). Plasma electrolysis for surface engineering. *Surface and Coatings Technology, 122*, 73–93. https://doi.org/10.1016/S0257-8972(99)00441-7.

12 Popova, N.A., Nikonenko, E.L., Tabieva, E.E., Uazyrkhanova, G.K., & Gromov, V.E. (2020). Influence of surface quenching on morphology and phase composition of ferritic–pearlitic steel. *Izvestiia. Ferrous Metallurgy, 63*(11-12), 915–921. https://doi.org/10.17073/0368-0797-2020-11-12-915-921.

13 Kombayev, K., Khoshnaw, F., Uazyrkhanova, G., & Moldabayeva, G. (2024). Experimental and mathematical modelling investigation of plasma electrolytic oxidation (PEO) for surface hardening of 20Ch steel. *Materials, 17*(24), Article 6043. https://doi.org/10.3390/ma17246043.

14 Kombayev, K., Kim, A., Sypainova, G., & Yelemanov, D. (2023). Improving wear resistance by electrolyte-plasma hardening of corrosion-resistant steel of the tip. *Journal of Applied Engineering Science, 21*(3), 810–819. https://doi.org/10.5937/jaes0-42291.

15 Fernández-López, P., Alves, S.A., San-Jose, J.T., Gutierrez-Berasategui, E., & Bayón, R. (2024). Plasma electrolytic oxidation (PEO) as a promising technology for the development of high-performance coatings on cast Al–Si alloys: A review. *Coatings, 14*(2), Article 217. https://doi.org/10.3390/coatings14020217.

Information about the authors

Kombayev, Kuat — Candidate of Technical Sciences, Associate professor, D. Serikbayev East Kazakhstan Technical University, Serikbayev Street, 19, Ust-Kamenogorsk, Kazakhstan; e-mail: kkombaev@edu.ektu.kz; ORCID ID https://orcid.org/0000-0002-6929-2748

Moldabayeva, Gulzhaz (*corresponding author*) — Doctoral student, D. Serikbayev East Kazakhstan Technical University, Serikbayev Street, 19, Ust-Kamenogorsk, Kazakhstan; e-mail: gmoldabaeva@edu.ektu.kz; ORCID ID https://orcid.org/0000-0001-9192-7087

Kozhakhmetov, Yernat — PhD, Head of the Center of Excellence "VERITAS", D. Serikbayev East Kazakhstan Technical University, Serikbayev Street, 19, Ust-Kamenogorsk, Kazakhstan; e-mail: ykozhakhmetov@edu.ektu.kz; ORCID ID https://orcid.org/0000-0002-6778-1898

Uazyrkhanova, Gulzhaz — PhD, Director of the Department of Research Activities, D. Serikbayev East Kazakhstan Technical University, Serikbayev Street, 19, Ust-Kamenogorsk, Kazakhstan; e-mail: guazyrhanova@edu.ektu.kz; ORCID ID https://orcid.org/0000-0002-9817-9752

Tabiyeva, Yerkezhan — PhD, Leading Researcher, Senior Lecturer, D. Serikbayev East Kazakhstan Technical University, Serikbayev Street, 19, Ust-Kamenogorsk, Kazakhstan; e-mail: etabieva@edu.ektu.kz; ORCID ID https://orcid.org/0000-0002-9726-7187

Kakimzhanov, Dauir — Doctoral student, D. Serikbayev East Kazakhstan Technical University, Serikbayev Street, 19, Ust-Kamenogorsk, Kazakhstan; e-mail: d.kakimzhanov19@gmail.com; ORCID ID https://orcid.org/0000-0001-9453-0456

Article

UDC 537.533.34

https://doi.org/10.31489/2026PH2/27-37

Received: 05.03.2026
Accepted: 22.04.2026

M.K. Tungushbekova[1], Zh.T. Kambarova[1]✉, A.O. Saulebekov[2], A.A. Trubitsyn[3], T.Zh. Shugayeva[4]

Design and Performance Analysis of an Electrostatic Energy Analyzer Based on Multipole-Spherical Fields

[1]*Buketov Karaganda National Research University, Karaganda, Kazakhstan;*
[2]*Lomonosov Moscow State University, Kazakhstan branch, Astana, Kazakhstan;*
[3]*Ryazan State Radio Engineering University named after V.F. Utkin, Ryazan, Russia;*
[4]*Aktobe Regional University named after K. Zhubanov, Aktobe, Kazakhstan*

A design of an electrostatic mirror energy analyzer for the analysis of charged particle beams based on a newly synthesized field is proposed. The electrostatic field of the analyzer is formed as a superposition of an axially symmetric multipole field and a spherical field. The structure of the electrostatic field formed by the superposition of axially symmetric octupole and spherical fields has been investigated. It is shown that varying the parameters determining the contribution of multipole components allows controlling the aberration properties of the electron-optical system. Conditions for compensating for second- and third-order aberrations have been obtained by selecting appropriate values for the weight coefficients of the hexapole and octupole components, which allows for a significant improvement in the focusing properties of the field. Numerical modeling of the electron-optical system and calculation of charged particle trajectories were carried out using the "FOCUS" simulation program. Two regimes of angular focusing were found. The first mode corresponds to second-order angular focusing at a particle input angle of 68°, while the second regime implements third-order focusing at an input angle of 90°. The instrumental functions of the device were constructed, and the relative energy resolutions and luminosities of the analyzer were evaluated. The proposed electron-optical schemes can be used in the development of high-resolution spectrometers for analyzing charged particle beams in space research, as well as spectrographs for the energy-angle analysis of solid surfaces.

Keywords: charged particle energy analyzer, multipole approach, electrostatic field, numerical modeling, trajectory analysis

✉*Corresponding author*: Kambarova, Zhanar, kambarovazht@gmail.com

Introduction

Modern research in the fields of plasma physics, space technology, and accelerator technology is closely linked to the task of diagnosing charged particle beams. In outer space, charged particle beams are formed under the influence of complex electromagnetic processes and carry information about the state of plasma, solar activity, and the interaction of magnetospheres with the solar wind. To study them, high-precision instruments capable of measuring the energy characteristics of particles over a wide range of energies are required. One of the key tools used in such studies is an energy analyzer that operates by controlling particle trajectories in electrostatic and magnetic fields [1].

The development of energy analyzers is becoming particularly relevant in the context of expanding space missions and increasing requirements for measurement accuracy. Modern devices must provide high energy resolution, stable operation, and compact dimensions. In addition, the development of numerical modeling methods for electron-optical systems allows the creation of new types of analyzers with improved characteristics.

A number of recent studies have presented various types of energy analyzers, including spherical, cylindrical, and toroidal configurations used for space experiments [2–5]. For example, top-hat analyzers are widely used in space missions due to their wide viewing angle and high sensitivity, which makes them effective for recording particle distributions in three-dimensional space [6, 7]. In addition, specialized devices are being developed to measure the energy spectra of ions and electrons in rarefied plasma conditions, which require high accuracy and resistance to external influences. Thus, the development and study of electrostatic energy analyzers for determining the energy characteristics of charged particle beams is a relevant scientific problem that is important both for fundamental research in plasma physics and for practical applications in accelerator technology and charged particle beams diagnostics.

One perspective direction in the development of charged particle energy analyzers is the use of a multipole approach to synthesize new electrostatic fields. A significant contribution to the development of this approach has been made in [8, 9], where the use of multipole configurations to improve the focusing properties of analyzers is proposed. These studies show that the superposition of multipole fields with axially symmetric electrostatic fields, in particular cylindrical ones, allows the formation of effective focusing systems and increases the energy resolution of electron devices. This approach was further developed in works devoted to multipole-cylindrical field configurations.

In previous studies by the authors, considerable attention was paid to the analysis of electrostatic energy analyzers based on the use of multipole-cylindrical fields. In particular, multipole-cylindrical fields, which are a superposition of multipole and axially symmetric cylindrical fields, have proven effective in forming the focusing properties of the working field of an energy analyzer and controlling the trajectories of charged particles. A number of studies [10–12] have shown that the use of multipole-cylindrical fields can significantly improve the characteristics of energy analyzers by increasing the focusing accuracy and reducing aberrations.

This work proposes a new configuration of an electrostatic field based on the superposition of multipole and spherical fields. Unlike previously studied multipole-cylindrical systems, this configuration has enhanced capabilities for controlling aberrations in the electron-optical system. This allows for significant improvement in the focusing properties of the field and increased efficiency in the energy analysis of charged particle beams.

The aim of this work is to study the theoretical development of an electrostatic energy analyzer based on a field formed by the superposition of multipole and spherical fields, as well as to investigate the focusing properties of the system.

Materials and Methods

The axially symmetric field $U(\rho, \xi)$ satisfies Laplace's equation, whose differential operator is the sum of two operators separated by coordinates ρ and ξ: $\Delta = T + \tau$ [8]. In the case of spherical coordinates, operators T and τ are defined by the formulas:

$$T = \frac{d}{d\rho}\left[(1+\rho)^2 \frac{d}{d\rho}\right];$$

$$\tau = \frac{1}{\sin\theta}\frac{d}{d\theta}\left[\sin\theta \frac{d}{d\theta}\right]. \quad (1)$$

Let us introduce a set of functions $f_n(\rho)$ and $\varphi_n(s)$, accepting the following rules for their generation:

$$Tf_n = -f_{n-1}, \quad (2)$$

$$\tau\varphi_n = \varphi_{n-1}, \quad (3)$$

where $n = 1, 2, 3, \ldots$.

Solutions to equations $Tf_0 = 0$, $\tau\varphi_0 = 0$ were used as basic functions.

A function of two variables $V_n(\rho, s)$, constructed from elements of sets (2) and (3), is harmonic, i.e., it satisfies the condition $\Delta V_n = 0$:

$$V_n(\rho, s) = \varphi_n f_0 + \varphi_{n-1} f_1 + \varphi_{n-2} f_2 + \ldots + \varphi_1 f_{n-1} + \varphi_0 f_n = \sum_{m=0}^{n} \varphi_{n-m} f_m. \tag{4}$$

The coordinate $s = \theta$ is the azimuth angle in the spherical coordinate system, in the symmetry plane of the field $\theta = \pi/2$. The fundamental solution of Laplace's equation in this case is the function $f_0 = \frac{1}{1+\rho} - 1$, satisfying the condition $f_0(0) = 0$ on the sphere $\rho = 0$. In accordance with rules (2)–(4) of the spherical quadrupole, hexapole, and octupole fields:

$$U_q(\rho, \theta) = \ln(\sin\theta) + 1 - \ln(1+\rho) - \frac{1}{1+\rho}, \tag{5}$$

$$U_h(\rho, \theta) = \left[2 - \ln(\sin\theta)\right]\left[1 - \frac{1}{1+\rho}\right] - \ln(1+\rho)\left[1 + \frac{1}{1+\rho}\right]. \tag{6}$$

$$\begin{aligned} U_{oct}(\rho, \theta) = {} & \frac{1}{2}\left[\ln(\sin\theta)\right]^2 - \frac{1}{2}\left[\ln\left(\tan\frac{\theta}{2}\right)\right]^2 + \left[\ln(1+\rho) + \frac{1}{1+\rho} - 2\right]\ln(\sin\theta) + \\ & + \frac{1}{2}\left[\ln(1+\rho)\right]^2 - 2\ln(1+\rho) - \frac{1}{2(1+\rho)^2} - \frac{1}{1+\rho} + \frac{3}{2}. \end{aligned} \tag{7}$$

Results and Discussion

Figure 1 shows the family of equipotentials of the spherical octupole $U_{oct}(\rho, \theta)$. For convenience, Cartesian coordinates $x = (1 + \rho)\sin\theta$, $y = (1 + \rho)\cos\theta$ are used. The figure shows that the field is divided into four regions with potentials of opposite signs. Here, the field is calculated only in one half-plane.

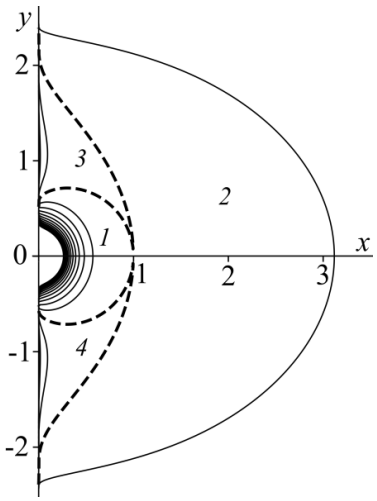

Figure 1. Family of equipotentials of the spherical octupole $U_{oct}(x, y)$:
1, 2 and 3, 4 are regions of potentials of opposite signs

The dynamics of changes in the structure of the electrostatic field formed by the superposition of an axially symmetric octupole and spherical fields has been investigated. Particular attention is paid to the influence of the parameter μ, which determines the relative contribution of the spherical component. The potential of the total field, which is a superposition of the spherical octupole (7) and the spherical field

$$U(x, y) = U_{oct}(x, y) + \mu\left[\frac{1}{\sqrt{x^2 + y^2}} - 1\right], \tag{8}$$

where μ is the coefficient that determines the weight contribution of the spherical field.

The equipotential families of the octupole-spherical field (8), formed by the superposition of an axially symmetric octupole and a spherical field, have been calculated (Figs. 2 and 3).

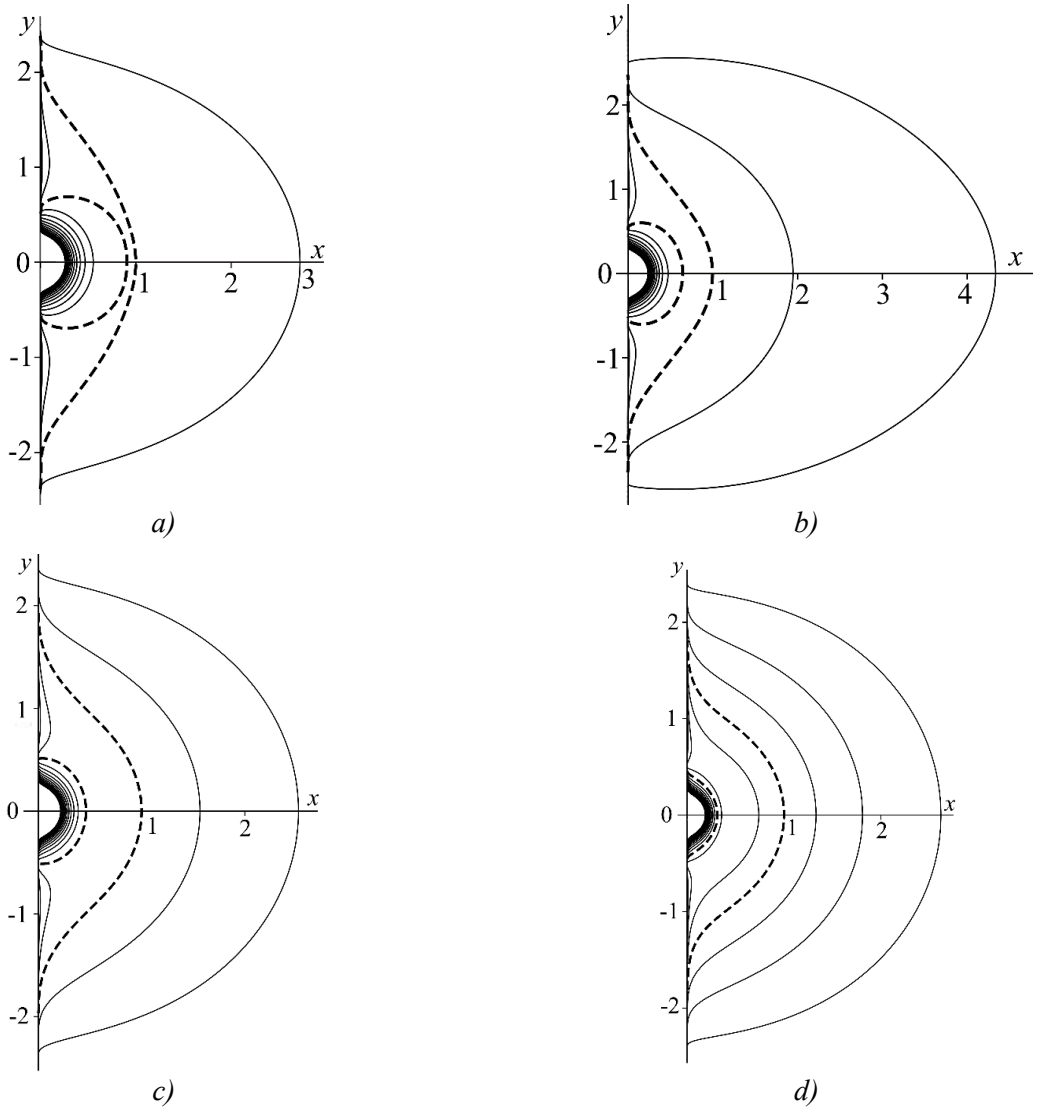

Figure 2. Equipotential octupole-spherical field:
a — μ = 0.1; *b* — μ = 0.5; *c* — μ = 1; *d* — μ = 1.75

It has been shown that at low values of the parameter μ, the field retains the characteristic features of octupole symmetry. The contribution of the spherical component is perturbative and does not lead to a significant restructuring of the field. It has been established that with an increase in μ, the equipotential lines are deformed due to the strengthening of the radially symmetric contribution of the spherical field. In the range of intermediate values of the parameter, a noticeable change in the configuration of equipotential lines is observed, associated with the simultaneous influence of the octupole and spherical components. With a further increase in μ, the spherical component begins to dominate, as a result of which the equipotential lines acquire a quasi-radial character, and the octupole structure is almost completely suppressed. Thus, the parameter μ determines the nature of the spatial distribution of the potential and ensures the transition from a field with a pronounced angular dependence to a field with predominant radial symmetry.

Unlike the case of positive μ values, where the spherical field enhances radial symmetry, negative values (Fig. 3) result in increased non-uniformity of the potential distribution and more complex deformation of the field structure.

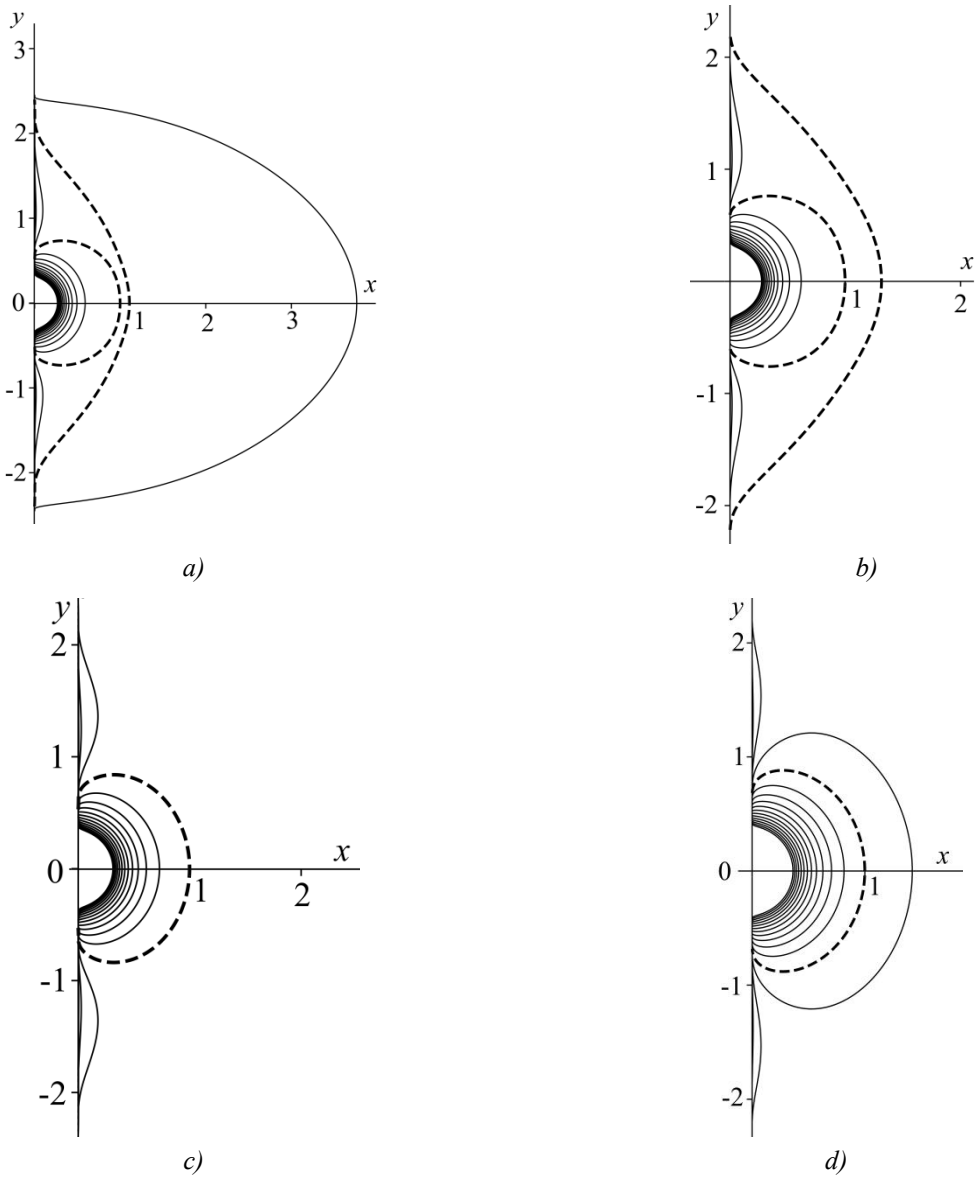

Figure 3. Equipotential octupole-spherical field: *a* — μ = –0.1; *b* — μ = –0.5; *c* — μ = –1; *d* — μ = –2

To construct an energy analyzer with specified characteristics, it is necessary to know the field distribution and determine the shape of the deflecting electrodes throughout the entire working volume of the device, which significantly exceeds the localization area of the analyzed beam. The field of the energy analyzer is considered as a superposition of multipoles and a spherical field:

$$\frac{U(\rho,\xi)}{U_0} = g(\rho,\xi) = U_0(\rho,\xi) + qU_q(\rho,\xi) + \beta U_h(\rho,\xi) + \omega U_{oct}(\rho,\xi) + dU_d(\rho,\xi) + ..., \quad (9)$$

where $U_0(\rho, \xi)$ is the base field, and $U_q(\rho, \xi)$, $U_h(\rho, \xi)$, etc. are components of an axially symmetric multipole field; q, β, ω, d are the weighting coefficients of the multipole components.

Table 1 shows the values of the decomposition coefficients (9), representing the contribution of each multipole component.

Table 1

Decomposition coefficients (9) for multipole components

ε_i	Spherical field $1-\frac{1}{1+\rho}$	Quadrupole $q\frac{\partial U_q}{\partial\rho}\Big\|_{\rho=0}$	Hexapole $\beta\frac{\partial U_h}{\partial\rho}\Big\|_{\rho=0}$	Octupole $\omega\frac{\partial U_{oct}}{\partial\rho}\Big\|_{\rho=0}$
ε_1	–2	–q	0	0
ε_2	3	2q	–β/2	0
ε_3	–4	–3q	4β/3	ω/6
ε_4	5	4q	–29β/12	–ω/2

The data in Table 1 shows that connecting a quadrupole component to the base field affects the parameters of the energy analyzer calculated in the first approximation, connecting a hexapole component affects the parameters starting from the second approximation, and connecting an octupole component affects the parameters starting from the third approximation.

Hexapole and octupole components are added to the basic electrostatic spherical field (quadrupole component is absent):

$$g(\rho,\xi)=1-\frac{1}{1+\rho}+\beta U_h+\omega U_{oct}. \tag{10}$$

Image smearing in focus is determined by angular aberrations. With an increase in the angular divergence of the charged particle beam, the greatest contribution to image smearing is made by cubic aberration, which limits the resolution and thus the sensitivity of the device.

The introduction of these multipole components affects the aberration coefficients of the second and higher orders, enabling their targeted control and optimization of the electron-optical characteristics of the system.

The coefficient of quadratic angular aberrations that smear the image of the source in the radial plane is determined by the following formula:

$$A_{II}(\varphi)=-\frac{K}{2\eta^2}\left[1-\cos\sqrt{\eta}\varphi\right]+\frac{1+\frac{K}{2\eta}}{3\eta}\left[\cos\sqrt{\eta}\varphi-\cos 2\sqrt{\eta}\varphi\right], \tag{11}$$

cube aberration coefficient is determined by the following formula:

$$A_{III}(\varphi)=\frac{\pi}{2\eta^2\sqrt{\eta}}\left[\frac{1}{3}\left(4\eta+K+\frac{5}{2}\frac{K^2}{\eta}\right)-\frac{3}{4}Q-\eta(1+\eta)-\frac{\eta}{2}\right], \tag{12}$$

where $\eta=3+\varepsilon_1$, $K=6+4\varepsilon_1+\varepsilon_2$, $Q=4+6\varepsilon_1+4\varepsilon_2+\varepsilon_3$.

According to Table 1, the decomposition coefficients (9) are: $\varepsilon_1=-2$, $\varepsilon_2=3-\frac{\beta}{2}$, $\varepsilon_3=-4+\frac{4}{3}\beta+\frac{1}{6}\omega$. The weight components β and ω are found based on the requirement that the quadratic and cubic aberrations be zero: $A_{II}=A_{III}=0$. It is determined that β = 3, ω = 3. With these values, simultaneous compensation of second- and third-order aberrations is achieved, which improves the focusing properties of the energy analyzer.

In the case of β = 3, ω = 3, the equipotential equation for the following field is obtained:

$$g=\frac{1}{\sqrt{x^2+y^2}}-1+\beta U_h+\omega U_{oct}. \tag{13}$$

Numerical modeling of the electron-optical scheme of an electrostatic mirror energy analyzer was performed, implementing a field configuration in the form of a superposition of multipoles and spherical components. The modeling was performed using the "FOCUS" software package [13], designed to calculate axially symmetric corpuscular-optical systems and analyze the trajectories of charged particles in electrostatic fields.

The geometry of the analyzer's electrode system was determined based on the equipotential surfaces of the field formed by the superposition of multipole and spherical components. An electrostatic field is formed between the electrodes, with a deflecting potential $U = \text{const}$ applied to the outer electrode. The source of charged particles is located on the axis of the device.

Figure 4 shows the distribution of electrostatic potential in the electron-optical system of the energy analyzer. The field is calculated by numerically determining the potential values at the nodes of the discretized region. For a clear presentation of the results, a color scale is used, in which higher potential values correspond to warm shades, and lower values correspond to cold shades.

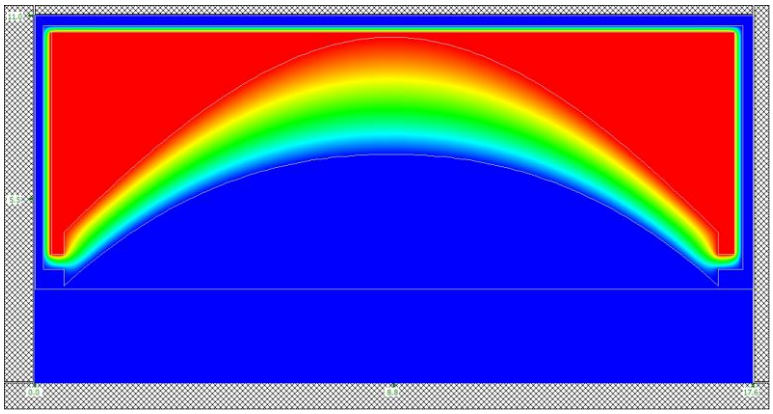

Figure 4. Distribution of the electrostatic field in the electron-optical scheme of an energy analyzer based on an octupole-spherical field

In the first of the operating regimes found, the angle of incidence of the central trajectory is 68°, and the spread of the angle of incidence of the particles relative to the trajectory of the central particle is ±4°. In this regime, the electron-optical scheme implements second-order "axis-ring" type angular focusing: according to the scheme, a beam of charged particles with energy $E/V = 0.5$ enters the analysis field from a point electron-optical source *1*. As a result of reflection from the field, charged particles are focused into a ring image *5* and enter the detector *6* (Fig. 5). By changing the deflection potential of the upper electrode, we obtain the energy spectrum of particles in the analyzed beam.

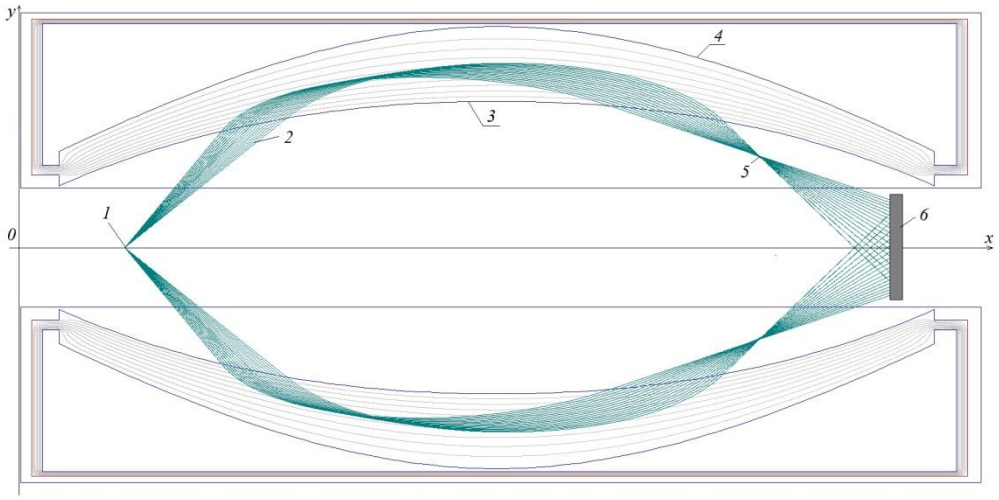

1 — point source; *2* — particle trajectories; *3* — inner electrode;
4 — outer deflection electrode; *5* — ring image; *6* — detector

Figure 5. Trajectories of charged particles in an energy analyzer (regime 1, central entrance angle 68°)

The instrumental function of the device *N(E),* characterizing the dependence of the number of registered particles on the relative energy, is shown in Figure 6. The relative energy resolution of the analyzer in this regime is $\Delta E/E = 2$ % at a luminosity of $\Omega/2\pi = 13$ %.

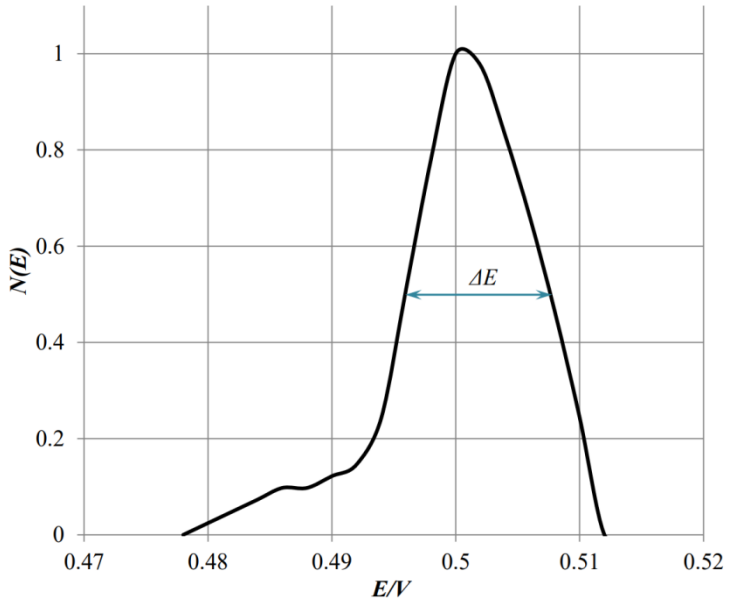

Figure 6. Instrumental function in 2nd order angular focusing regime
(regime 1, central entrance angle 68°)

The second operating regime of the analyzer implements third-order angular "axis-ring" type focusing at a particle input angle of 90° (Fig. 7). In this regime, the analyzer operates as follows: a beam of charged particles emerging from a point source *1* with a 180° angle of divergence in a plane perpendicular to the symmetry axis and with a 90°±3° angular divergence in the axial plane enters the analyzer field. As a result of reflection from the field, a ring image *5* is formed. The equality of the angle of inclination of the axial trajectory 90° at the analyzer input ensures the achromatic mode of the device.

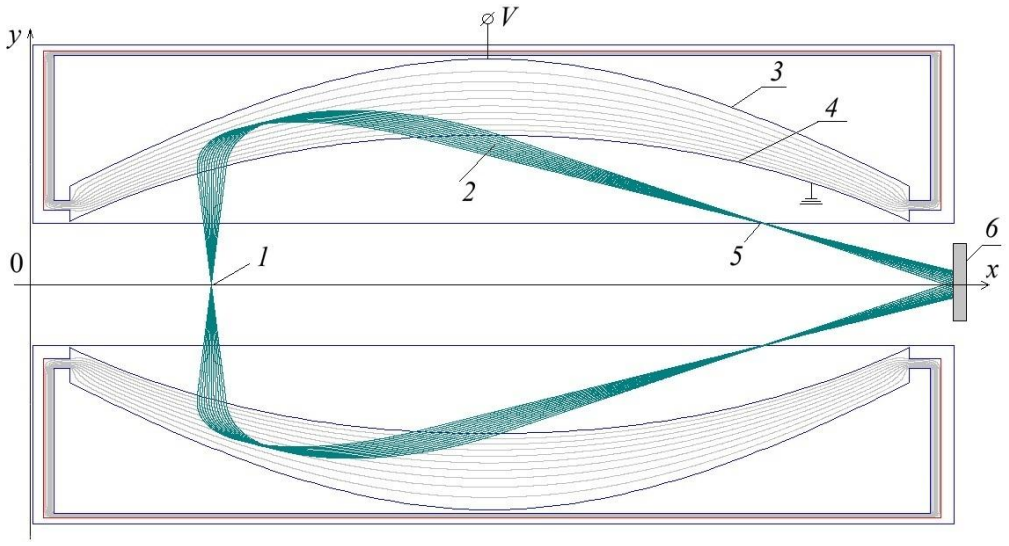

1 — point source; *2* — particle trajectories; *3* — outer deflecting electrode;
4 — inner electrode; *5* — ring image; *6* — detector

Figure 7. Trajectories of charged particles in an energy analyzer (regime 2, input angle 90°)

The instrumental function of the analyzer in this regime is shown in Figure 8. In this focusing regime, the analyzer achieves a relative energy resolution of $E/\Delta E = 1.8$ at a luminosity of $\Omega/2\pi = 10$ %.

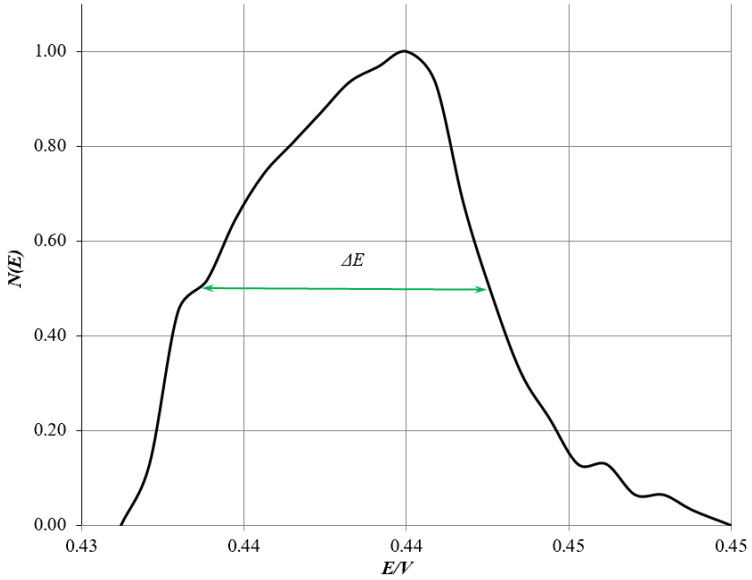

Figure 8. Instrumental function in 3rd order angular focus regime (regime 2, input angle 90°)

This electron-optical scheme is suitable for constructing a spectrograph simultaneously by energy and by the polar angle of particle emission, which is of considerable interest for studying the surface of solids using electron spectroscopy methods.

Thus, profiling the analyzer electrodes in accordance with function (13) is a sufficient condition for compensating for the quadratic and cubic aberrations. This ensures high-order focusing without the introduction of additional corrective elements.

Conclusion

The structure of the electrostatic field obtained by superposition an axially symmetric octupole and a spherical field has been investigated.

It has been established that in the proposed electrostatic energy analyzer, based on the superposition of a spherical field and multipoles, the selection of coefficients β and ω, which determine the weight contributions of the axially symmetric hexapole and octupole, allows controlling second- and third-order aberrations and compensating for angular quadratic and cubic aberrations.

Modeling of electron-optical scheme performed by the “Focus” program confirmed the feasibility of an electron-optical scheme of energy analyzer based on the superposition of axially symmetric multipoles and a spherical field. The proposed electron-optical system implements two independent operating regime: second-order focusing at a central entrance angle of 68° and third-order focusing at an input angle of 90°. The results obtained demonstrate the promise of using the superposition of multipole components and spherical field as a tool for targeted control of the aberration properties of electrostatic mirror analyzers.

Acknowledgement

This research was funded by the Science Committee of the Ministry of Science and Higher Education of the Republic of Kazakhstan (Grant No. AP26101393).

References

1 Humphries, & Stanley, Jr. (1990). Charged particle beams. New York, Wiley-Interscience. *massless.info*. Retrieved from https://massless.info/images/charged_particle.pdf

2 Halekas, J.S., Hansen, C., Ruhunusiri, S., et al. (2025). The TRACERS Analyzer for Cusp Electrons. *Space Sci Rev*, *221*, 21. https://doi.org/10.1007/s11214-025-01147-9

3 Fuselier, S.A., Freeman, M.A., Kletzing, C.A., Christopherson, S.R., Covello, M.J., De Luna, D., Doty, R.L., et al. (2025). The Analyzer for Cusp Ions (ACI) on the TRACERS Mission. *Space Sci Rev., 221*(2), 30. https://doi.org/10.1007/s11214-025-01154-w

4 Yokota, S., Kitamura, Y., & Terada, K., et al. (2026). Ion optics of a single pair of angular scanning deflectors for space plasma instruments. *Earth Planets Space, 78*, 20. https://doi.org/10.1186/s40623-026-02366-2

5 Hénaff, G., & Berthomier, M. (2025). Parametric study of the performance of ±45° an electrostatic analyzer with an hemispheric field-of-view based on the donut topology. *Journal of Geophysical Research: Space Physics, 130*, e2024JA033367. https://doi.org/10.1029/2024JA033367

6 Dai, L., Kong, L., & Zhang, A., et al. (2025). The Light Ion Analyzer (LIA) for the SMILE Mission. *Space Sci Rev, 221*, 109. https://doi.org/10.1007/s11214-025-01235-w

7 Rankin, J.S., McComas, D.J., & Alimaganbetov, M., et al. (2025). Solar Wind and Pickup Ion (SWAPI) Instrument on NASA's Interstellar Mapping and Acceleration Probe (IMAP). *Space Sci Rev, 221*, 108. https://doi.org/10.1007/s11214-025-01229-8

8 Zashkvara, V.V., & Tyndyk, N.N. (1996). Potential fields based on circular multipole series. *Nuclear Instruments & Methods in Physics Research. Section A., A370,* 452–460. https://doi.org/10.1016/0168-9002(95)00809-8

9 Zashkvara, V.V., & Tyndyk, N.N. (1992). Electrostatic axially symmetric multipole in deflector-type analyzers. *Nuclear Instruments & Methods in Physics Research. Section A.*, A313, 315–327. https://doi.org/10.1016/0168-9002(92)90806-F

10 Kambarova, Zh.T., Saulebekov, A.O., & Trubitsyn, A.A. (2022). The All-sky Spectrometer of Hot Cosmic Plasma. *The Astronomical Journal, 164*(2), 47(1–10). https://doi.org/10.1088/2631-8695/ad1c0a

11 Kambarova, Z.T., & Saulebekov, A.O. (2018). Calculation of the structure of electrostatic quadrupole-cylindrical fields. *Bulletin of the University of Karaganda – Physics, 1*(89), 66–71. Retrieved from https://phs.buketov.edu.kz/physics-vestnik/article/view/544/449

12 Kambarova, Zh.T., Trubitsyn, A.A., & Saulebekov, A.O. (2018). Axially symmetric energy analyzer based on the electrostatic decapole-cylindrical field. *Technical Physics, 63,* 11, 1667–1671. https://doi.org/10.1134/S1063784218110142

13 Sautbekova, Z., & Trubitsyn, A. (2022). FOCUS CPM software for trajectory analysis of real axially symmetric electrostatic mirrors: methods and algorithms. *Eurasian Physical Technical Journal*, *19*(3(41), 91–96. https://doi.org/10.31489/2022No3/91-96

М.К. Тунгушбекова, Ж.Т. Камбарова, А.А. Трубицын,
А.О. Саулебеков, Т.Ж. Шугаева

Мультипольді-сфералық өрістерге негізделген электрстатикалық энергия талдағыштарды жобалау және оның сипаттамаларын талдау

Зарядталған бөлшектер шоқтарын талдауға арналған жаңа синтезделген өріс негізінде электрстатикалық айна типті энергия талдағыштың сұлбасы ұсынылды. Энергия талдағыштың электрстатикалық өрісі осьтік симметриялы мультипольдік мен сфералық өрістердің суперпозициясы ретінде қарастырылады. Осьтік симметриялы октуполь және сфералық өрістердің суперпозициясы арқылы қалыптасатын электрстатикалық өрістің құрылымы зерттелді. Мультипольдік құраушылардың үлесін анықтайтын параметрлерді өзгерту электрондық-оптикалық жүйенің аберрациялық қасиеттерін басқаруға мүмкіндік беретіні көрсетілді. Гексаполь және октуполь құраушыларының салмақтық коэффициенттерінің сәйкес мәндерін таңдау арқылы екінші және үшінші ретті аберрацияларды компенсациялау шарттары алынды, бұл өрістің тоғыстаушы қасиеттерін едәуір жақсартуға мүмкіндік береді. «Focus» сандық бағдарламасының көмегімен электронды-оптикалық жүйеге сандық моделдеу жүргізіліп, зарядталған бөлшектердің қозғалыс траекториялары есептелген. Бұрыштық тоғыстаудың екі режимі анықталды. Бірінші режим бөлшектердің енгізу бұрышы 68° болған кезде екінші ретті бұрыштық тоғыстауға сәйкес келеді, ал екінші режим енгізу бұрышы 90° болғанда үшінші ретті тоғыстауды жүзеге асырады. Құрылғының аппараттық функциялары құрылып, талдағыштың және сұлбаның салыстырмалы энергетикалық ажырату қабілеті мен жарық күші бағаланды. Ұсынылған электрондық-оптикалық сұлбалар ғарыштық зерттеулерде зарядталған бөлшектер ағындарын талдауға арналған жоғары ажыратымдылықты спектрометрлерді және қатты денелер бетінің энергия-бұрыштық талдауына арналған спектрографтарды әзірлеуде қолданылуы мүмкін.

Кілт сөздер: зарядталған бөлшектердің энергия талдағыштары, мультипольдік тәсіл, электрстатикалық өріс, модельдеу, траекториялық талдау

М.К. Тунгушбекова, Ж.Т. Камбарова, А.А. Трубицын,
А.О. Саулебеков, Т.Ж. Шугаева

Проектирование и анализ характеристик электростатического энергоанализатора на основе мультипольно-сферических полей

Предложена схема электростатического зеркального энергоанализатора для анализа пучков заряженных частиц на основе нового синтезированного поля. Электростатическое поле энергоанализатора представляет собой суперпозицию осесимметричного мультиполя и сферического поля. Исследована структура электростатического поля, формируемого суперпозицией осесимметричного октупольного и сферического полей. Показано, что изменение параметров, определяющих вклад мультипольных компонентов, позволяет управлять аберрационными свойствами электронно-оптической системы. Получены условия компенсации аберраций второго и третьего порядков за счёт выбора соответствующих значений весовых коэффициентов гексапольной и октупольной составляющих, что позволяет существенно улучшить фокусирующие свойства поля. С помощью программы «Focus» проведено численное моделирование электронно-оптической системы и расчет траекторий движения заряженных частиц. Найдены два режима угловых фокусировок. Первый режим соответствует угловой фокусировке второго порядка при угле ввода частиц 68°, второй режим реализует фокусировку третьего порядка при угле ввода 90°. Построены аппаратные функции прибора, оценены относительные энергетические разрешения и светосилы анализатора. Предложенные электронно-оптические схемы могут быть использованы при разработке высокоразрешающих спектрометров, предназначенных для анализа потоков заряженных частиц в космических исследованиях, и спектрографов для энергоуглового анализа поверхности твердых тел.

Ключевые слова: энергоанализатор заряженных частиц, мультипольный подход, электростатическое поле, моделирование, траекторный анализ

Information about the authors

Tungushbekova, Meiramkul — PhD student, Master, Faculty of Physics and Technology, Buketov Karaganda National Research University, Karaganda, Kazakhstan; e-mail: mtungushbekova@mail.ru. ORCID ID: https://orcid.org/0009-0002-3410-2454

Kambarova, Zhanar *(corresponding author)* — PhD, Professor, Faculty of Physics and Technology, Buketov Karaganda National Research University, Karaganda, Kazakhstan; e-mail: kambarova-zht@gmail.com. SCOPUS Author ID: 55543382800; ORCID ID: 0000-0001-9808-5484

Trubitsyn, Andrey — Doctor of Physical and Mathematical Sciences, Professor, Ryazan State Radio Engineering University named after V.F. Utkin, Ryazan, Russia; e-mail: assur@bk.ru. SCOPUS Author ID: 6604053991, ORCID ID: https://orcid.org/0000-0002-9337-8947

Saulebekov, Arman — Doctor of Physical and Mathematical Sciences, Professor, Lomonosov Moscow State University, Kazakhstan branch, Astana, Kazakhstan; e-mail: saulebekov@mail.ru. SCOPUS Author ID: 6505502480, ORCID ID: https://orcid.org/0000-0002-6842-9263

Shugayeva, Tlektes — PhD, Associate Professor, Aktobe Regional University named after K. Zhubanov, Aktobe, Kazakhstan; e-mail: tlektes21@mail.ru. SCOPUS Author ID: 60321990400, ORCID ID: https://orcid.org/0000-0002-4797-4529

Article

UDC 621.762:539.2

https://doi.org/10.31489/2026PH2/38-48

Received: 02.02.2026
Accepted: 10.04.2026

S.A. Ghyngazov[1], I.P. Vasil'ev[1], V.A. Boltueva[1], S. Bobuyok[1], I.K. Chakin[2], V.P. Krivobokov[1]

[1]*National Research Tomsk Polytechnic University, Tomsk, Russia;*
[2]*Budker Institute of Nuclear Physics, Novosibirsk, Russia*

The Influence of Electron Processing of the Powder Mixture of Initial Reagents on the Sintering of High-Entropy Ceramics $(Ca_{0.2}Sr_{0.2}Ba_{0.2}Pb_{0.2}La_{0.2})TiO_3$

The development of thermoelectric materials has attracted considerable attention with the emergence of a new class of high-entropy materials. Their fabrication is typically based on solid-state synthesis and involves prolonged mechanical mixing of powder precursors, high-temperature heat treatment, and multiple repetitions of these operations. The paper addresses the issues of accelerating the manufacturing process of highly entropic ceramics for thermoelectric applications through the use of electron beam processing. The effect of cyclic processing of a powder mixture of initial reagents in air with a high-energy electron beam (E = 1.4 MeV) on the sintering of compacts was studied using high-entropy perovskite ceramics $(Ca_{0.2}Sr_{0.2}Ba_{0.2}Pb_{0.2}La_{0.2})TiO_3$ as an example. The electron beam current was 4 mA (5 treatment cycles) and 5 mA (4 treatment cycles), with mechanical grinding of the powder after each irradiation step. It was found that electron beam treatment enhances the compaction/sintering kinetics. The efficiency of the treatment increases with the number of cycles. As a result, the sintering process is accelerated, leading to increased ceramic density and mechanical strength. These improvements are attributed to the formation of the high-entropy phase $(Ca_{0.2}Sr_{0.2}Ba_{0.2}Pb_{0.2}La_{0.2})TiO_3$ in the powder mixture as a result of electron beam processing.

Keywords: high-entropy ceramics, perovskites, synthesis, electron beams, sintering

✉*Corresponding author*: Ghyngazov, Sergei, ghyngazov@tpu.ru

Introduction

The development of solar energy is largely associated with perovskites [1]. The most well-known representative of this class of materials is calcium titanate ($CaTiO_3$), which is widespread in nature, readily available, and inexpensive [2]. Perovskite solar cells are considered the basis for tandem (e.g., perovskite-silicon) cells, which could significantly increase the efficiency of solar panels and make solar energy more accessible. One of the main drawbacks of conventional perovskites is their instability at high temperatures [3]. Perovskite materials, especially those based on lead methylammonium iodide, tend to degrade rapidly when exposed to moisture, oxygen, high temperatures, and intense sunlight [4]. This leads to the destruction of their crystal structure and a loss of efficiency, making them less durable compared to traditional silicon solar cells. For example, modern silicon panels lose about 0.5 % of their power per year, while perovskite cells can lose up to 10 % of their power in just two months of operation. An integrated approach—a combination of defect engineering, composition modification, surface protection, and encapsulation—can significantly improve the efficiency, stability, and environmental safety of perovskite solar cells, bringing them closer to mass commercial use. However, these measures do not completely solve the problem. New prospects for improving the properties of perovskites have emerged with the development of high-entropy ceramics. The concept of creating a high-entropy state was first successfully implemented in alloys [5]. Outstanding achievements in producing alloys with unique properties have stimulated research into the creation of high-entropy ceramics [6]. High-entropy ceramics (HECs) are materials composed of five or more elements that form a homogeneous crystalline structure. Due to their unique combination of properties, such as high thermal stability, wear resistance, low thermal conductivity, high strength, and permittivity, they find application in a wide range of fields. In aerospace engineering, HECs are used as thermal barrier coatings and structural components for operation under ultra-high temperatures and loads, for example, in engines, nozzles, and thermal protection systems [7]. In the energy industry, they are employed in the manufacture of solid oxide fuel cell components, high-temperature insulation materials [8], and energy storage systems [9]. Additionally, HECs

and their oxides serve as catalysts for chemical reactions, including those involved in energy purification and conversion processes. Transparent high-entropy ceramics can be used as protective coatings for optics, screens, and semiconductor devices due to their plasma resistance and low etching rate [10]. The properties of thermoelectric materials have been improved thanks to the development of high-entropy perovskites [11]. These materials constitute a new class of compounds whose crystal structure contains five or more different elements in approximately equal proportions in one or both cationic sublattices. This composition provides high configurational entropy, which stabilizes the structure and imparts unique properties. Therefore, the synthesis and sintering of high-entropy perovskite materials has become a particularly pressing issue. The technology for synthesizing high-entropy perovskites typically involves the following basic steps, which form the basis of solid-phase synthesis [12, 13]. Initially, the starting oxide powders are mechanically mixed in a stoichiometric ratio using a planetary ball mill. The powder mixture is then fired and reground in the mill; this process may be repeated several times to ensure homogeneity. After milling, the dispersed powders are used to form compacts of a given shape (green bodies). The ceramics are subsequently sintered from these compacts, followed by prolonged annealing of the ceramic billets at high temperature in an inert atmosphere. This annealing step enhances the conductive properties of the material, which is essential for its performance as a thermoelectric. As can be seen from the above, the fabrication process for thermoelectric materials is very time-consuming and expensive. These drawbacks can be significantly mitigated by accelerating the synthesis and improving the quality of the sintering process. In this work, it is proposed to activate these processes by treating the initial powder mixture of reagents with a powerful beam of high-energy electrons. One of the known methods for activating the sintering of powder compacts is the pretreatment of powders by electron irradiation [14, 15]. Electron treatment of powders is usually carried out in a vacuum, which complicates the technological process. Currently, electron accelerators are available that allow the extraction of electron beams with energies of 1 MeV or more into the air atmosphere [16, 17]. Using such electron beams makes it possible to process powder systems in air with high speed and efficiency [18, 19].

In this work, for the first time, the effect of high-energy electron beam treatment in an air atmosphere on the shrinkage kinetics of compacts made from a powder mixture of initial reagents is investigated.

Materials and Methods

Commercial powders of $CaTiO_3$, $SrTiO_3$, $BaTiO_3$, $PbTiO_3$, La_2O_3, and TiO_2 with a purity of 99.99 % were used as starting materials for the synthesis of high-entropy ceramics with the composition $(Ca_{0.2}Sr_{0.2}Ba_{0.2}Pb_{0.2}La_{0.2})TiO_3$. Simultaneous thermal analysis of these powders was performed using an STA 449 device (Netzsch, Germany). To maintain the specified stoichiometry of the resulting ceramics, a powder mixture was prepared in the molar ratio $4CaTiO_3 + 4SrTiO_3 + 4BaTiO_3 + 4PbTiO_3 + 2La_2O_3 + 4TiO_2$. Mixing of the powders was carried out in a humid environment using a Tencan XQM-2A planetary ball mill. The mixture was then dried in a resistance furnace at a temperature of 150 °C for 2 hours. Part of the powder mixture prepared in this way was left in its original state, while the remaining part was divided into portions and subjected to short-term treatment with high-energy electrons in air using an electron accelerator (Unique scientific installation “Stand ELV-6”, INP SB RAS, Novosibirsk, Russia). The ELV-6 Stand and the electron beam processing technique are described in detail in [20, 21]. The issues of the formation of temperature fields in powder samples, the distribution of energy density, and the depth of electron penetration were previously discussed in detail in [22]. Powder compacts for sintering high-entropy ceramics were obtained by uniaxial pressing on a PGR-10 press at a pressure of 100 MPa. Sintering of $(Ca_{0.2}Sr_{0.2}Ba_{0.2}Pb_{0.2}La_{0.2})TiO_3$ ceramic samples was carried out in air within the furnace chamber of a DIL 402 C dilatometer (Netzsch, Germany) at a temperature of 1200 °C for 5 hours. The heating and cooling rates were 10 °C/min. After electron beam processing at beam currents of 4 mA and 5 mA, the powder was mechanically ground in an agate mortar. The resulting powder was then placed into a massive copper die and again subjected to electron beam processing under identical conditions. This sequence of actions was repeated five times for a current of 4 mA and four times for a current of 5 mA. After each electron beam exposure, a powder sample was taken for the production of powder compacts. To obtain reliable results, all experiments were carried out repeatedly in the amount of at least three.

Results and Discussion

Figure 1 shows the TG and DSC curves for each individual powder (TiO_2, La_2O_3, $BaTiO_3$, $SrTiO_3$, $CaTiO_3$, $PbTiO_3$) included in the powder mixture.

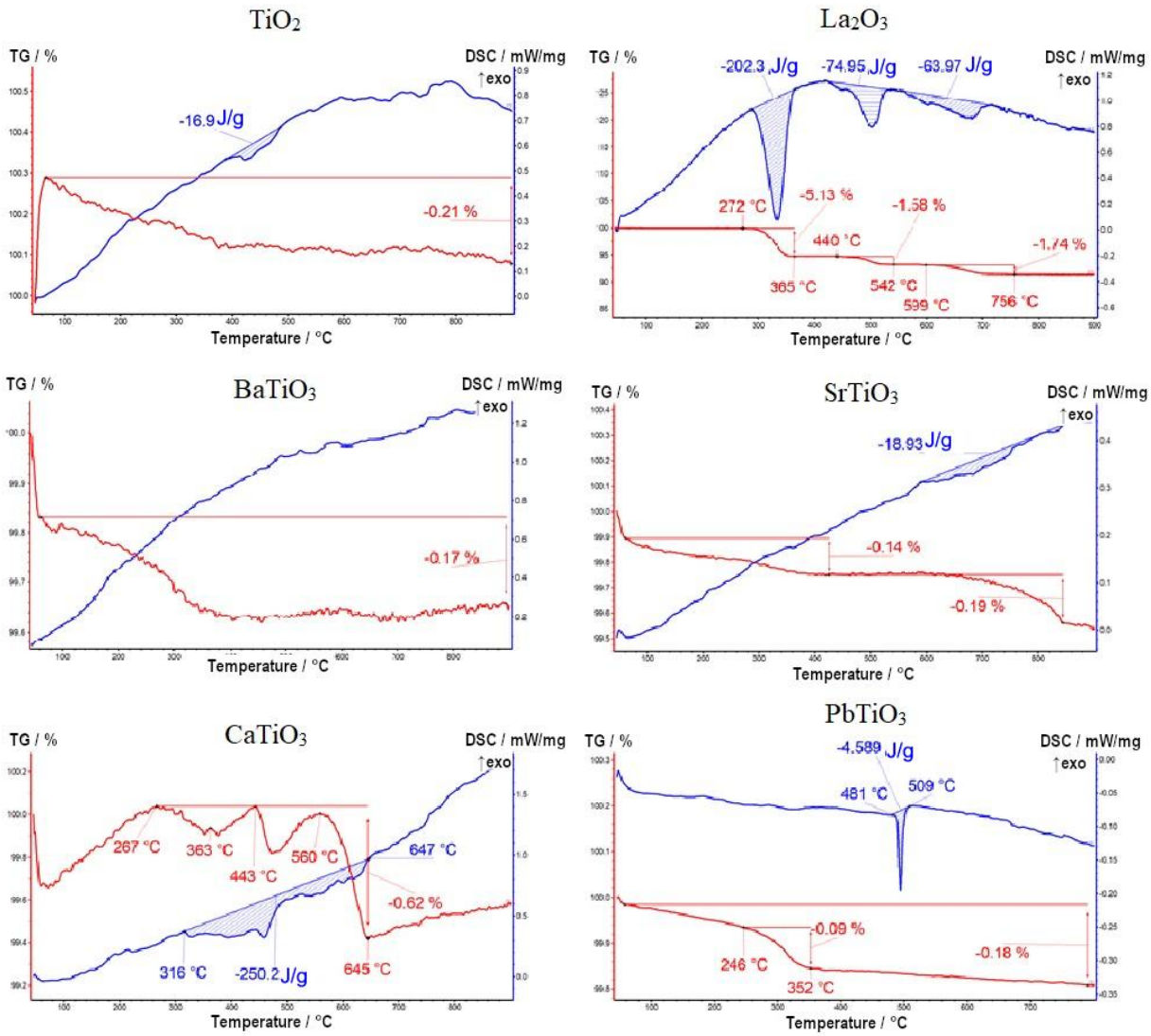

Figure 1. TG and DSC curves for the initial powders used in the synthesis of high-entropy ceramics $(Ca_{0.2}Sr_{0.2}Ba_{0.2}Pb_{0.2}La_{0.2})TiO_3$

Figure 1 shows that for all components of the reaction mixture, except for La_2O_3, the weight loss is less than 1 % and is primarily due to the desorption of adsorbed water. At temperatures below 100 °C, a slight weight loss is observed, which is attributed to the desorption of physically bound water. In the temperature range of 100–500 °C, the removal of loosely bound moisture occurs. For La_2O_3, more significant weight changes are observed, which may be due to its tendency to interact with carbon dioxide and water from the atmosphere via the following mechanism.

$$La_2O_3 + 2CO_2 + H_2O \rightarrow 2LaCO_3(OH).$$

Upon heating, hydroxyl groups are initially eliminated with the release of a water molecule. As the temperature increases further, decarboxylation of the residual carbonate occurs, accompanied by the evolution of carbon dioxide. The overall decomposition process of lanthanum hydroxycarbonate is expressed by the equation:

$$2LaCO_3(OH) \rightarrow La_2O_3 + CO_2 + H_2O.$$

Since the weight loss during heating of the La_2O_3 powder (Fig. 1) is several times greater than that of each of the other powders in the reaction mixture, the shape of the TG and DSC curves for the mixture of initial reagents completely repeats the corresponding curves for pure La_2O_3 powder (Fig. 2).

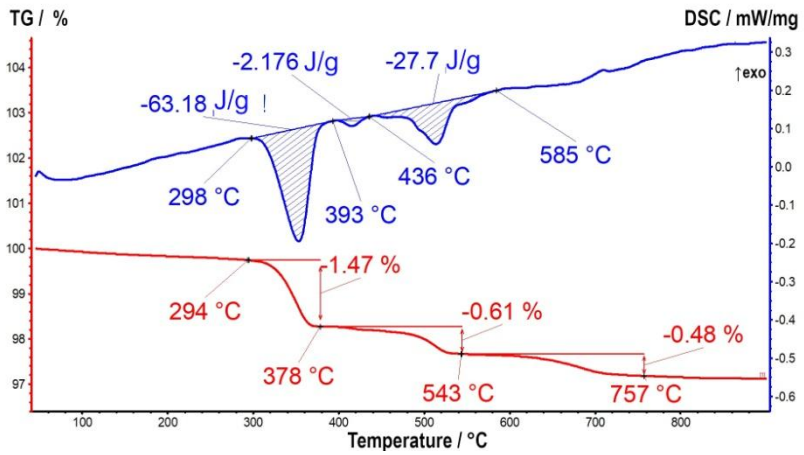

Figure 2. TG and DSC curves for the powder mixture in the molar ratio:
$4CaTiO_3 + 4SrTiO_3 + 4BaTiO_3 + 4PbTiO_3 + 2La_2O_3 + 4TiO_2$

Figure 2 shows the results of TG and DSC analysis for a powder mixture of complex composition: $4CaTiO_3 + 4SrTiO_3 + 4BaTiO_3 + 4PbTiO_3 + 2La_2O_3 + 4TiO_2$. According to the TG data, the slight weight loss observed at temperatures below 100 °C is associated with the removal of physically adsorbed moisture from the surface of the powder particles. The sharp decrease in weight in the temperature range of 300–360 °C is mainly due, as described above, to the weight loss of lanthanum oxide present in the powder mixture as a result of the release of H_2O and CO_2. A less pronounced weight loss in the temperature range of 400–600 °C can be explained by the combustion of residual organic matter and the removal of residual moisture. The occurrence of these processes is confirmed by the presence of corresponding endothermic peaks on the DSC curve (Fig. 2). Thus, the results of simultaneous thermal analysis demonstrate that, upon heating the powder mixture to the sintering temperature, no decomposition of the titanates occurs. The minor weight loss observed is attributed to the release of previously adsorbed moisture and the products of the decomposition of lanthanum hydroxycarbonate and lanthanum oxide. This result confirms literature data on the high-temperature stability of all selected reagents.

Figure 3 shows photographs of a massive copper container holding a powder mixture before (Fig. 3*a*) and after treatment with a 1.4 MeV electron beam (Fig. 3*b* and 3*c*). The electron beam current was 4 mA, and the container moved under the beam at a speed of 1 cm/s. The beam itself was scanned across the internal width of the container at a frequency of 50 Hz.

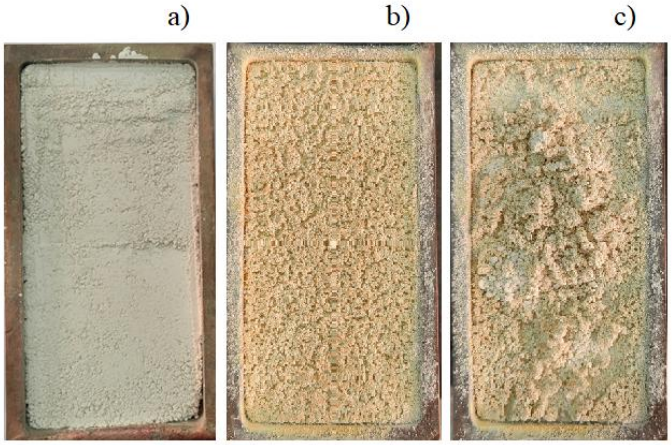

Figure 3. Photographs of the container before (*a*) and after (*b*, *c*) treatment with a 1.4 MeV electron beam. Beam current: 4 mA; container movement speed under the beam: 1 cm/s

Figure 3*c* shows the structure within the irradiated powder layer (part of the powder was swept toward the center of the container). It is evident that, as a result of brief electron-beam heating, the powder mixture changed color, and the powder grains entered into solid-phase interactions with each other. This is evidenced

by the formation of a highly porous plate (Fig. 3*b*), which readily disintegrates into large particles in the form of agglomerates of smaller particles (Fig. 3*c*). The absence of melting droplets in the electron-treated powder (Figs. 3*b* and 3*c*) indicates that the temperature of the powder mixture did not reach the melting point of any of its components during electron-beam heating. The mechanical adhesion of the powder particles indicates that interparticle solid-phase interactions occurred. SEM images of the powder mixture particles and EDS spectra of the main elements of the powder particles after the first and fourth irradiation/grinding cycles are shown in Figure 4 and Figure 5, respectively. The treatment included electron beam irradiation at E = 1.4 MeV, beam current I = 5 mA, scan speed V = 1 cm/s, and subsequent grinding in an agate mortar.

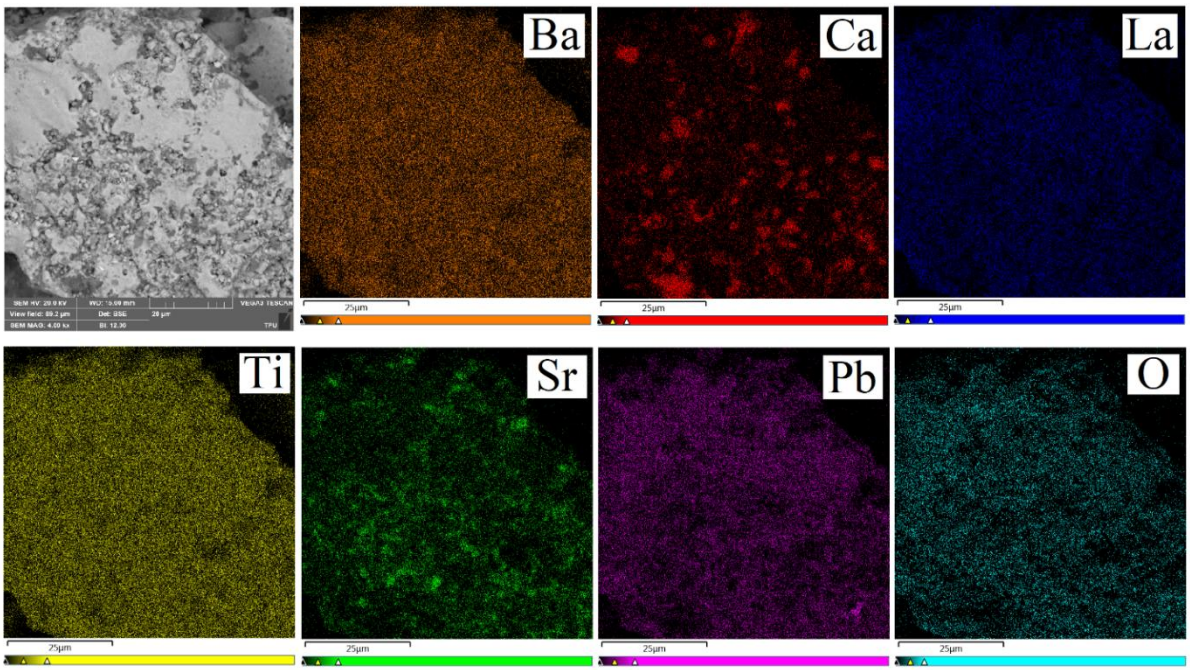

Figure 4. SEM image of a powder mixture particle and the corresponding EDS spectrum of the main elements after the first processing cycle (E = 1.4 MeV, I = 5 mA, V = 1 cm/s)

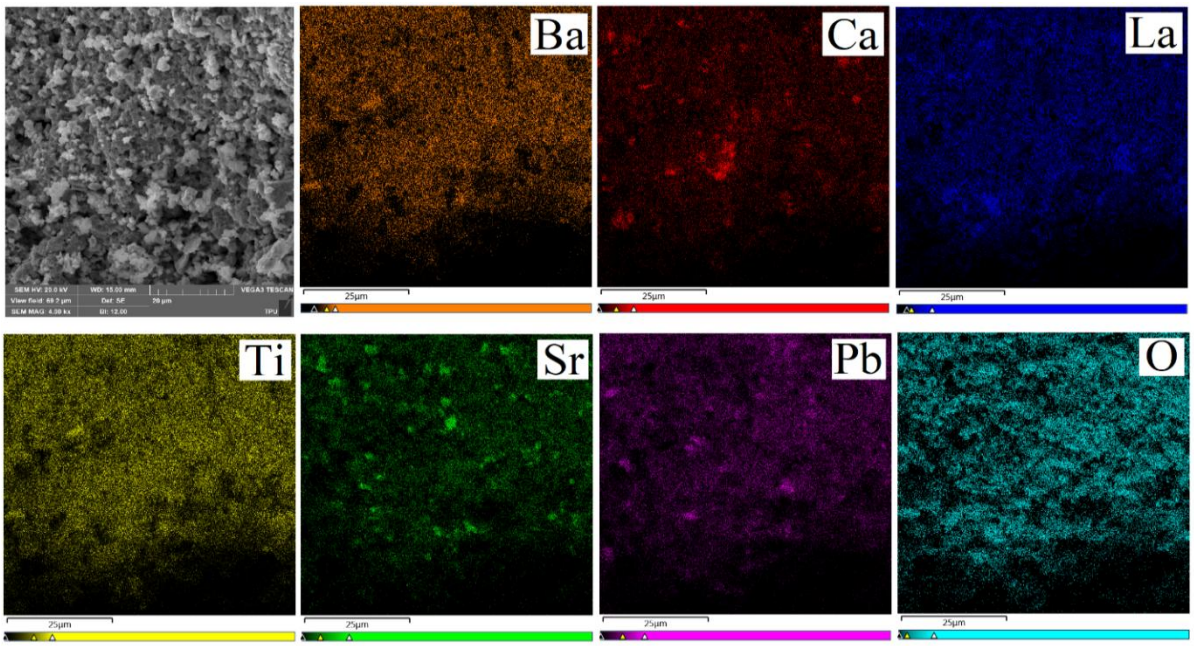

Figure 5. SEM image of a powder mixture particle and the corresponding EDS spectrum of the main elements after the fourth processing cycle (E = 1.4 MeV, I = 5 mA, V = 1 cm/s)

The SEM image in Figure 4 shows that after a single short-term exposure to the electron beam, the mixture consists of particle agglomerates, and the agglomerate surface is partially melted. The occurrence of solid-phase interparticle interaction during a single treatment can be judged from the analysis of the XRD data presented in Figure 6. For a beam current of 5 mA, the diffraction pattern has a shape corresponding to ceramics of the composition $(Ca_{0.2}Sr_{0.2}Ba_{0.2}Pb_{0.2}La_{0.2})TiO_3$ [22]. The data in Figure 5 indicate a change in the structure of the mixture particles after four irradiation cycles with an electron beam at $I = 5$ mA. The SEM image of the particles is typical of sintered ceramics. The distribution of the main elements by volume for all elements except Ca and Sr is characterized by high uniformity. The X-ray diffraction results are shown in Figure 6. The clean sharp peaks for samples sintered from electron-untreated powders indicate that a homogeneous phase was formed due to atomic diffusion over a period of 5 hours. Figure 6 also shows that the same type of diffraction pattern is recorded in the powder mixture after a single treatment with an electron beam with a current of 5 mA. During the analysis, a comparison with the peaks of cubic perovskite $CaTiO_3$ (PDF#43-0226) and $SrTiO_3$ (PDF#35-0734) was used. The calculated value of the lattice parameter a is 3.915 Å, indicating that that the larger Ba, Pb, and La atoms occupied the A-position of perovskite, which led to an expansion of the lattice, which is typical for the high-entropy phase. After repeated electronic processing (upper diffractogram), peak splitting is observed, which, according to [22], is explained by oxygen deficiency due to a partial decrease in Ti^{4+} to Ti^{3+}.

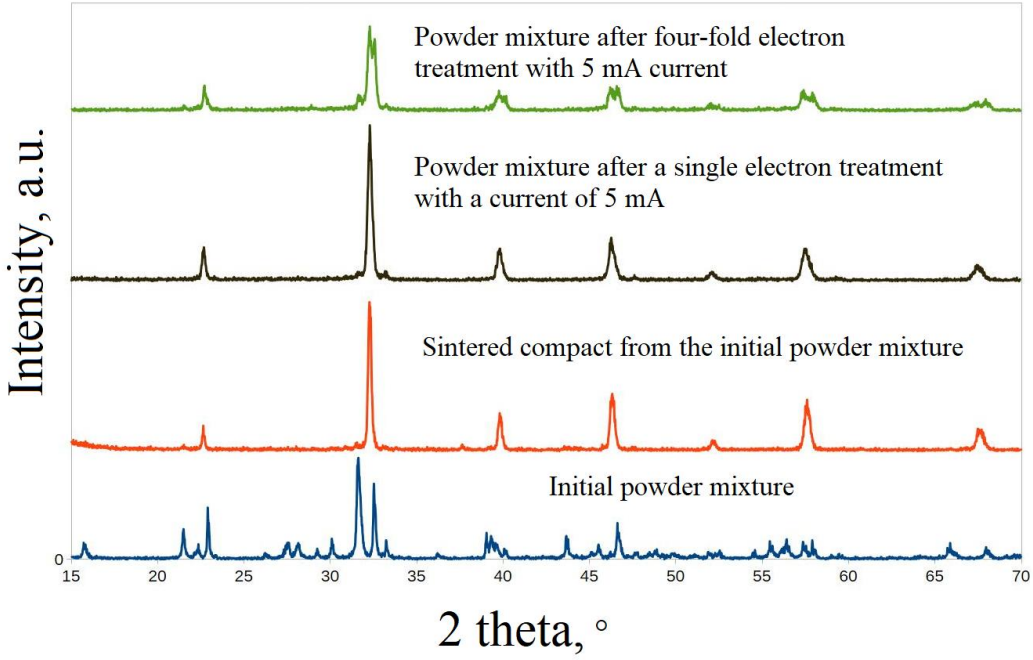

Figure 6. XRD patterns of the initial powder mixture, the compact sintered from it, and the initial powder after single and quadruple electron beam treatment. Electron energy: 1.4 MeV; beam current: 5 mA; cuvette movement speed under the beam: 1 cm/s

Thus, the presented experimental data indicate that preliminary short-term electron beam treatment of the powder mixture with the composition $4CaTiO_3 + 4SrTiO_3 + 4BaTiO_3 + 4PbTiO_3 + 2La_2O_3 + 4TiO_2$ initiates the synthesis of ceramics with the composition $(Ca_{0.2}Sr_{0.2}Ba_{0.2}Pb_{0.2}La_{0.2})TiO_3$ within the bulk of the mixture. With an increase in the number of irradiation/grinding cycles, the yield of the synthesized product increases, and the powder particles obtained after multiple treatments exhibit a ceramic nature. The results of dilatometry are presented in Figures 6–8.

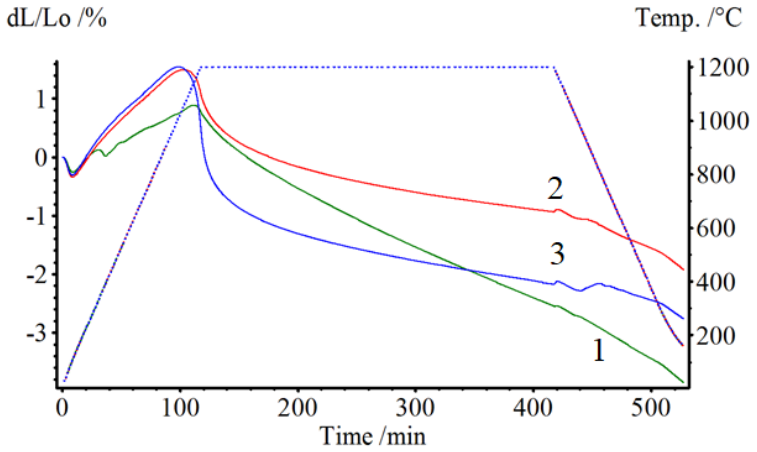

Figure 6. Dilatometric analysis of compacts for the sintering of $(Ca_{0.2}Sr_{0.2}Ba_{0.2}Pb_{0.2}La_{0.2})TiO_3$ ceramics from a powder mixture: (*1*) before treatment, (*2*) after a single treatment with a high-power electron beam, and (*3*) after five treatments with intermediate milling. Electron energy: 1.4 MeV; beam current: 4 mA; cuvette movement speed under the beam: 1 cm/s

The dilatograms (shrinkage curves) in Figure 6 show that the compact made from the initial powder mixture, when heated from 300 to 400 °C, exhibits a region of compaction followed by expansion, despite an overall tendency toward shrinkage. This behavior can be attributed to moisture release processes, as shown in Figure 2 (the position of the endothermic peak on the DSC curve). During isothermal holding, the compact steadily compacts, and during the cooling stage, at a temperature of approximately 300 °C, a region of barely noticeable abrupt change in linear dimension is observed, which is usually associated with a phase transition in the material under study.

The dilatograms for compacts (Fig. 6, curves *2* and *3*) obtained from powder mixtures subjected to electron beam treatment do not exhibit any changes in linear dimensions during the heating stage, unlike those for the compact from the initial powder mixture. The increase in linear dimensions during heating is more pronounced. The shrinkage curves themselves have a shape characteristic of ceramic sintering: the compact expands during heating, and when the temperature reaches 900–1000 °C, compaction processes begin to prevail over linear expansion, with the maximum shrinkage rate observed upon reaching the sintering temperature. As the heating time increases, the shrinkage rate decreases, indicating the formation of the ceramic structure of the sample. Increasing the electron beam current to 5 mA during the initial processing further enhances compaction (Fig. 7, curve *2*).

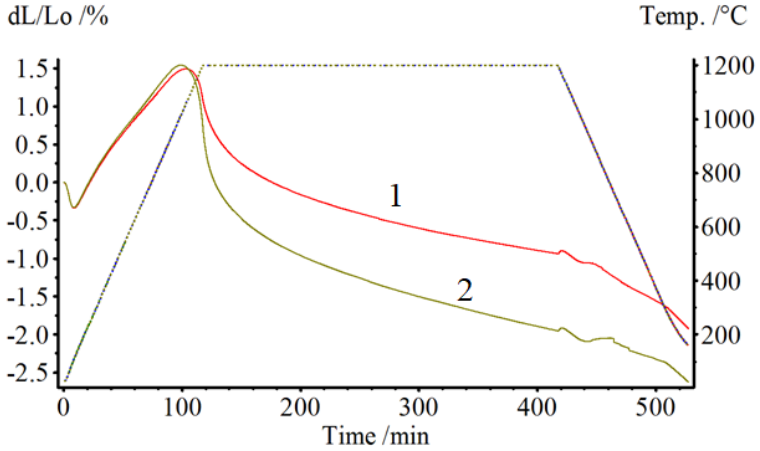

Figure 7. Dilatometric analysis of compacts for the sintering of $(Ca_{0.2}Sr_{0.2}Ba_{0.2}Pb_{0.2}La_{0.2})TiO_3$ ceramics from a powder mixture after a single treatment with a high-power electron beam (E = 1.4 MeV; scan speed: 1 cm/s): Curve 1 — beam current 4 mA; Curve 2 — beam current 5 mA

The trends observed for the effect of electron beam current on the shrinkage of powder compacts after a single electron beam treatment are preserved for multiple irradiation/grinding cycles (Fig. 8).

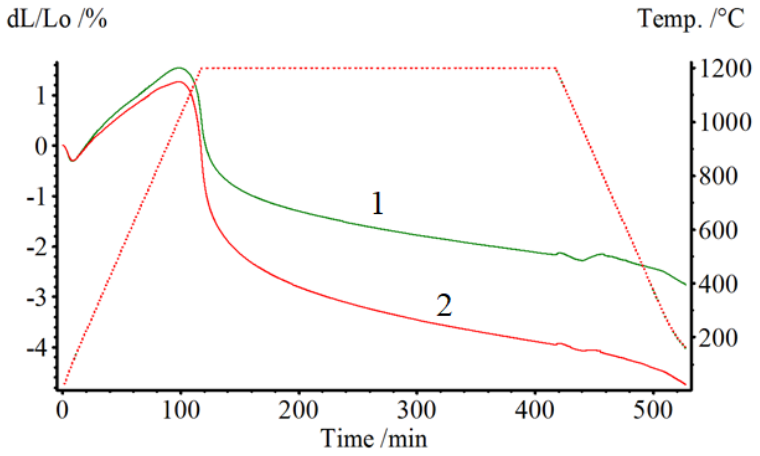

Figure 8. Dilatometric analysis of compacts for the sintering of $(Ca_{0.2}Sr_{0.2}Ba_{0.2}Pb_{0.2}La_{0.2})TiO_3$ ceramics from a powder mixture after multiple treatments with a high-power electron beam (E = 1.4 MeV; scan speed: 1 cm/s): Curve 1 — 5 treatment cycles at a beam current of 4 mA; Curve 2 — 4 treatment cycles at a beam current of 5 mA

Figure 8 shows that the shrinkage of the compacts increases with repeated electron beam processing. This effect is most pronounced at an electron beam current of 5 mA. Moreover, the change in linear dimension during the cooling stage is minimal in this case, which can be explained by the formation of a stable, high-entropy state in the sintered ceramics. These observed shrinkage patterns are confirmed by density measurements of the sintered ceramic samples, presented in Table 1.

Table 1

Measurement results for the density, porosity, and hardness of ceramic samples of $(Ca_{0.2}Sr_{0.2}Ba_{0.2}Pb_{0.2}La_{0.2})TiO_3$. Thermal sintering: 1200 °C, 5 hours

Compact type	Density, g/cm^3	Open porosity, %	Hardness, GPa
The compacts were fabricated from the as-prepared powder mixture	3.27±0.32	41±6	2.75±0.21
From the powder after a single electron beam treatment at a beam current of 4 mA	4.40±0.28	20±4	3.2±0.32
From the powder after four cycles of electron beam treatment at a beam current of 5 mA	5.04±0.36	8±1	6.11±0.33

The data in Table 1 indicate an increase in the density and hardness of the sintered ceramics after electron beam treatment of the initial powder mixture, accompanied by a corresponding decrease in open porosity. The low density and high porosity of the ceramics sintered from the initial powder mixture, which was not subjected to electron beam treatment, indicate that the sintering time was insufficient. The change in the compact shrinkage kinetics after electron beam treatment can be explained based on the X-ray diffraction data presented in Figure 6. The diffraction pattern for the ceramics sintered from the initial powder mixture indicates incomplete formation of the high-entropy phase and contains a small number of extraneous peaks. Their presence is evidence of incomplete synthesis during sintering. With an increasing number of electron beam treatments, the content of the high-entropy phase in the powder mixture increases. Compacts formed from powders with a high content of the high-entropy phase are compacted more efficiently, since the synthesis processes that hinder ceramic compaction are partially or completely completed under the influence of the electron beam. Powder subjected to multiple electron beam treatments is characterized by a diffraction pattern that most closely matches the samples obtained in [22]. Thus, as the number of irradiation treatments increased, the sintering behavior of compacts made from treated powders became similar to that of ceramics where particle compaction is the primary mechanism. Moreover, thermal energy is not wasted on material synthesis. Consequently, preliminary electron beam treatment of the powder mixture allows for a significant reduction in the sintering time of ceramic products. Electron beam treatment significantly accelerates synthesis and, accordingly, reduces the time and cost of ceramic production.

Conclusion

Using the example of high-entropy ceramics $(Ca_{0.2}Sr_{0.2}Ba_{0.2}Pb_{0.2}La_{0.2})TiO_3$, a promising material for solar energy applications, we studied the effect of treatment in air with high-energy electrons (1.4 MeV) on the synthesis and sintering of this ceramic. It was found that, starting from the first cycle of short-term electron beam treatment, the radiation processing is accompanied by the formation of the oxides constituting the high-entropy phase $(Ca_{0.2}Sr_{0.2}Ba_{0.2}Pb_{0.2}La_{0.2})TiO_3$ in the powder mixture. With an increasing number of treatment/grinding cycles, the phase composition of the mixture increasingly corresponds to that of the target $(Ca_{0.2}Sr_{0.2}Ba_{0.2}Pb_{0.2}La_{0.2})TiO_3$ ceramics. The effectiveness of the treatment increases with the number of cycles, which accelerates the sintering process and leads to an increase in the ceramic's density and mechanical strength.

Acknowledgment

This work was supported by the Russian Science Foundation [grant no. 23-79-00014].

References

1 Wang, R., Zhang, J., Cao, Y., ... Liu, S., & Feng, J. (2026). Reconstruction of the surface for efficient 3D/quasi-2D heterostructured inverted perovskite solar cells. *Advanced Functional Materials*, *36*(15), e17633. DOI: 10.1002/adfm.202517633.

2 Gralik, G., Thomsen, A.E., Moraes, C.A., Raupp-Pereira, F., & Hotza, D. (2014). Processing and characterization of $CaTiO_3$ perovskite ceramics. *Processing and Application of Ceramics, 8*(2), 87–92. DOI: 10.2298/PAC1402053G.

3 Wan, Z., Wei, R., Zhao, H., ... Luo, J., & Jia, C. (2026). Thermal management technologies for improving the thermal stability of perovskite solar cells. *NanoMicroLetters, 18*(1), 207. DOI: 10.1007/s40820-025-02047-x.

4 Reddy, D.J., & Lazarus, I.J. (2024). Fabrication and characterization of methylammonium lead iodide-based perovskite solar cells under ambient conditions. *Indonesian Journal of Electrical Engineering and Computer Science, 34*(3), 1410–1419. DOI: 10.11591/ijeecs.v34.i3.pp1410-1419.

5 Salifu, S., & Olubambi, P.A. (2025). High entropy alloy reinforced lightweight metal matrix composites: A review of the fundamentals, fabrication, properties, and prospects. *Materials Today Sustainability,* 32, 101216. DOI: 10.1016/j.mtsust.2025.101216.

6 Zhang, R.-Z., & Reece, M.J. (2019). Review of high entropy ceramics: design, synthesis, structure and properties. *Journal of Materials Chemistry A, 7*(39), 22148–22162. DOI: 10.1039/c9ta05698j.

7 Wang, M., Liu, R., Qi, K., ... Li, Z., & Sun, C. (2025). Research progress of high-temperature resistant aerogel thermal insulation materials for aerospace applications. *Journal of Ceramics, 46*(4), 672–688. DOI: 10.13957/j.cnki.tcxb.2025.04.003.

8 Sharma, Y., Mazza, A.R., Musico, B.L., ... Keppens, V., & Ward, T.Z. (2021). Magnetic texture in insulating single crystal high entropy oxide spinel films. *ACS Applied Materials and Interfaces, 13*(15), 17971–17977. DOI: 10.1021/acsami.1c01344.

9 Sun, L., Wang, J., Hu, Z., Chen, W., & Sun, C. (2026). Advances in high-entropy oxides for reversible protonic ceramic cells applications. *Applied Energy, 411*, 127595. DOI: 10.1016/j.apenergy.2026.127595.

10 Wang, B., Hao, Y., Xu, Y., Chen, X., & Zhang, K. (2026). Investigation on the microstructure, optical, and mechanical properties of multi-component sesquioxide transparent ceramics. *Journal of the European Ceramic Society, 46*(5), 118017. DOI: 10.1016/j.jeurceramsoc.2025.118017.

11 Jiang, S., Hu, T., Gild, J., ... Vecchio, K., & Luo, J. (2018). A new class of high-entropy perovskite oxides. *Scripta Materialia, 142*, 116–120. DOI: 10.1016/j.scriptamat.2017.08.040.

12 Vinnik, D.A., Trofimov, E.A., Zhivulin, V.E., ... Trukhanov, S.V., & Podgornov, F.V. (2020). High entropy oxide phases with perovskite structure. *Nanomaterials, 10*(2), 268. DOI: 10.3390/nano10020268.

13 Li, S., Li, J., Zhou, C., ... Yan, J., & Qi, X. (2022). Research on the dielectric energy storage characteristics of the $[(Bi_{0.5}Na_{0.5})_{0.2}Ba_{0.2}Sr_{0.2}Ca_{0.2}Mg_{0.2}]TiO_3$ equal ratio high-entropy ceramics. *Journal of Materials Science Materials in Electronics, 33*(30), 23792–23805. DOI: 10.1007/s10854-022-09137-1.

14 Il'in, A.P., Root, L.O., & Mostovshchikov, A.V. (2012). The rise of energy accumulated in metal nanopowders. *Technical Physics, 57*(8), 1178–1180. DOI: 10.1134/S1063784212080129.

15 Mostovshchikov, A.V., Ilyin, A.P., & Egorov, I.S. (2024). Effect of electron beam irradiation on the thermal properties of the aluminum nanopowder. *Radiation Physics and Chemistry, 153*, 156–158. DOI: 10.1016/j.radphyschem.2018.09.024.

16 Fadeev, S.N., Golkovski, M.G., Korchagin, A.I., ... Salimov, R.A., & Vaisman, A.F. (2000). Technological applications of BINP industrial electron accelerators with focused beam extracted into atmosphere. *Radiation Physics and Chemistry, 57*(3–6), 653–655. DOI: 10.1016/S0969-806X(99)00499-5.

17 Vorobev, D.S., Domarov, E.V., Golkovskii, M.G., ... Lavrukhin, A.V., & Nemytov, P.I. (2021). Accelerators of ELV series: current status and further development. *CERN Proceedings,* 111–113. DOI: 10.18429/JACoW-RuPAC2021-FRB02.

18 Ghyngazov, S.A., Surzhikov, A.P., Vasil'ev, I.P., Boltueva, V.A., & Vlasov, V.A. (2024). Synthesis of high-entropy ceramics $(Y_{0.2}Yb_{0.2}Lu_{0.2}Eu_{0.2}Er_{0.2})_3Al_5O_{12}$ by electron beam heating. *Ceramics International, 50*(22), 45037–45043. DOI: 10.1016/j.ceramint.2024.08.342.

19 Ghyngazov, S.A., Vasil'ev, I.P., Boltueva, V.A., & Vlasov, V.A. (2025). Electron beam synthesis of $CaZrTi_2O_7$ zirconolite ceramics. *Russian Physics Journal, 68*(9), 1454–1458. DOI: 10.1007/s11182-025-03580-3.

20 Ghyngazov, S.A., Boltueva, V.A., & Vasil'ev, I.P. (2024). Synthesis of oxide ceramics in a beam of fast electrons. *Bulletin of the University of Karaganda – Physics*, *29*(4(116)), 27–34. DOI: 10.31489/2024/PH4/27-34.

21 Golkovski, M.G., Denisov, I.P., Ghyngazov, S.A., Vasil'ev, I.P., & Chakin, I.K. (2024). Efficiency of liquid-phase synthesis of ceramic materials under the influence of an electron beam with high penetrating power. *Bulletin of the University of Karaganda – Physics*, *29*(4(116)), 35–45. DOI: 10.31489/2024PH4/35-45.

22 Zheng, Y., Zou, M., Zhang, W., Yi, D., Lan, J., Nan, C.-W., & Lin, Y.-H. (2021). Electrical and thermal transport behaviours of high-entropy perovskite thermoelectric oxides. *Journal of Advanced Ceramics, 10*(2), 377–384. DOI: 10.1007/s40145-021-0462-5.

С.А. Гынгазов, И.П. Васильев, В.А. Болтуева,
С. Бобуёк, И.К. Чакин, В.П. Кривобоков

Электронды өңдеудің бастапқы реагенттер ұнтақ қоспасының жоғары энтропиялы керамиканың $(Ca_{0.2}Sr_{0.2}Ba_{0.2}Pb_{0.2}La_{0.2})TiO_3$ күйдірілуіне әсері

Термоэлектрлік материалдардың дамуы жоғары энтропиялық материалдардың жаңа класының пайда болуына байланысты белсенді түрде жүргізілуде. Оларды өндіру процестері қатты фазалық синтезге дейін азаяды және реагенттердің ұнтақ қоспаларын механикалық араластырудың ұзақ циклдерін, жоғары температурада термиялық өңдеуді, осы операцияларды бірнеше рет қайталауды қамтиды. Жұмыста электронды-сәулелік өңдеуді қолдану арқылы термоэлектрлік қосымшалар үшін жоғары энтропинді керамика жасау процесін жеделдету мәселелері туралы айтылған. Жоғары энтропиялық перовскит керамикасын $(Ca_{0.2}Sr_{0.2}Ba_{0.2}Pb_{0.2}La_{0.2})TiO_3$ алу мысалында бастапқы реагенттердің ұнтақ қоспасын ауада жоғары энергиялы электронды сәулемен (E = 1,4 МэВ) циклдік өңдеудің керамиканың күйдіру (спекание) процесіне әсері зерттелді. Электронды сәуле тогы 4 мА (5 өңдеу циклі) және 5 мА-дан (4 өңдеу циклі) құрады. Әрбір сәулелендіру кезеңінен кейін ұнтақ механикалық түрде ұнтақталды. Электронды сәуле мен өңдеу күйдіру/тығыздау кинетикасын күшейтеді. Өңдеудің тиімділігі циклдар санымен артады, бұл керамиканың тығыздалу процесін жеделдетеді. Нәтижесінде керамиканың тығыздығы мен механикалық беріктігі жоғарылайды. Бұл жақсартулар электронды сәулемен өңдеу нәтижесінде ұнтақ қоспасында жоғары энтропиялық фаза $(Ca_{0.2}Sr_{0.2}Ba_{0.2}Pb_{0.2}La_{0.2})TiO_3$ түзілуімен байланысты.

Кілт сөздер: жоғары энтропиялық керамика, перовскиттер, синтез, электронды сәулелер, күйдіру

С.А. Гынгазов, И.П. Васильев, В.А. Болтуева,
С. Бобуёк, И.К. Чакин, В.П. Кривобоков

Влияние электронной обработки порошковой смеси исходных реагентов на спекание высокоэнтропийной керамики $(Ca_{0.2}Sr_{0.2}Ba_{0.2}Pb_{0.2}La_{0.2})TiO_3$

Развитие термоэлектрических материалов идет активно в связи с появлением нового класса высокоэнтропийных материалов. Процессы их производства сводятся к твердофазному синтезу и включают длительные циклы механического перемешивания порошковых смесей реагентов, термической обработки при высокой температуре, повторение данных операций несколько раз. В работе решаются вопросы ускорения процесса изготовления высокоэнтропийной керамики для термоэлектрических приложений за счет применения электронно-лучевой обработки. Изучено влияние циклической обработки порошковой смеси исходных реагентов на воздухе с помощью пучка высокоэнергетических электронов (E = 1,4 МэВ) на процесс спекания компактов на примере высокоэнтропийной перовскитной керамики $(Ca_{0.2}Sr_{0.2}Ba_{0.2}Pb_{0.2}La_{0.2})TiO_3$. Ток электронного пучка составлял 4 мА (5 циклов обработки) и 5 мА (4 цикла обработки), при этом после каждого этапа облучения проводилось механическое измельчение порошка. Было установлено, что обработка электронным пучком ускоряет кинетику уплотнения/спекания. Эффективность обработки возрастает с увеличением числа циклов. Это приводит к ускорению процесса спекания, увеличению плотности и механической прочности керамики. Данные улучшения объясняются формированием в порошковой смеси высокоэнтропийной фазы $(Ca_{0.2}Sr_{0.2}Ba_{0.2}Pb_{0.2}La_{0.2})TiO_3$ в результате обработки электронным пучком.

Ключевые слова: высокоэнтропийная керамика, перовскиты, синтез, электронные пучки, спекание

Information about the authors

Ghyngazov, Sergei (*corresponding author*) — Doctor of Engineering Sciences, Leading Researcher, National Research Tomsk Polytechnic University, Tomsk, Russia; e-mail: ghyngazov@tpu.ru, ORCID ID: https://orcid.org/0000-0002-2524-9238

Vasil'ev, Ivan — PhD in Engineering Sciences, Researcher, National Research Tomsk Polytechnic University, Tomsk, Russia; e-mail: zarkvon@tpu.ru, ORCID ID: https://orcid.org/0000-0002-4077-7012

Boltueva, Valeria — PhD in Engineering Sciences, Researcher, National Research Tomsk Polytechnic University, Tomsk, Russia; e-mail: kostenkova@tpu.ru, ORCID ID: https://orcid.org/0000-0001-8128-9042

Bobuyok, Sergei — Engineer, National Research Tomsk Polytechnic University, Tomsk, Russia; e-mail: bobuyok@tpu.ru, ORCID ID: https://orcid.org/0000-0002-9838-1934

Chakin, Ivan — Engineer, Budker Institute of Nuclear Physics SB RAS, Novosibirsk, Russia; e-mail: chak_in2003@bk.ru, ORCID ID: https://orcid.org/0000-0003-0529-2017

Krivobokov, Valery — Professor, Doctor of Physical and Mathematical Sciences, Head of Department, National Research Tomsk Polytechnic University, Tomsk, Russia; e-mail: krivobokov@tpu.ru, ORCID ID: https://orcid.org/0000-0003-0569-3291

Article

UDC 544.6

https://doi.org/10.31489/2026PH2/49-57

Received: 28.01.2026
Accepted: 25.03.2026

D.A. Zakari[1]✉, G.A. Audu[2], A.A. Aliyu[3], I.O. Mustapha[4], K.M. Omatola[5]

[1,2,3,5]Prince Abubakar Audu University, PMB 1008, Anyigba, Kogi State, Nigeria;
[4]Interdisciplinary Research Center for Membranes and Water Security,
King Fahd University of Petroleum and Minerals, Dhahran 31261, Saudi Arabia

Electrochemical Oxidation of Methyl Orange as a Model Azo Dye Pollutant: Comparative Electrode Performance, EIS Mechanistic Analysis, and Techno-Economic Assessment

This study investigates the electrochemical oxidation (EO) of methyl orange (MO) as a model azo dye pollutant representative of textile and industrial effluents, using boron-doped diamond (BDD) and dimensionally stable anode (DSA) electrodes under systematically optimized conditions. Model solutions were prepared in ultrapure water with 0.1 M Na_2SO_4 as the supporting electrolyte. Batch experiments were conducted in galvanostatic mode at 25 ± 1 °C with constant stirring (300 rpm), varying current densities (10–50 mA/cm²), pH values (2–10), and initial methyl orange concentrations (50–500 mg/L). BDD anodes achieved 94.3 ± 2.1 % pollutant removal within 120 min at optimal conditions (30 mA/cm², pH 3.0, 200 mg/L), significantly outperforming DSA (87.6 ± 3.3 %) and platinum (68.7 ± 4.5 %) electrodes. Electrochemical impedance spectroscopy (EIS) using a Randles R(C_{dl}(R_{ct}W)) equivalent circuit revealed a 73 % decrease in charge transfer resistance (R_{ct}: 385 Ω → 104 Ω) with increasing anodic potential (1.0–2.5 V vs. Ag/AgCl), confirming Butler–Volmer-controlled oxidation kinetics. The apparent rate constant k_{app} = 0.0315 ± 0.0018 min^{-1} for BDD was 1.68-fold greater than for platinum. Total organic carbon (TOC) analysis confirmed near-complete mineralization (96.8 ± 1.5 % TOC reduction) with BDD. Specific energy consumption was minimized to 8.2 kWh/m^3, indicating the potential competitiveness of this approach for treating dye-containing effluents. At Nigerian electricity tariffs (₦45/kWh), estimated treatment cost is ₦369/m^3, suggesting feasibility for industrial application in developing economies, pending validation with real effluent matrices.

Keywords: electrochemical oxidation, boron-doped diamond, azo dye degradation, methyl orange, dimensionally stable anode, electrochemical impedance spectroscopy, mineralization, model pollutant, charge transfer resistance, hydroxyl radicals, pseudo-first-order kinetics, techno-economic assessment

✉*Corresponding author*: Zakari, David, david.z@ksu.edu.ng

Introduction

Synthetic azo dyes in industrial effluents represent a growing environmental and public health challenge, particularly in rapidly industrializing nations where textile, pharmaceutical, and food-processing industries discharge large volumes of dye-laden wastewater [1]. Among these, methyl orange (MO) is widely used as a model azo dye pollutant in electrochemical treatment research owing to its representative chromophoric azo group (–N=N–) and strong resistance to aerobic biodegradation, allowing quantitative spectrophotometric monitoring and systematic mechanistic study [2, 3].

Conventional treatment approaches present significant limitations for azo dye-containing effluents. The central challenge is biochemical: aerobic microbial metabolism cannot efficiently cleave the azo bond (–N=N–) because the electron-withdrawing sulphonate and nitro substituents on the aromatic rings create a highly oxidised chromophore that resists oxidative catabolism by most bacterial enzyme systems [3]. Under aerobic conditions, conventional activated sludge processes therefore achieve only 30–50 % colour removal for recalcitrant azo structures, and the aromatic amine intermediates that do form under anaerobic reductive cleavage are frequently more toxic and carcinogenic than the parent dye [3, 4]. Combined anaerobic–aerobic biological systems improve mineralization somewhat but require long hydraulic retention times, large reactor footprints, and precise control of redox conditions, making them difficult to retrofit into existing industrial infrastructure [4]. Chemical coagulation–flocculation generates large sludge volumes requiring costly disposal without achieving true mineralization. These fundamental limitations of microbial metabolism and

physicochemical methods underline the need for destructive, non-sludge-generating advanced oxidation technologies capable of complete mineralization of the aromatic dye scaffold to CO_2 and H_2O.

Electrochemical oxidation (EO) mineralizes organics through direct anodic electron transfer, governed by Faraday's law and Butler–Volmer kinetics, without external chemical reagents [5]. The electrode material critically determines treatment efficacy. Boron-doped diamond (BDD) anodes exhibit an exceptionally wide electrochemical window (~3.2 V in aqueous media) and high oxygen-evolution overpotential (~1.8–2.3 V vs. SHE), enabling generation of surface hydroxyl radicals (•OH, $E°$ = 2.80 V vs. SHE) at densities sufficient for complete mineralization of refractory compounds [6–9]. Dimensionally stable anodes (DSA, IrO_2–RuO_2/Ti) offer lower capital cost but their reduced overpotential limits •OH yield [4].

Despite growing laboratory-scale EO literature, systematic multi-parameter optimization and quantitative EIS-based mechanistic characterization remain fragmented. Techno-economic assessments for sub-Saharan African industrial contexts are also largely absent. Nigeria's textile, pharmaceutical, and food-processing industries collectively discharge an estimated 150 million m³ of inadequately treated wastewater annually, exerting severe pressure on receiving water bodies [10]. Electrochemical methods are particularly attractive for this setting as they require only electrical energy, generate no chemical sludge, and enable modular deployment [11].

The present study therefore aimed to: (1) compare BDD and DSA electrode performance against platinum using MO model solutions under controlled laboratory conditions; (2) optimize current density, solution pH, and initial dye concentration; (3) elucidate electrode kinetics using EIS and Randles-type equivalent circuit analysis; (4) quantify mineralization efficiency via TOC analysis; and (5) evaluate energy consumption and estimated treatment cost to assess prospective industrial feasibility. The scientific novelty lies in the integrated mechanistic–economic analysis linking EIS-derived kinetic parameters to treatment efficiency metrics, with the results establishing a quantitative performance baseline for future validation with real textile and industrial effluents in the Nigerian and sub-Saharan African context.

Materials and Methods

Electrochemical apparatus and electrode materials. All experiments were conducted in a thermostated, undivided three-electrode batch cell (borosilicate glass, 100 mL working volume; cylindrical geometry, 50 mm i.d.) maintained at 25 ± 1 °C by a circulating water bath (Julabo F12). Mixing was provided by a magnetic stir bar at 300 rpm (IKA RCT Basic) to ensure uniform mass transport. The inter-electrode gap between anode and cathode was fixed at 15 mm throughout all experiments. Three anode materials were evaluated: (i) boron-doped diamond thin film on silicon substrate (5 mm × 5 mm × 1 mm, B/C atomic ratio ≈ 1000 ppm, Element Six, UK); (ii) IrO_2–RuO_2/Ti dimensionally stable anode (Premetek Inc., USA); and (iii) platinum foil (99.99 % purity, Alfa Aesar). A platinum gauze sheet (geometric area 10 mm × 10 mm, 52 mesh, Alfa Aesar) served as the cathode; its larger surface area relative to the anode ensured that the anodic reaction remained rate-determining. An Ag/AgCl electrode (3 M KCl, +0.210 V vs. SHE, CH Instruments) served as the reference electrode and was positioned 5 mm from the anode surface via a Luggin capillary to minimize ohmic drop. All galvanostatic experiments were controlled by a PGSTAT204N potentiostat (Metrohm Autolab, Netherlands) operating in current-controlled (CC) mode; the applied current was held constant throughout each run and the corresponding cell voltage was logged continuously. The FRA32M frequency-response analysis module was used for EIS measurements. Impedance data were fitted to the Randles $R(C_{dl}(R_{ct}W))$ equivalent circuit using NOVA 2.1 software ($\chi^2 < 10^{-3}$).

Chemical reagents and solutions. Methyl orange (C.I. 13025, M_w = 327.33 g/mol; λ_{max} = 464 nm; Sigma-Aldrich, ≥98 %) served as the model azo dye pollutant. Stock solutions (1000 mg/L) were prepared gravimetrically in ultrapure water (>18 MΩ·cm, Milli-Q A10). Sodium sulfate (0.1 M Na_2SO_4; Sigma-Aldrich, ≥99 %) served as supporting electrolyte. Solution pH was adjusted to target values (2.0, 3.0, 5.0, 7.0, 10.0) using 1 M HCl or NaOH and monitored with a calibrated pH meter (Mettler-Toledo FiveEasy).

Experimental protocol. Current density was varied at 10, 20, 30, 40, and 50 mA/cm² (pH 3.0, $[MO]_0$ = 200 mg/L). pH was varied at 2.0, 3.0, 5.0, 7.0, and 10.0 (30 mA/cm², $[MO]_0$ = 200 mg/L). Initial concentration was studied over 50–500 mg/L (30 mA/cm², pH 3.0). Each condition was replicated in triplicate (n = 3) on separate days. Aliquots (1 mL) were withdrawn at 0, 15, 30, 45, 60, 90, and 120 min, filtered through 0.45 μm PTFE syringe filters, and analyzed within 30 min.

Analytical methods. Dye concentration was quantified by UV-Visible spectroscopy (Lambda 365, PerkinElmer) at λ_{max} = 464 nm using five-point external calibration curves ($R^2 > 0.998$, 2–50 mg/L). Total organic carbon was measured in NPOC mode (acidification and CO_2 sparging to remove inorganic carbon)

using a TOC-V CPH analyzer (Shimadzu; detection limit: 2 μg/L). EIS measurements were performed over a frequency range of 10 kHz to 0.01 Hz (60 logarithmically spaced points per decade) at each of four applied potentials (1.0, 1.5, 2.0, and 2.5 V vs. Ag/AgCl), using a 10 mV RMS sinusoidal AC perturbation superimposed on the DC bias. Measurements were performed under open-circuit steady state, confirmed by monitoring the potential drift to below 0.5 mV min^{-1} before acquisition. The linearity and causality of each spectrum were verified by Kramers–Kronig compliance (residuals <1 % across the full frequency range) using the KK-test routine in NOVA 2.1 prior to equivalent circuit fitting. Spectra were fitted to the Randles $R(C_{dl}(R_{ct}W))$ circuit using a complex non-linear least squares (CNLS) algorithm; goodness-of-fit was assessed by the chi-squared criterion ($\chi^2 < 5 \times 10^{-4}$) and visual inspection of Nyquist and Bode representations.

Removal efficiency (RE, %) was calculated as:

$$RE\ (\%) = [(C_0 - C_t)/C_0] \times 100,$$

where C_0 and C_t are concentrations (mg/L) at time 0 and t (min), respectively. Apparent rate constants (k_{app}, min^{-1}) were determined from $-\ln(C_t/C_0)$ vs. t regression. Specific energy consumption E_{sp} (kWh/m³) for 90 % removal was calculated as $E_{sp} = (U \times I \times t_{90})/V$, where U is cell voltage (V), I is applied current (A), t_{90} is the time for 90 % removal (h), and V is solution volume (m³).

Results and Discussion

3.1 Comparative performance of electrode materials. Figure 1 shows time-resolved degradation profiles for BDD, DSA, and platinum anodes at 30 mA/cm², pH 3.0, and $[MO]_0$ = 200 mg/L. BDD electrodes achieved 94.3 ± 2.1 % removal within 120 min, significantly outperforming DSA (87.6 ± 3.3 %) and platinum (68.7 ± 4.5 %), with statistically significant pairwise differences (one-way ANOVA, $F(2,6) = 38.4$, $p < 0.001$; Tukey HSD). All systems followed pseudo-first-order kinetics ($R^2 > 0.95$), with apparent rate constants k_{app} of 0.0315 ± 0.0018 min^{-1} (BDD), 0.0271 ± 0.0025 min^{-1} (DSA), and 0.0187 ± 0.0031 min^{-1} (Pt). The 1.68-fold acceleration with BDD relative to Pt reflects the exceptional •OH generation capacity of diamond surfaces at high anodic overpotentials [6, 12]. These k_{app} values fall within the 0.028–0.038 min^{-1} range reported for BDD-based degradation of comparable azo dyes [13–16]. Electrochemical performance comparison of electrode materials is presented in Table 1.

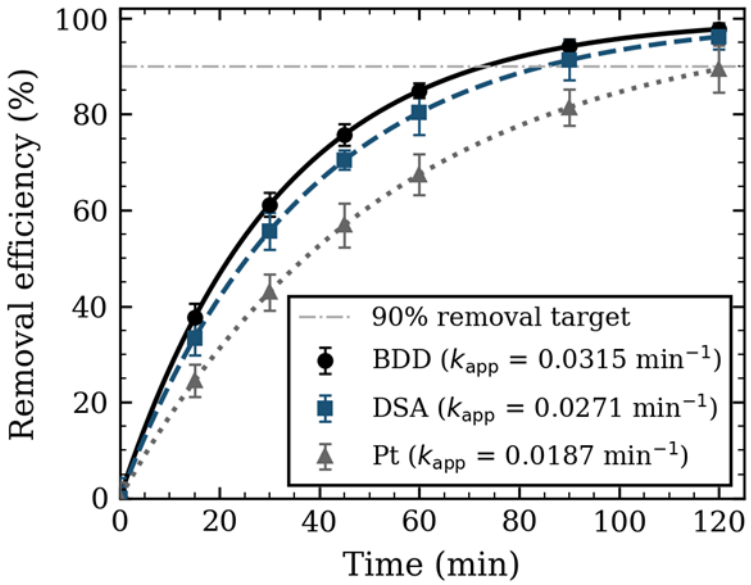

Figure 1. Time-resolved degradation of methyl orange using BDD, DSA, and platinum electrodes. Conditions: 30 mA/cm², pH 3.0, $[MO]_0$ = 200 mg/L, 0.1 M Na_2SO_4, T = 25 ± 1 °C, 300 rpm, n = 3. Error bars represent ± standard deviation

Table 1

Electrochemical performance comparison of electrode materials

Electrode Material	RE (%)	k_{app} (min^{-1})	t_{90} (min)	TOC Reduction (%)	Energy Consumption (kWh/m^3)
BDD (5×5 mm)	94.3 ± 2.1	0.0315 ± 0.0018	73	96.8 ± 1.5	8.2
DSA (IrO_2–RuO_2/Ti)	87.6 ± 3.3	0.0271 ± 0.0025	85	89.2 ± 2.8	9.1
Platinum foil	68.7 ± 4.5	0.0187 ± 0.0031	123	72.4 ± 3.2	12.5

Note: Conditions: 30 mA/cm², pH 3.0, $[MO]_0$ = 200 mg/L, 0.1 M Na_2SO_4, 25 ± 1 °C, 300 rpm, n = 3. Values are mean ± SD. RE = removal efficiency; k_{app} = apparent first-order rate constant; t_{90} = time for 90 % removal; TOC = total organic carbon reduction at 120 min

3.2 Influence of current density. Figure 2 (panel B) shows that increasing current density from 10 to 30 mA/cm² enhanced MO removal from 76.2 ± 3.1 % to 94.3 ± 2.1 %, consistent with the linear relationship between Faradaic charge and •OH flux predicted by Faraday's law. Beyond 30 mA/cm², gains were marginal (96.1 ± 1.8 % at 50 mA/cm²), indicating the onset of mass-transport limitation confirmed by the Warburg element in EIS data (Section 3.4). Concurrently, specific energy consumption rose from 5.1 to 13.8 kWh/m³ across 10–50 mA/cm², establishing 30 mA/cm² as the economically optimal operating point. These trends are in agreement with Butler–Volmer predictions of exponential current–overpotential dependence [9, 12].

3.3 pH-dependent degradation behavior. Solution pH modulates treatment efficiency through three mechanisms: (1) protonation state of the dye molecule, affecting its adsorption at the anode surface; (2) stability of electrogenerated •OH, which is scavenged by OH^- at alkaline pH via $•OH + OH^- \rightarrow O•^- + H_2O$; and (3) competition from oxygen evolution at higher pH. Figure 2 (panel A) shows that maximum removal (94.3 ± 2.1 %) occurred at pH 3.0, declining to 88.6 ± 2.4 % (pH 5.0), 76.4 ± 3.0 % (pH 7.0), and 52.1 ± 4.1 % (pH 10.0). Below the pK_a of MO (~3.5), the neutral azo form adsorbs more readily at the positively charged BDD surface, increasing the rate of direct oxidation [17–19].

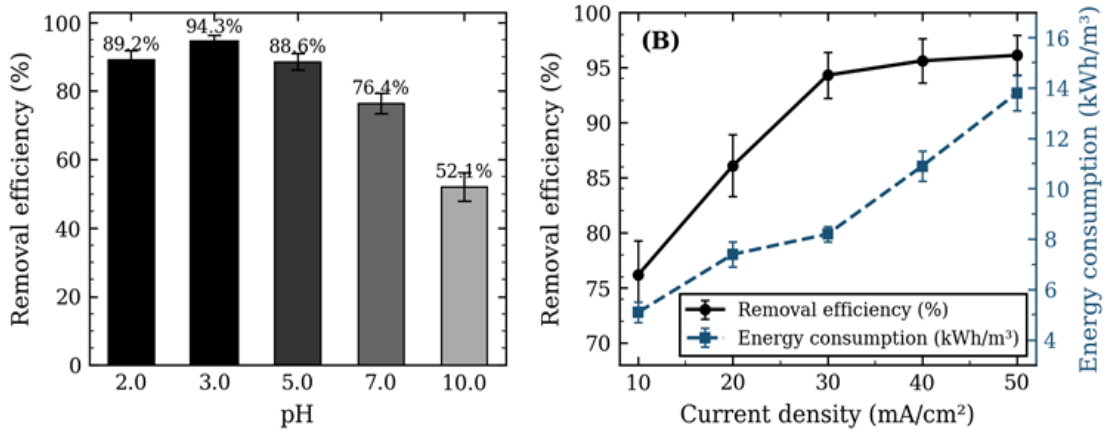

Figure 2. Effect of operating parameters on methyl orange removal using BDD electrode (n = 3, error bars = ± SD). *A* — Effect of pH (30 mA/cm², $[MO]_0$ = 200 mg/L). *B* — Effect of current density on removal efficiency and specific energy consumption (pH 3.0, $[MO]_0$ = 200 mg/L)

3.4 Electrochemical impedance spectroscopy analysis. Nyquist plots (Figure 3*A*) display the depressed semicircle topology characteristic of charge-transfer-controlled kinetics. The Randles $R(C_{dl}(R_{ct}W))$ circuit yielded excellent fits ($\chi^2 < 5\times10^{-4}$) in all cases. Charge transfer resistance R_{ct} decreased from 385 Ω at 1.0 V to 104 Ω at 2.5 V vs. Ag/AgCl (73 % reduction), following exponential decay (R^2 = 0.982) consistent with $R_{ct} \propto \exp(-\alpha F\eta/RT)$ where α is the transfer coefficient, F is Faraday's constant, η is overpotential, and T is temperature [20, 21]. Double-layer capacitance C_{dl} remained stable at 45–52 μF across the potential range, confirming no significant electrode fouling or passivation. The Warburg element became prominent at current densities ≥40 mA/cm², corroborating the mass-transport limitation identified in Section 3.2. Fitted EIS parameters are summarized in Table 2.

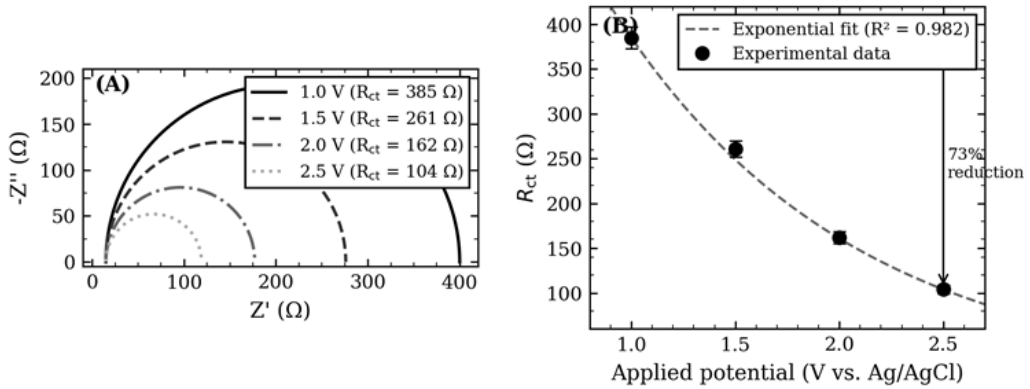

Figure 3. Electrochemical impedance spectroscopy results for BDD electrode at different applied potentials (pH 3.0, $[MO]_0$ = 200 mg/L, 0.1 M Na_2SO_4). *A* — Nyquist plots (symbols = measured data; lines = $R(C^{dM}(R^{ct}W))$ fits). *B* — Potential dependence of charge transfer resistance R^{ct} with exponential decay fit (R^2 = 0.982), showing 73 % reduction from 1.0 to 2.5 V vs. Ag/AgCl

Table 2

EIS-derived equivalent circuit parameters for BDD electrode as a function of applied potential

Potential (V vs. Ag/AgCl)	R_{ct} (Ω)	C_{dl} (μF)	χ^2
1.0	385 ± 12	45 ± 2	3.2×10^{-4}
1.5	261 ± 9	47 ± 2	2.8×10^{-4}
2.0	162 ± 7	49 ± 3	4.1×10^{-4}
2.5	104 ± 5	52 ± 3	4.7×10^{-4}
Note: Equivalent circuit $R(C_{dl}(R_{ct}W))$; pH 3.0, $[MO]_0$ = 200 mg/L, 0.1 M Na_2SO_4, 25 ± 1 °C. Values are mean ± SD (n = 3).			

3.5 Mineralization and energy efficiency. Figure 4 shows TOC reduction profiles and energy consumption data. BDD achieved 96.8 ± 1.5 % TOC reduction at 120 min, compared with 89.2 ± 2.8 % (DSA) and 72.4 ± 3.2 % (Pt). The high TOC removal with BDD confirms conversion of MO to CO_2 and H_2O without significant accumulation of persistent aromatic amine or quinone intermediates [22]. All TOC values were obtained in NPOC mode with acidification and sparging to preclude inorganic carbon interference. Specific energy consumption for 90 % removal was 8.2 kWh/m^3 (BDD), 9.1 kWh/m^3 (DSA), and 12.5 kWh/m^3 (Pt). These values are competitive with photocatalytic advanced oxidation processes (5–12 kWh/m^3) and ozonation (8–15 kWh/m^3) while offering substantially simpler operation and zero chemical sludge [19, 22].

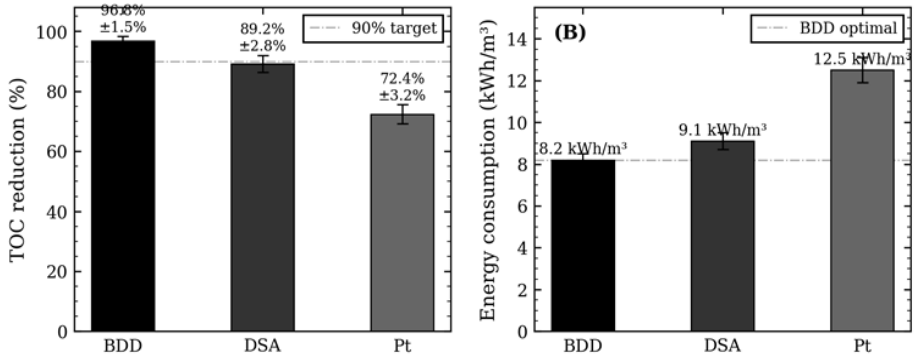

Figure 4. Mineralization and energy performance comparison (120 min treatment, 30 mA/cm^2, pH 3.0, n = 3; error bars = ± SD). *A* — Mineralization efficiency based on total organic carbon (TOC) reduction for BDD, DSA, and platinum electrodes; *B* — Specific energy consumption and estimated operating cost for 90 % pollutant removal (cost calculated at Nigerian electricity rate ₦45/kWh)

3.6 Electrochemical oxidation versus biological treatment: a mechanistic comparison. The superior performance of BDD-mediated electrochemical oxidation observed in this study is best understood in the context of the fundamental biochemical constraints that limit conventional biological treatment of azo dyes. In aerobic microbial metabolism, aromatic ring degradation proceeds via oxygenase-catalysed hydroxylation

followed by ring fission, a pathway that depends on the availability of nucleophilic reactive sites on the aromatic substrate [3, 23]. The azo chromophore of methyl orange, however, bears strongly electron-withdrawing sulphonate ($–SO_3Na$) and dimethylamino groups flanking the –N=N– linkage, rendering the molecule electron-deficient and sterically resistant to electrophilic attack by microbial mono- and dioxygenases [3, 4]. Consequently, aerobic activated sludge systems typically achieve only 20–40 % colour removal for sulphonated azo dyes, with negligible TOC reduction, as the intact aromatic scaffold persists through the biological reactor [23].

Under anaerobic conditions, azoreductase enzymes in facultative bacteria can reductively cleave the azo bond, producing colourless aromatic amines [3]. However, these amine products—including sulphanilic acid and dimethylaniline in the case of methyl orange—are frequently more acutely toxic and potentially carcinogenic than the parent dye, and themselves resist further microbial catabolism under aerobic conditions [4, 24]. Combined anaerobic–aerobic sequential biological systems have been investigated to couple reductive decolourization with aerobic mineralization of the amine intermediates, but typically achieve only 60–75 % TOC removal even under optimized conditions, and require hydraulic retention times of 24–72 h and careful redox management [23]. By contrast, BDD-mediated electrochemical oxidation in the present study achieved 96.8 ± 1.5 % TOC reduction within 120 min via non-selective hydroxyl radical attack (•OH, $E° = 2.80$ V vs. SHE), which oxidizes both the azo bond and the aromatic rings simultaneously, irrespective of electron density or substituent pattern [5, 6]. The •OH radical generated at the BDD surface reacts with the aromatic ring at diffusion-controlled rates ($k \approx 10^9$–10^{10} $M^{-1}s^{-1}$), bypassing the biochemical selectivity constraints that render microbial metabolism ineffective against recalcitrant azo structures [12, 22, 25].

These mechanistic distinctions have direct practical implications. The stable double-layer capacitance (C_{dl} = 45–52 μF) observed across the BDD electrode potential range confirms that electrode surface integrity was maintained throughout electrolysis, with no fouling by polymeric degradation products—a common operational failure mode in biological reactors treating high-strength dye effluents where biofilm inhibition by the dye itself disrupts microbial metabolism [4, 24]. Taken together, the EIS kinetic data, TOC mineralization results, and mechanistic contrast with biological treatment establish BDD electrochemical oxidation as a scientifically grounded alternative for treating azo dye effluents where conventional microbial methods are biochemically inadequate.

Industrial implementation and techno-economic assessment

For Nigerian and sub-Saharan African industrial contexts, electrochemical oxidation offers several practical advantages that justify the present laboratory-scale characterization as a precursor to scale-up: (i) no chemical consumables beyond electrical energy; (ii) modular scalability without process redesign; (iii) applicability across diverse pollutant classes; (iv) minimal sludge generation; and (v) potential integration with solar photovoltaic sources to reduce grid dependency. It must be noted that the energy and cost figures reported here derive from model MO solutions in a simple electrolyte matrix; real textile or pharmaceutical effluents contain competing organic loads, suspended solids, and chloride species that will alter energy demand and electrode service life.

Capital equipment cost for a 1,000 L/day electrochemical treatment unit is estimated at USD 18,000–25,000, compared with USD 45,000–65,000 for membrane bioreactor systems of equivalent throughput. At the Nigerian industrial electricity tariff of approximately ₦45/kWh, the energy-cost component for BDD-mediated treatment is ₦369/m^3 (~USD 0.81/m^3), which is economically competitive when lifecycle sludge disposal costs are included. Priority future work should address: (i) pilot-scale continuous-flow studies to validate batch-to-flow kinetic translation; (ii) complex matrix effects from co-contaminants; (iii) electrode lifetime and regeneration; and (iv) renewable energy integration.

Conclusion

This study systematically characterized the electrochemical oxidation of methyl orange as a well-defined model azo dye in ultrapure water with Na_2SO_4 supporting electrolyte, integrating kinetic optimization, EIS mechanistic analysis, and techno-economic evaluation. The results provide a rigorous quantitative baseline for evaluating electrode performance and process economics, with validation against real industrial effluents identified as a key priority for future work. The principal findings are:

1. BDD anodes achieved the highest pollutant removal (94.3 ± 2.1 %) and near-complete mineralization (96.8 ± 1.5 % TOC reduction) within 120 min under optimized conditions (30 mA/cm^2, pH 3.0, 200 mg/L), significantly outperforming DSA and platinum electrodes.

2. Pseudo-first-order kinetics were confirmed for all electrode types; the BDD apparent rate constant (k_{app} = 0.0315 ± 0.0018 min^{-1}) was 1.68-fold higher than for platinum, consistent with the superior •OH generation capacity of diamond surfaces.

3. EIS analysis using a Randles $R(C_{dl}(R_{ct}W))$ equivalent circuit revealed a 73 % reduction in R_{ct} (385 Ω → 104 Ω) over 1.0–2.5 V vs. Ag/AgCl, confirming Butler–Volmer-controlled charge-transfer kinetics. Stable C_{dl} (45–52 μF) demonstrated electrode surface integrity throughout electrolysis.

4. Optimal conditions (30 mA/cm^2, pH 3.0) were identified, yielding specific energy of 8.2 kWh/m^3 with BDD, competitive with photocatalytic and ozonation-based advanced oxidation processes.

5. At Nigerian electricity tariffs (₦45/kWh), an estimated treatment cost of ₦369/m^3 (~USD 0.81/m^3) indicates promising economic competitiveness for electrochemical oxidation in developing-economy industrial contexts, though cost projections for real effluents will depend on matrix composition, required pretreatment, and electrode lifetime under fouling conditions.

Acknowledgement

This research received no external funding. The authors thank the technical staff of Prince Abubakar Audu University, Anyigba, for analytical support.

References

1 Katheresan, V., Kansedo, J., & Lau, S.Y. (2018). Efficiency of various recent wastewater dye removal methods: A review. *Journal of Environmental Chemical Engineering, 6*(4), 4676–4697. https://doi.org/10.1016/j.jece.2018.06.060

2 Yusuf, M., Shabbir, M., & Mohammad, F. (2017). Natural colorants: Historical, processing and sustainable prospects. *Natural Products and Bioprospecting, 7*(1), 123–145. https://doi.org/10.1007/s13659-017-0119-9

3 Forgacs, E., Cserháti, T., & Oros, G. (2004). Removal of synthetic dyes from wastewaters: A review. *Environmental International, 30*(7), 953–971. https://doi.org/10.1016/j.envint.2004.02.001

4 Martínez-Huitle, C.A., & Brillas, E. (2009). Decontamination of wastewaters containing synthetic organic dyes by electrochemical methods: A general review. *Applied Catalysis B: Environmental, 87*(3-4), 105–145. https://doi.org/10.1016/j.apcatb.2008.09.017

5 Panizza, M., & Cerisola, G. (2005). Application of diamond electrodes to electrochemical processes. *Electrochimica Acta, 51*(2), 191–199. https://doi.org/10.1016/j.electacta.2005.04.023

6 Comninellis, C. (1994). Electrochemical oxidation of organic pollutants for wastewater treatment. *Electrochimica Acta, 39*(11-12), 1857–1862. https://doi.org/10.1016/0013-4686(94)85175-1

7 Li, X., Cui, Y., Feng, Y., Xie, Z., & Gu, J. (2005). Electrochemical oxidation of acid orange II in aqueous solution using a boron-doped diamond electrode. *Journal of Hazardous Materials, 117*(2-3), 215–222. https://doi.org/10.1016/j.jhazmat.2004.09.016

8 Martínez-Huitle, C.A., Rodrigo, M.A., Sirés, I., & Scialdone, O. (2015). Single and coupled electrochemical processes and reactors for the abatement of organic water pollutants: A critical review. *Chemical Reviews, 115*(24), 13362–13407. https://doi.org/10.1021/acs.chemrev.5b00361

9 Brosler, P., Girão, A.V., Silva, R.F., Tedim, J., & Oliveira, F.J. (2023). Electrochemical advanced oxidation processes using diamond technology: A critical review. *Environments, 10*, 15. https://doi.org/10.3390/environments10020015

10 Ochor, N.O., Onyeizu, R.U., Uchendu, U.I., & Ikpeazu, O.V. (2020). Assessment of industrial influent and effluent water quality at a bottling company in Aba, Abia State, Nigeria. *Nigerian Journal of Environmental Sciences and Technology, 4*(2), 253–259. https://doi.org/10.36263/nijest.2020.02.0200

11 Du, X., Xie, W., Long, X., Li, D., Huang, W., Zhang, I.Y., & Huang, R. (2025). Efficient removal of sulfamethoxazole in electro-oxidation system with boron-doped diamond anode and NaCl electrolyte: Degradation mechanisms. *Molecules, 30*(5), 1056. https://doi.org/10.3390/molecules30051056

12 Brillas, E., & Martínez-Huitle, C.A. (2015). Decontamination of wastewaters containing synthetic organic dyes by electrochemical methods: An updated review. *Applied Catalysis B: Environmental*, 166-167, 603–643. https://doi.org/10.1016/j.apcatb.2014.11.016

13 Serrano, K., Michaud, P.A., Comninellis, C., & Savall, A. (2002). Electrochemical preparation of peroxodisulfuric acid using boron-doped diamond thin film electrodes. *Electrochimica Acta*, *48*, 431–436. https://doi.org/10.1016/s0013-4686(02)00688-6

14 Fernandes, A., Pacheco, M.J., Ciríaco, L., & Lopes, A. (2012). Anodic oxidation of biologically treated leachate on a boron-doped diamond anode. *Journal of Hazardous Materials*, *199-200*, 82–87. https://doi.org/10.1016/j.jhazmat.2011.10.074

15 Aquino, J.M., Rocha-Filho, R.C., Ruotolo, L.A.M., Bocchi, N., & Biaggio, S.R. (2014). Electrochemical degradation of a real textile wastewater using β-PbO_2 and DSA® anodes. *Chemical Engineering Journal, 251*, 138–145. https://doi.org/10.1016/j.cej.2014.04.032

16 Brillas, E., Sirés, I., & Oturan, M.A. (2009). Electro-Fenton process and related electrochemical technologies based on Fenton's reaction chemistry. *Chemical Reviews, 109*(12), 6570–6631. https://doi.org/10.1021/cr900136g

17 Ganiyu, S.O., & Martínez-Huitle, C.A. (2020). The electrochemical advanced oxidation processes for pharmaceutical compounds removal from wastewater. *Reviews in Advanced Sciences and Engineering, 9*(1-2), 25–50. https://doi.org/10.1166/rase.2020.1356

18 Cho, K., Qu, Y., Kwon, D., Zhang, H., Cid, C.A., Aryanfar, A., & Hoffmann, M.R. (2014). Effects of anodic potential and chloride ion on overall reactivity in electrochemical reactors designed for solar-powered wastewater treatment. *Environmental Science & Technology, 48*(4), 2377–2384. https://doi.org/10.1021/es404137u

19 Oturan, M.A., & Aaron, J.J. (2014). Advanced oxidation processes in water/wastewater treatment: Principles and applications. *Critical Reviews in Environmental Science and Technology, 44*(23), 2577–2641. https://doi.org/10.1080/10643389.2013.829765

20 Duan, X., Ma, F., Yuan, Z., Chang, L., & Jin, X. (2012). Electrochemical degradation of phenol in aqueous solution using PbO_2 anode. *Journal of the Taiwan Institute of Chemical Engineers, 43*(2), 173–180. https://doi.org/10.1016/j.jtice.2011.08.003

21 Sirés, I., & Brillas, E. (2012). Remediation of water pollution caused by pharmaceutical residues based on electrochemical separation and degradation technologies: A review. *Environment International*, *40*, 212–229. https://doi.org/10.1016/j.envint.2011.07.012

22 Moreira, F.C., Boaventura, R.A.R., Brillas, E., & Vilar, V.J.P. (2017). Electrochemical advanced oxidation processes: A review on their application to synthetic and real wastewaters. *Applied Catalysis B: Environmental*, *202*, 217–261. https://doi.org/10.1016/j.apcatb.2016.08.037

23 Dos Santos, A.B., Cervantes, F.J., & van Lier, J.B. (2007). Review paper on current technologies for decolourisation of textile wastewaters: Perspectives for anaerobic biotechnology. *Bioresource Technology, 98*(12), 2369–2385. https://doi.org/10.1016/j.biortech.2006.11.013

24 Holkar, C.R., Jadhav, A.J., Pinjari, D.V., Mahamuni, N.M., & Pandit, A.B. (2016). A critical review on textile wastewater treatments: Possible approaches. *Journal of Environmental Management*, *182*, 351–366. https://doi.org/10.1016/j.jenvman.2016.07.090

25 Ganiyu, S.O., Oturan, N., Raffy, S., Esposito, G., van Hullebusch, E.D., Cretin, M., & Oturan, M.A. (2017). Use of Substoichiometric Titanium Oxide as a Ceramic Electrode in Anodic Oxidation and Electro-Fenton Degradation of the Beta-blocker Propranolol: Degradation Kinetics and Mineralization Pathway. *Electrochimica Acta, 242*, 344–354. https://doi.org/10.1016/j.electacta.2017.05.047

Д.А. Закари, Г.А. Ауду, А.А. Алию, И.О. Мустафа, К.М. Оматола

Модельдік азобояғышты ластаушы ретінде қызғылт метилді электрхимиялық тотықтыру: электродтардың салыстырмалы өнімділігі, ЭИС әдісімен механизмдік талдау және техникалық-экономикалық бағалау

Жұмыста тоқыма және өнеркәсіптік ағын суларға тән модельдік азобояғышты ластаушы ретінде қызғылт метилдің (МО) электрхимиялық тотығуы (ЕО) бор-легирленген алмаз (BDD) және өлшемдік тұрақты анод (DSA) электродтарын жүйелі түрде оңтайландырылған жағдайларда қолдана отырып зерттелген. Модельдік ерітінділер 0,1 M Na_2SO_4 фондық электролиті бар ультражоғары таза суда дайындалды. Эксперименттер 25 ± 1 °C температурада, тұрақты араластыру (300 айн/мин) жағдайында гальваностатикалық режимде жүргізілді. Ток тығыздығы (10–50 мА/см²), pH (2–10) және бастапқы концентрация (50–500 мг/л) өзгертілді. BDD анодтары 120 минут ішінде 94,3 ± 2,1 % ластаушыны жойды (30 мА/см², pH 3,0, 200 мг/л), бұл DSA (87,6 ± 3,3 %) және платина электродтарынан (68,7 ± 4,5 %) айтарлықтай жоғары нәтиже берді. Электрхимиялық импеданс спектроскопиясы (EIS) Randles $R(C_{dl}(R_{ct}W))$ эквиваленттік схемасын қолдана отырып, анодтық потенциалдың (1,0–2,5 В Ag/AgCl) артуымен заряд тасымалдау кедергісінің 73 % төмендегенін көрсетті (R_{ct}: 385 Ω → 104 Ω), бұл Батлер–Фольмер теңдеуімен басқарылатын тотығу кинетикасын растайды. BDD үшін тиімді жылдамдық константасы k_{app} = 0,0315 ± 0,0018 мин$^{-1}$ платинаға қарағанда 1,68 есе жоғары болды. Жалпы органикалық көміртек (ТОС) талдауы BDD қолданғанда толық дерлік минералдануды (96,8 ± 1,5 % ТОС төмендеуі) көрсетті. Меншікті энергия шығыны 8,2 кВт·сағ/м^3 болды, бұл боғарыш ағын суларды өңдеуде әдістің тиімділігін анықтайды. Нигериядағы электр энергия тарифі (₦45/кВт·сағ) бойынша өңдеу құны шамамен ₦369/м^3, бұл дамушы елдерде өнеркәсіптік қолдану үшін әлеуетті тиімділікті көрсетеді.

Кілт сөздер: электрхимиялық тотығу, бор-легирленген алмаз, азобояғыштардың ыдырауы, қызғылт метил, өлшемдік тұрақты анод, электрхимиялық импеданс спектроскопиясы, минералдану, модельдік ластаушы, заряд тасымалдау кедергісі, гидроксил радикалдары, псевдо-бірінші ретті кинетика, техникалық-экономикалық бағалау

Д.А. Закари, Г.А. Ауду, А.А. Алию, И.О. Мустафа, К.М. Оматола

Электрохимическое окисление метилового оранжевого как модельного загрязнителя азокрасителей: сравнительная эффективность электродов, механистический анализ методом ЭИС и технико-экономическая оценка

Данное исследование посвящено электрохимическому окислению (ЕО) метилового оранжевого (МО) как модельного загрязнителя азокрасителей, характерного для текстильных и промышленных сточных вод, с использованием анодов из бор-легированного алмаза (BDD) и размерно-стабильных анодов (DSA) в систематически оптимизированных условиях. Модельные растворы готовились в ультрачистой воде с использованием 0,1 М Na_2SO_4 в качестве фонового электролита. Пакетные эксперименты проводились в гальваностатическом режиме при температуре 25 ± 1 °C при постоянном перемешивании (300 об/мин) с варьированием плотности тока (10–50 мА/см²), pH (2–10) и начальной концентрации метилового оранжевого (50–500 мг/л). Аноды BDD обеспечили 94,3 ± 2,1 % удаления загрязнителя за 120 мин при оптимальных условиях (30 мА/см², pH 3,0, 200 мг/л), значительно превосходя DSA (87,6 ± 3,3 %) и платиновые электроды (68,7 ± 4,5 %). Электрохимическая импедансная спектроскопия (EIS) с использованием эквивалентной схемы Рэндлса $R(C_{dl}(R_{ct}W))$ показала снижение сопротивления переноса заряда на 73 % (Rct: 385 Ω → 104 Ω) при увеличении анодного потенциала (1,0–2,5 В относительно Ag/AgCl), что подтверждает кинетику окисления, контролируемую уравнением Батлера–Фольмера. Константа кажущейся скорости k_{app} = 0,0315 ± 0,0018 мин$^{-1}$ для BDD была в 1,68 раза выше, чем для платины. Анализ общего органического углерода (TOC) подтвердил почти полную минерализацию (96,8 ± 1,5 % снижения TOC) при использовании BDD. Удельное энергопотребление составило 8,2 кВт·ч/м³, что указывает на конкурентоспособность метода для очистки красителей. При тарифе на электроэнергию в Нигерии (₦45/кВт·ч) расчетная стоимость обработки составляет ₦369/м³, что свидетельствует о потенциальной применимости в промышленности развивающихся стран при условии проверки на реальных сточных водах.

Ключевые слова: электрохимическое окисление, бор-легированный алмаз, разложение азокрасителей, метиловый оранжевый, размерно-стабильный анод, электрохимическая импедансная спектроскопия, минерализация, модельный загрязнитель, сопротивление переноса заряда, гидроксильные радикалы, кинетика псевдопервого порядка, технико-экономическая оценка

Information about the authors

Zakari, David Adeiza (*corresponding author*) — PhD, Associate Professor, Department of Microbiology, Prince Abubakar Audu University, Anyigba, Nigeria; e-mail: david.z@ksu.edu.ng; ORCID: https://orcid.org/0000-0002-7111-6065

Audu, Godwin Amoka — MSc, Research Officer, Department of Biochemistry, Prince Abubakar Audu University, Anyigba, Nigeria; e-mail: audu.ga@ksu.edu.ng; ORCID: https://orcid.org/0009-0001-6987-9442

Aliyu, Abdulbasit Anoze — PhD, Senior Lecturer, Department of Pure and Industrial Chemistry, Prince Abubakar Audu University, Anyigba, Nigeria; e-mail: abdulbasit.a@ksu.edu.ng; ORCID: https://orcid.org/0000-0002-0166-1228

Mustapha, Idris Omenesa — Postdoctoral Fellow, Interdisciplinary Research Center for Membranes and Water Security, King Fahd University of Petroleum and Minerals, Dhahran, Saudi Arabia; e-mail: idris-mustapha710@gmail.com; ORCID: https://orcid.org/0000-0003-4799-1959

Omatola, Kingsley Makoji — PhD, Associate Professor, Department of Physics, Prince Abubakar Audu University, Anyigba, Nigeria; e-mail: omatola.k@ksu.edu.ng; ORCID: https://orcid.org/0009-0008-5756-1251

Article

UDC 621.793

https://doi.org/10.31489/2026PH2/58-67

Received: 12.02.2026
Accepted: 02.04.2026

M. Maulet[1]✉, Zh.B. Sagdoldina[1], N.N. Yusof[2], A.K. Khassenov[3]

[1]*Sarsen Amanzholov East Kazakhstan University, Ust-Kamenogorsk, Kazakhstan;*
[2]*University Sains Malaysia, 11800 Pulau Pinang, Malaysia;*
[3]*Buketov Karaganda National Research University, Karaganda, Kazakhstan*

Investigation of Detonation-Sprayed NiCr–Al Coatings Tested under Real Operating Conditions of a Thermal Power Plant

This study presents the experimental results of high-temperature oxidation testing under actual operating conditions in a thermal power plant of gradient and homogeneous composite NiCr–Al coatings produced by the detonation spraying method. To characterize the degradation mechanisms of the tested coatings, systematic analyses were performed, including phase composition evaluation, and detailed microstructural examination using scanning electron microscopy (SEM). The evolution of oxide layers and elemental redistribution across the coating thickness were also assessed to clarify the influence of coating architecture on protective performance. The experimental results demonstrated that the gradient composite NiCr–Al coatings exhibit superior resistance to high-temperature oxidation compared to homogeneous coatings. The gradient architecture effectively preserved structural integrity and promoted a more uniform distribution of aluminum and chromium within the coating thickness. This compositional optimization facilitated the formation of continuous and adherent protective oxide layers, predominantly Al_2O_3 and Cr_2O_3, which significantly reduced oxidation kinetics and inhibited coating degradation. In contrast, the homogeneous NiCr–Al coatings showed noticeable aluminum depletion, crack formation, and oxide scale spallation after prolonged exposure to high-temperature industrial conditions. The findings of this study confirm that gradient NiCr–Al coatings deposited by detonation spraying represent a promising protective solution for components operating in severe high-temperature and corrosive environments, offering improved durability and extended service life for industrial and energy related applications.

Keywords: NiCrAl coatings, detonation spraying technology, high temperature properties, thermal power plant

✉*Corresponding author*: Maulet, Meruyert, mauletmeruert@gmail.com

Introduction

Structural steel components used in modern energy and heavy industrial sectors, particularly in coal- and biomass-fired thermal power plants, are subjected to complex degradation phenomena such as high-temperature oxidation, hot corrosion, erosion, and abrasive wear [1]. Boiler tubes, water walls, economizers, and superheaters, when operated for prolonged periods in aggressive gas environments containing sulfur, chlorine, alkali metal salts, and fly ash particles, undergo accelerated degradation, leading to a reduced service life of the equipment, increased maintenance and repair costs, and decreased efficiency of power generation systems. The synergistic nature of these degradation processes accelerates the breakdown of protective oxide layers, ultimately resulting in premature material failure [2–4].

One of the effective approaches to addressing these issues is the application of protective coatings on steel surfaces, which has become widely adopted. In recent years, coatings produced by thermal spraying techniques have gained particular importance for protection against high-temperature corrosion and oxidation. HVOF, HVAF, detonation, and plasma spraying technologies enable the deposition of dense coatings with high adhesion and relatively low porosity using metallic, ceramic, and cermet materials. In particular, FeCr-, NiCr-, and NiCrAl-based alloys, as well as carbide-based composite coatings (Cr_3C_2–NiCr, WC–Co–Cr), are considered effective protective solutions against erosion and corrosion in power plant boilers [5-6]. In carbide-based systems, the protective effect is primarily provided by the physical barrier role of hard carbide phases (Cr_3C_2, WC, W_2C), and such coatings exhibit high effectiveness under short- and medium-term cyclic exposure conditions [7]. However, during long-term high-temperature service, oxidation or decarburization of carbides may limit their protective performance. Consequently, recent studies have placed particular emphasis on aluminum-forming coatings, as the Al_2O_3 layer formed on their surface can significantly suppress oxidation and hot corrosion [8]. However, long-term tests conducted under industrial operating conditions have shown that, although pure Ni and nickel aluminide (Ni_2Al_3) coatings provide effective protection in the initial stages, their service life is limited due to the chemical instability of the γ-Al_2O_3 layer under the influence of KCl present in biomass combustion products, selective aluminum depletion, and the subsequent breakdown of the protective layer [9]. This indicates that the long-term stability of aluminum-forming systems is not determined solely by the formation of Al_2O_3 and that additional elements are required to enhance the chemical stability of the protective layer.

From this perspective, chromium-containing NiCrAl coatings are regarded as an intermediate and promising protective system. In such coatings, the Cr_2O_3 layer provides initial protection at low and intermediate temperatures, while the formation of an Al_2O_3 layer at higher temperatures enhances long-term stability. The presence of chromium partially compensates for the chemical instability of γ-Al_2O_3 and helps mitigate chlorine-induced corrosion. In addition, the dense microstructure and low porosity of NiCrAl coatings produced by detonation spraying and HVOF methods form an effective barrier against erosion-induced corrosion [10–12].

At present, it is becoming evident that the performance of single-layer coatings is limited in energy systems subjected simultaneously to high temperature, corrosion, and erosion. Consequently, multilayer and functionally graded thermally sprayed coatings are being considered as a promising approach. Such architectures reduce the thermal and mechanical mismatch between the coating and the substrate, improve adhesion, and decrease residual stresses [13]. The aim of this work is to test and comparatively investigate homogeneous and gradient NiCrAl coatings produced by detonation spraying under industrial operating conditions.

Materials and Methods

NiCr–Al coatings were deposited onto 12Kh1MF heat resistance steel substrates (ISO 4955 standard). The steel was machined into discs measuring 50 mm in diameter and 3 mm in thickness. Before the coating process, the substrate surfaces were sequentially ground with SiC sandpapers of 120–2000 grit size to obtain a uniform finish. To enhance the adhesion of the coatings, the prepared substrates were additionally subjected to sandblasting treatment. Composite powders were prepared using Ni75Cr25 alloy powder and high-purity Al powder (99.99 %). The powder mixture was homogenized and mechanically activated in a BML-6 ball mill. The average particle size of the NiCr–Al composite powder is 68 μm.

Homogeneous and gradient NiCr–Al coatings were produced using the CCDS2000 detonation spraying system. The study demonstrated that gradient-composition NiCr–Al coatings can be obtained by adjusting the filling volume of the detonation barrel with the explosive gas during detonation spraying [14-15]. The technological parameters for producing the coatings are presented in Table 1.

Table 1

Technological parameters for producing the NiCr–Al detonation coating

Coating structure	O_2/C_2H_2	Spray Distance, mm	Barrel Filling Volume,%	Number of Shots
Homogeneous	1.856	150	50	40
Gradient	1.856	150	50	10
			40	10
			30	10
			25	10

For the high-temperature tests, specimens with geometric dimensions of 15×15×3 mm were prepared. The samples were fabricated by detonation spraying and fully coated with NiCr–Al on all six surfaces.

The high-temperature oxidation testing of the coatings was conducted in an industrial environment at the Sogra Thermal Power Plant (TPP) in Ust-Kamenogorsk, Kazakhstan. In this test, NiCr–Al coated specimens were placed in the high-temperature zone of the TPP (≈700 °C) and exposed to actual service conditions for a period of two weeks. The duration of exposure was selected based on literature data [16]. The industrial atmosphere of the thermal power plant is characterized by the presence of oxygen, water vapor, and combustion products, including sulfur- and chlorine-containing species, as well as fly ash particles. These factors create an aggressive high-temperature environment that promotes oxidation and corrosion processes. To ensure the reliability of the results, at least three coated samples were tested under identical conditions. The obtained results demonstrated good repeatability, as consistent trends in phase composition, oxide formation, and microstructural evolution were observed across all samples.

The phase composition of the coatings was examined using an X'Pert PRO X-ray diffractometer (PANalytical, Netherlands). X-ray diffraction analysis was performed with CuKα radiation under the following conditions: 40 kV accelerating voltage, 30 mA tube current, 1 s exposure time, step size of 0.02°, and a 2θ range of 10°–90°. The obtained diffractograms were processed using HighScore software in conjunction with the PDF2 database. The surface microstructure and cross-sectional morphology of the coatings were investigated by scanning electron microscopy (SEM, SEM3200, China), while the elemental composition was determined by energy-dispersive X-ray spectroscopy (EDX, Bruker, USA).

Results and Discussion

Figure 1 presents the X-ray phase analysis results for the structure of homogeneous-composition and gradient-composition NiCr–Al coatings. It can be observed that the homogeneous-composition NiCr–Al coating consists mainly of the $CrNi_3$ phase. During the deposition process, the elevated temperatures prevented the formation of Al phases on the homogeneous-composition NiCr–Al coating surface. In contrast, the gradient-composition NiCr–Al coatings contains both $CrNi_3$ and Al phases. The appearance of the Al phase is attributed to the reduced filling volume of the detonation barrel with the explosive gas mixture during deposition [17].

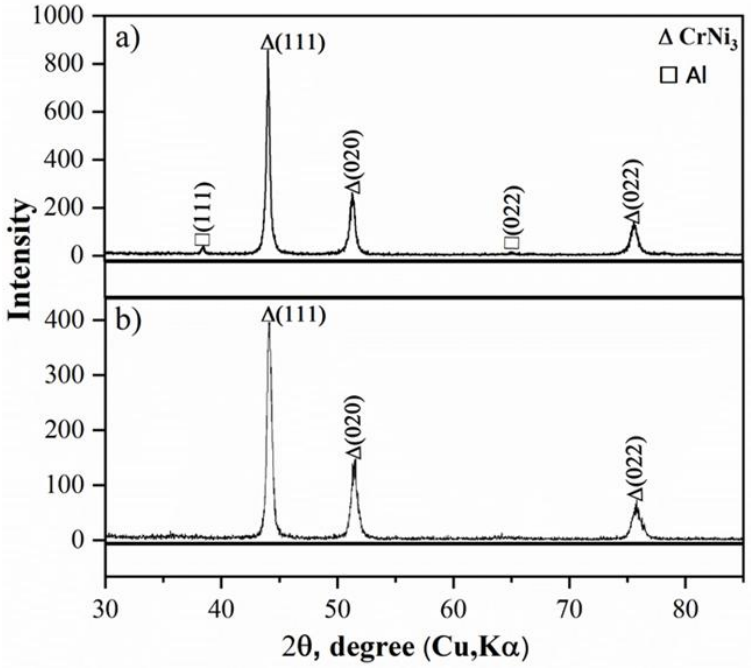

Figure 1. Results of the X-ray diffraction phase analysis for NiCr–Al coatings: a) Gradient; b) Homogeneous

Figure 2 presents cross-sectional micrographs of the homogeneous-composition and gradient-composition NiCr–Al coatings. In the microstructure of the homogeneous-composition NiCr–Al coating, distinct phase separation of the components can be observed. By progressively reducing the detonation

energy (from 50 % to 25 %), a gradient-composition NiCr–Al coatings was produced with an increased Al content in the surface layer, which contributed to a relatively high coating density (Fig. 2*a*). In contrast, the surface layer of the homogeneous-composition NiCr–Al coating exhibited a lower microstructural density. The study revealed that the coating obtained at a 50 % filling of the detonation barrel with explosive gases contained only a limited amount of Al. Consequently, the insufficient quantity of molten Al between $CrNi_3$ particles hindered the formation of a dense matrix, leading instead to a porous NiCr–Al coating (Fig. 2*b*) [18].

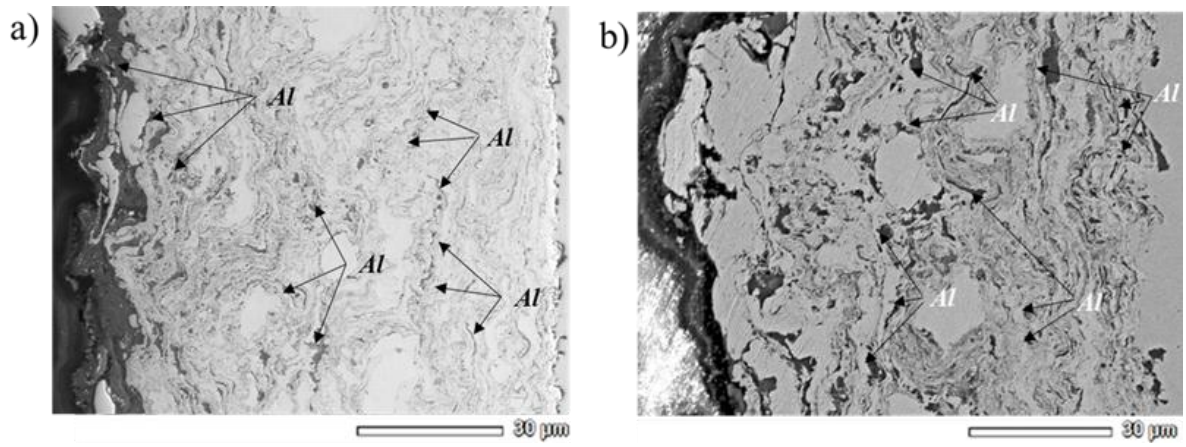

Figure 2. Cross-sectional microstructure of NiCr–Al coatings: *a*) Gradient; *b*) Homogeneous

Figure 3 shows the X-ray phase analysis results of homogeneous-composition and gradient-composition NiCr–Al coatings after high-temperature testing under industrial conditions. As can be seen, the gradient-composition NiCr–Al coating (Fig. 3*a*) is dominated by the $CrNi_3$ intermetallic phase, which indicates its high thermal stability. In addition, protective oxides such as Cr_2O_3 and Al_2O_3 were formed on the coating surface. This phase composition demonstrates the enhanced oxidation and corrosion resistance of the gradient-composition NiCr–Al coatings. Furthermore, the CrO_3 oxidized chromium phase, which typically forms under aggressive oxidation conditions, was also detected on the coating surface. In contrast, for the homogeneous-composition NiCr–Al coating, although the $CrNi_3$ phase was retained, oxidation-resistant oxides (Al_2O_3, Cr_2O_3) were either scarce or not detected at all. This indicates the weaker ability of the homogeneous-composition NiCr–Al coating to form a protective layer.

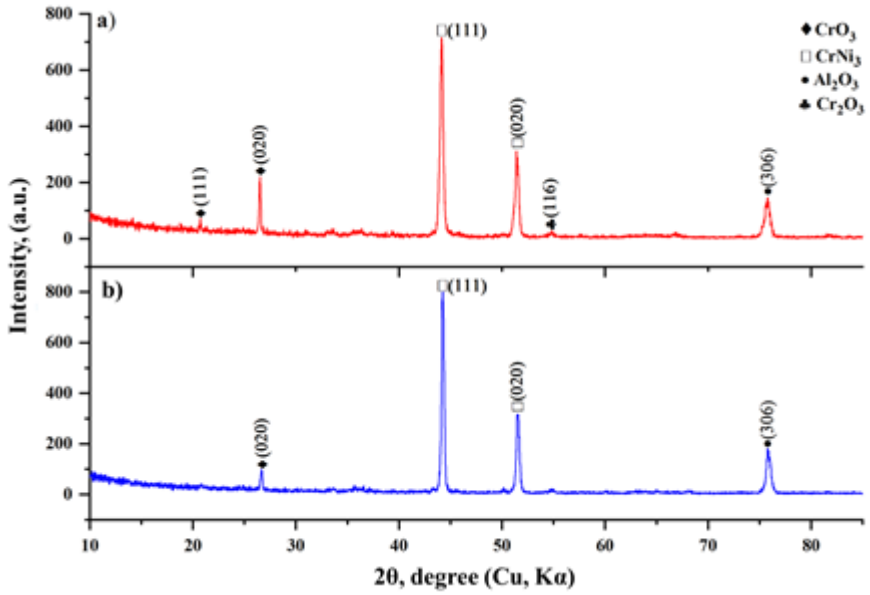

Figure 3. X-ray phase analysis results of NiCr–Al coatings after high-temperature testing under industrial conditions: *a*) homogeneous; *b*) gradient

Figure 4 presents the SEM cross-sectional images of homogeneous-composition and gradient-composition NiCr–Al coatings after high-temperature testing under industrial conditions. These results provide an assessment of the internal structure and structural changes of the coatings after thermal exposure. In the cross-section of the homogeneous-composition NiCr–Al coating (Fig. 4*a*), cracks, porosity, and fragmented regions are clearly visible within the coating. In some areas, structural disintegration is observed. These changes indicate that oxidation and thermal fatigue processes occurred intensively under high temperature and aggressive atmospheric conditions. In contrast, the gradient-composition NiCr–Al coating (Fig. 4*b*) exhibits fewer microcracks and pores, and no signs of fragmentation or delamination are observed in the internal regions of the coating. A certain degree of surface oxidation is present, but this is attributed to the formation of a protective oxide layer, which helps to suppress coating degradation.

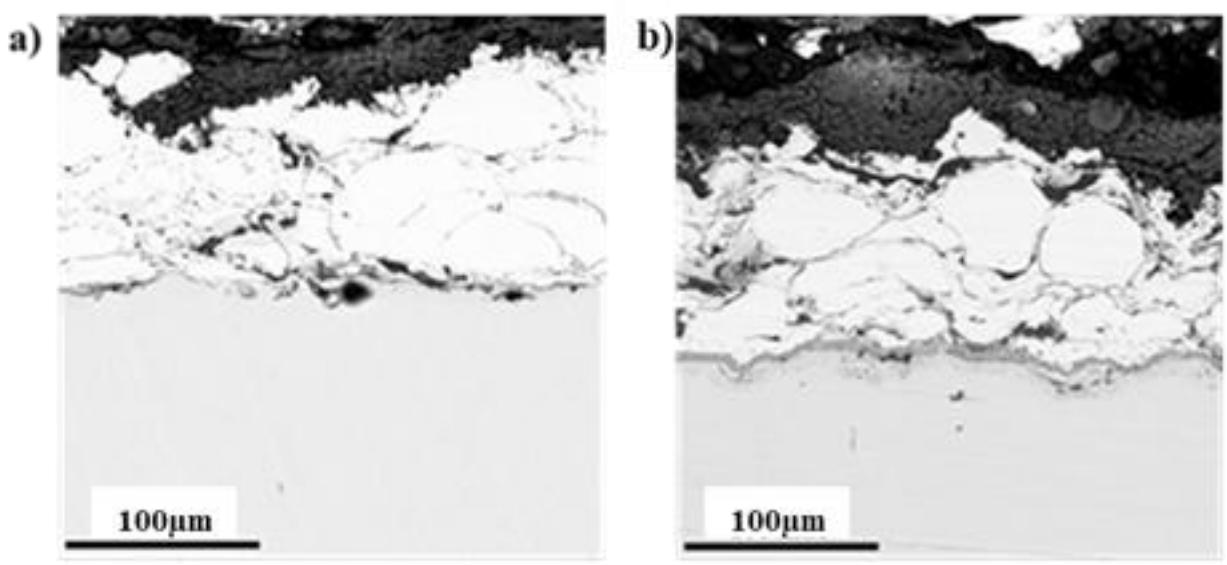

Figure 4. SEM cross-sectional image of NiCr–Al coatings after high-temperature testing under industrial conditions: *a*) homogeneous; *b*) gradient

Figure 5 shows the EDS results of the cross-section of the homogeneous-composition NiCr–Al coating after high-temperature testing under industrial conditions. Within the coating, Cr and Ni elements are uniformly distributed, representing the main constituents of the coating. According to the spectral analysis, the Al content in the coating is relatively low, with a noticeable concentration only near the surface. This indicates the formation of a protective Al_2O_3 oxide layer on the surface during high-temperature oxidation. The elemental mapping results reveal that oxygen (O) and aluminum (Al) are concentrated in the upper region of the coating, confirming the presence of an oxide layer. Based on the line scan analysis, Fe content sharply increases within ~100 μm from the coating surface, which marks the boundary between the coating and the substrate. Overall, the EDS analysis demonstrates that, after high-temperature exposure under industrial conditions, the homogeneous-composition NiCr–Al coating underwent oxidation and formed a surface oxide protective layer. However, the low aluminum content in the coating suggests insufficient capability for long-term protection of the substrate.

Figure 6 presents the EDS results obtained from the cross-section of the gradient-composition NiCr–Al coatings after high-temperature testing under industrial conditions. The analysis reveals the elemental distribution between the coating and the substrate, the oxidation process, as well as the advantages of the gradient structure. According to the line scan profile, aluminum (Al) and chromium (Cr) are highly con-centrated in the surface layer of the coating, which facilitates the formation of protective oxides such as Al_2O_3 and Cr_2O_3. Spectral analysis taken at different points from the substrate toward the coating surface shows that the aluminum content gradually increases toward the surface. Elemental mapping demonstrates that nickel (Ni) and chromium (Cr) are uniformly and predominantly distributed within the inner regions of the coating, while iron (Fe) is localized in the bottom region, clearly indicating the boundary between the substrate and the coating. These EDS results confirm that the gradient-composition NiCr–Al coatings possesses high oxidation resistance and good structural integrity under industrial high-temperature conditions.

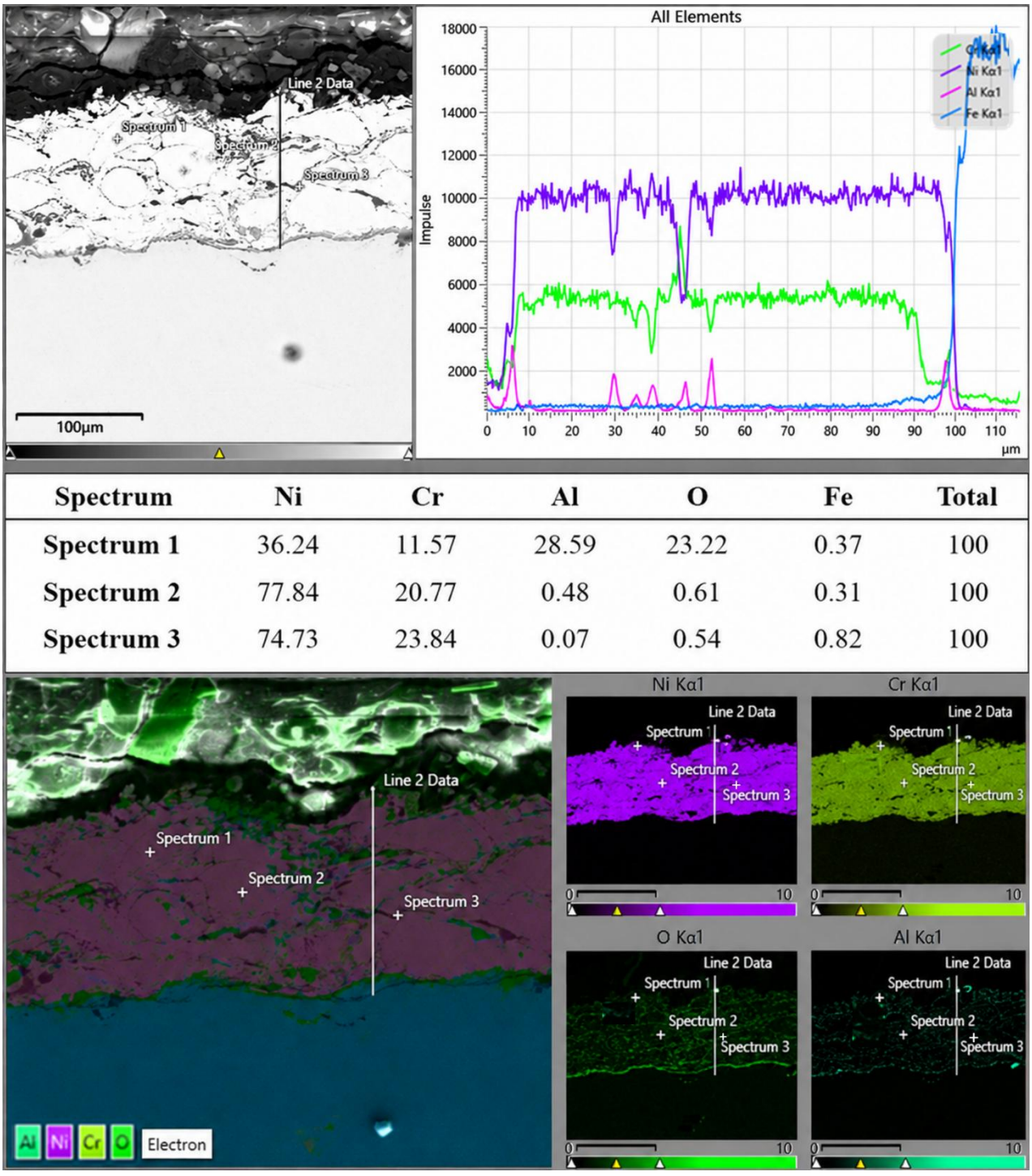

Spectrum	Ni	Cr	Al	O	Fe	Total
Spectrum 1	36.24	11.57	28.59	23.22	0.37	100
Spectrum 2	77.84	20.77	0.48	0.61	0.31	100
Spectrum 3	74.73	23.84	0.07	0.54	0.82	100

Figure 5. Cross-sectional EDS analysis of the homogeneous-composition NiCr–Al coating after exposure to high-temperature testing in an industrial environment

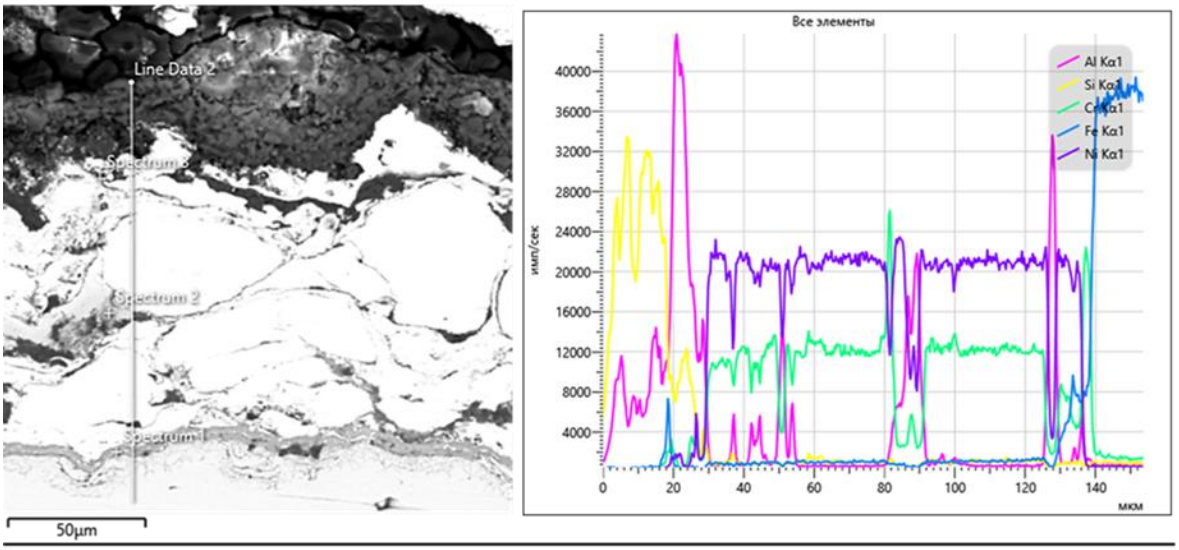

Spectrum	Ni	Cr	Al	O	Fe	Total
Spectrum 1	58.01	20.34	6.23	4.3	11.12	100
Spectrum 2	53.91	17.64	16.96	11.20	0.29	100
Spectrum 3	43.93	12.61	29.06	14.40	-	100

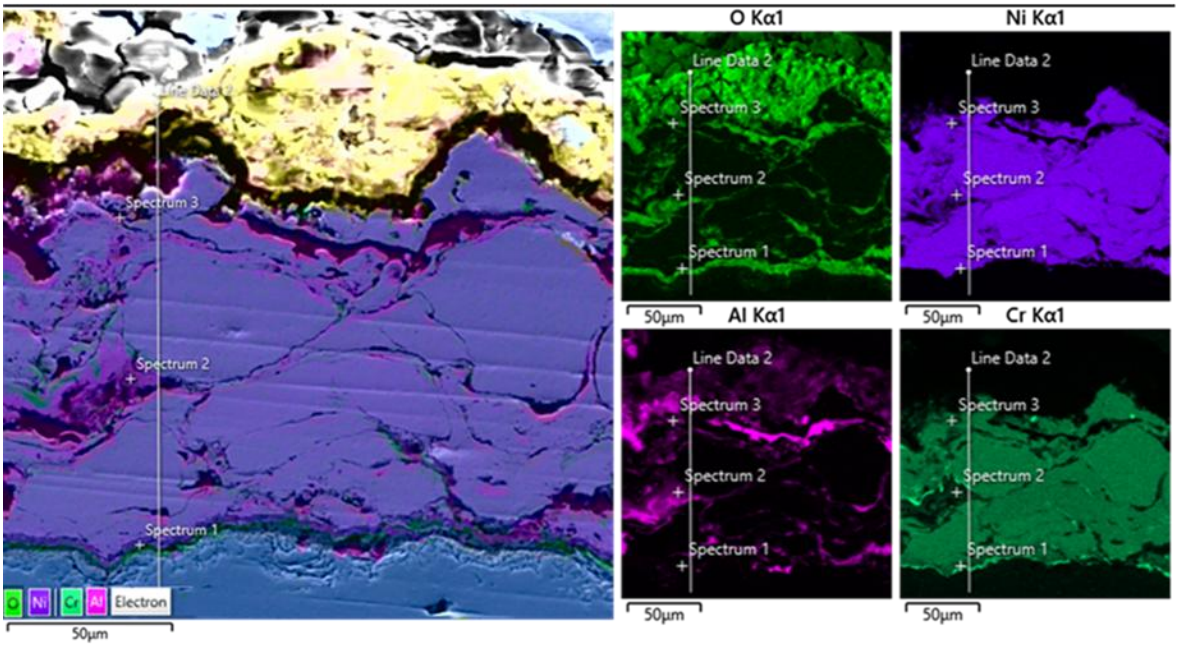

Figure 6. Cross-sectional EDS analysis of the gradient composition NiCr–Al coating after exposure to high-temperature testing in an industrial environment

Conclusion

Based on the results following conclusions can be drawn:

– After high-temperature oxidation testing under industrial operating conditions, the homogeneous composite NiCr–Al coating exhibited a pronounced reduction in aluminum concentration accompanied by structural degradation, including crack formation and oxide scale spallation. In contrast, the gradient composite NiCr–Al coating showed a more favorable elemental distribution along the coating thickness, particularly for aluminum and chromium.

– The optimized compositional gradient promoted the formation of continuous and adherent protective oxide layers, primarily Al_2O_3 and Cr_2O_3, on the coating surface. These oxides acted as effective diffusion barriers, significantly improving oxidation resistance and mitigating further material degradation at elevated temperatures.

– The superior performance of the gradient composite NiCr–Al coating can be attributed to the combined effect of its tailored chemical architecture and enhanced thermomechanical compatibility between coating layers, which reduces thermal stresses and improves long-term stability under severe service conditions.

Funding

This research has been funded by the Committee of Science of the Ministry of Science and Higher Education of the Republic of Kazakhstan (Grant No. AP22688426).

References

1 Deepak, D., Parlad, K., & Jasmaninder, S.G. (2021). A review of thermal spray coatings for protection of steels from degradation in coal-fired power plants. *Corrosion Reviews*, *39*(3), 243–268. https://doi.org/10.1515/corrrev-2020-0043.

2 Wu, D.L., Dahl, K.V., Christiansen, T.L., Montgomery, M., & Hald, J. (2019). Corrosion behaviour of Ni and nickel aluminide coatings exposed in a biomass-fired power plant for two years. *Surface & Coatings Technology*, *362*, 355–365. https://doi.org/10.1016/j.surfcoat.2018.12.129.

3 Oksa, M., Auerkari, P., Salonen, J., & Varis, T. (2014). Nickel-based HVOF coatings promoting high-temperature corrosion resistance of biomass-fired power plant boilers. *Fuel Processing Technology*, *125*, 236–245. https://doi.org/10.1016/j.fuproc.2014.04.006.

4 Kissabekova, P.A., Karabekova, D.Zh., Khassenov, A.K., Kucheruk, V.Yu., Kudussov, A.S., & Kyzdarbekova, Sh.S. (2023). Theoretical foundations of the construction of the operation of heat flow devices. *Bulletin of the University of Karaganda-Physics*, *1*(109), 80–87. https://doi.org/10.31489/2023ph1/80-87.

5 Formanek, B., Szymański, K., Szczucka-Lasota, B., & Włodarczyk, A. (2005). New generation of protective coatings intended for the power industry. *Journal of Materials Processing Technology*, *164-165*, 850–855. https://doi.org/10.1016/j.jmatprotec.2005.02.098.

6 Sidhu, V., Goyal, K., & Goyal, R. (2017). Comparative study of corrosion behaviour of HVOF-coated boiler steel in the actual boiler environment of a thermal power plant. *Journal of the Australian Ceramic Society*, *53*, 1–8. https://doi.org/10.1007/s41779-017-0107-x.

7 Szymański, K., Hernas, A., Moskal, G., & Myalska, H. (2015). Thermally sprayed coatings resistant to erosion and corrosion for power plant boilers: A review. *Surface & Coatings Technology*, *268*, 153–164. https://doi.org/10.1016/j.surfcoat.2014.10.046.

8 Medvedovski, E., & Dudziak, T. (2019). Protective coatings for high-temperature steam oxidation in coal-fired power plants. *Surface & Coatings Technology*, *369*, 127–141. https://doi.org/10.1016/j.surfcoat.2019.04.049.

9 Wu, D.L., Dahl, K.V., Grumsen, F.B., Christiansen, T.L., Montgomery, M., & Hald, J. (2020). Breakdown mechanism of γ-Al_2O_3 on Ni_2Al_3 coatings exposed in a biomass-fired power plant. *Corrosion Science*, *170*, 108583. https://doi.org/10.1016/j.corsci.2020.108583.

10 Oksa, M., Metsäjoki, J., & Kärki, J. (2016). Corrosion testing of thermal spray coatings in a biomass co-firing power plant. *Coatings*, *6*, 1–13. https://doi.org/10.3390/coatings6040065

11 Mishra, S.B., Chandra, K., & Prakash, S. (2013). Erosion–corrosion performance of NiCrAlY coating produced by plasma spray process in a coal-fired thermal power plant. *Surface & Coatings Technology*, *216*, 23–34. https://doi.org/10.1016/j.surfcoat.2012.09.044.

12 Hussain, T., Dudziak, T., Simms, N.J., & Nicholls, J.R. (2013). Fireside corrosion behavior of HVOF- and plasma-sprayed coatings in advanced coal/biomass co-fired power plants. *Journal of Thermal Spray Technology*, *22*, 797–807. https://doi.org/10.1007/s11666-013-9887-x.

13 Sharun, V., Rajasekaran, M., Suresh Kumar, S., Tripathi, V., Sharma, R., Puthilibai, G., Sudhakar, M., & Negash, K. (2022). Study on developments in protection coating techniques for steel. *Advances in Materials Science and Engineering*, *2022*, 1–10. https://doi.org/10.1155/2022/2843043.

14 Rakhadilov, B., Sagdoldina, Zh., Maulet, M., Buitkenov, D., & Sulubayeva, L. (2024). *Method of obtaining functionally gradient coating.* Patent for Utility Model No. 8922, Republic of Kazakhstan.

15 Maulet, M., Sagdoldina, Zh.B., Rakhadilov, B.K., Kakimzhanov, D.N., & Magazov, N.M. (2022). Influence of the aluminum content on the structure of gradient detonation coatings based on NiCr–Al. *Bulletin of the University of Karaganda-Physics, 107*(3), 18–24. https://doi.org/10.31489/2022ph3/18-24.

16 Jiang, S.M., Li, H.Q., Ma, J., Xu, C.Z., Gong, J., & Sun, C. (2010). High-temperature corrosion behaviour of a gradient NiCoCrAlYSi coating II: Oxidation and hot corrosion. *Corrosion Science, 52*(7), 2316–2322. https://doi.org/10.1016/j.corsci.2010.03.032.

17 Rakhadilov, B., Maulet, M., Abilev, M., Sagdoldina, Zh., & Kozhanova, R. (2021). Structure and tribological properties of Ni–Cr–Al-based gradient coating prepared by detonation spraying. *Coatings*, *11*(2), 218. https://doi.org/10.3390/coatings11020218.

18 Sagdoldina, Zh., Rakhadilov, B., Maulet, M., Sulyubayeva, L., Dreanda, C., & Bolatov, S. (2025). Comprehensive study of the mechanical and tribological properties of NiCr–Al detonation coatings. *Applied Sciences*, *15*(13), 7513. https://doi.org/10.3390/app15137513.

М. Маулет, Ж.Б. Сагдолдина, Н.Н. Юсуф, А.К. Хасенов

Жылу электр станциясының нақты жұмыс жағдайларында сыналған детонациялық бүрку арқылы алынған NiCr–Al жабындарын зерттеу

Жұмыста детонациялық бүрку әдісімен алынған градиентті және біртекті композициялық NiCr–Al жабындарының жылу электр станциясының нақты жұмыс жағдайларында жоғары температуралық тотығуға төзімділігі бойынша жүргізілген эксперименттік зерттеулердің нәтижелері ұсынылған. Сынақтан өткен жабындардың деградация механизмдерін сипаттау мақсатында фазалық құрамды бағалау және сканерлеуші электрондық микроскопия әдісін қолдана отырып, микрокұрылымды талдау сияқты жүйелі зерттеулер жүргізілді. Қорғаныштық тиімділікке жабын құрылымының әсерін нақтылау мақсатында жабын қалыңдығы бойынша оксидтік қабаттардың өзгерісі мен элементтердің таралуы бағаланды. Эксперименттік нәтижелер градиентті композициялық NiCr–Al жабындарының біртекті жабындармен салыстырғанда ыстық коррозияға және жоғары температуралық тотығуға төзімділігі жоғары екенін көрсетті. Градиентті жабын құрылымдық тұтастығын тиімді түрде сақтауға мүмкіндік беріп, жабын қалыңдығы бойымен алюминий мен хром элементтерінің неғұрлым біркелкі таралуын қамтамасыз етті. Мұндай құрамдық оңтайландыру негізінен Al_2O_3 және Cr_2O_3 типтес үздіксіз әрі адгезиясы жоғары қорғаныш оксидтік қабаттардың қалыптасуына ықпал етіп, тотығуды төмендетті және жабынның деградациялануын тежеді. Ал біртекті NiCr–Al жабындарында жоғары температуралы өнеркәсіптік жағдайларда ұзақ уақыт әсер ету нәтижесінде алюминийдің айқын сарқылуы, жарықшақтардың түзілуі және оксидтік қабаттың қабыршақтанып бөлінуі байқалды. Зерттеу нәтижелері детонациялық бүрку әдісімен алынған градиентті NiCr–Al жабындарының жоғары температуралы және коррозиялық әсері күшті ортада жұмыс істейтін бөлшектерді қорғау үшін перспективалы екенін көрсетті, бұл өнеркәсіптік және энергетикалық қолданбаларда олардың ұзақ мерзімділігін арттырып, қызмет ету мерзімін ұзартады.

Кілт сөздер: NiCr–Al жабыны, детонациялық бүрку технологиясы, жоғары температуралық қасиеттер, ЖЭС

М. Маулет, Ж.Б. Сагдолдина, Н.Н. Юсуф, А.К. Хасенов

Исследование покрытий NiCr–Al полученных методом детонационного напыления испытанных в реальных условиях эксплуатации теплоэлектростанции

В данной работе представлены экспериментальные результаты испытаний на высокотемпературное окисление в реальных условиях эксплуатации теплоэлектростанции градиентных и однородных композиционных покрытий NiCr–Al, полученных методом детонационного напыления. Исследуемые покрытия подвергались воздействию агрессивных промышленных сред с целью оценки их структурной стабильности, стойкости к окислению и коррозионной стойкости в условиях повышенных температур. Для характеристики механизмов деградации исследуемых покрытий были проведены систематические анализы, включающие оценку фазового состава и детальное исследование микроструктуры с использованием сканирующей электронной микроскопии (SEM). Для уточнения влияния архитектуры покрытия на его защитную эффективность также были оценены эволюция оксидных слоёв и перераспределение элементов по толщине покрытия. Экспериментальные результаты показали, что градиентные композиционные покрытия NiCr–Al по сравнению с однородными покрытиями обладают более высокой стойкостью к высокотемпературному окислению. Градиентная архитектура эффективно сохраняла структурную целостность покрытия и способствовала более равномерному распределению алюминия и хрома по всей толщине покрытия. Данная оптимизация состава способствовала формированию непрерывных и хорошо адгезированных защитных оксидных слоёв, преимущественно Al_2O_3 и Cr_2O_3, что существенно снизило кинетику окисления и подавило деградацию покрытия. В отличие от этого, однородные покрытия NiCr–Al после длительного воздействия высокотемпературных промышленных условий демонстрировали заметное истощение алюминия, образование трещин и отслаивание оксидной окалины. Результаты настоящего исследования подтверждают, что градиентные покрытия NiCr–Al, нанесённые методом детонационного напыления, представляют собой перспективное защитное решение для компонентов, работающих в условиях высоких температур и агрессивных корро-

зионных сред, обеспечивая повышенную долговечность и увеличение срока службы в промышленном и энергетическом применении.

Ключевые слова: покрытия NiCr–Al, технология детонационного напыления, высокотемпературные свойства, ТЭЦ

Information about the authors

Maulet, Meruyert (*corresponding author*) — PhD, Senior Researcher of Scientific Research Center "Surface Engineering and Tribology", Sarsen Amanzholov East Kazakhstan University; e-mail: mauletmeruert@gmail.com. ORCID ID: https://orcid.org/0000-0003-1570-0301

Sagdoldina, Zhuldyz — PhD, Associate Professor, Senior Researcher of Scientific Research Center "Surface Engineering and Tribology", Sarsen Amanzholov East Kazakhstan University, Ust-Kamenogorsk, Kazakhstan; e-mail: sagdoldina@gmail.com. ORCID ID: https://orcid.org/0000-0001-6421-2000

Yusof, Nur Nabihah Binti — PhD, Associate Professor at School of Physics, University Sains Malaysia, Pulau Pinang, Malaysia; e-mail: nurnabihah7@usm.my. ORCID ID: https://orcid.org/0000-0002-6303-4908

Khassenov, Ayanbergen — PhD, Professor, Buketov Karaganda National Research University, Karaganda, Kazakhstan; e-mail: ayanbergen@mail.ru; ORCID ID:https://orcid.org/0000-0002-5220-9469

Article

UDC 544.42+519.242.7

https://doi.org/10.31489/2026PH2/68-82

Received: 02.02.2026
Accepted: 06.04.2026

E. Somuncu✉

Department of Medical Services and Techniques, Usak Ulubey Vocational School, Usak University, Usak, Turkey, 64000

The Accurate Evaluation of the Intermolecular Potential Parameters and its Applications

Accurate determination of intermolecular potential parameters is essential for predicting thermophysical properties of real gases, particularly heavy polyatomic fluorides of industrial relevance. In this study, Morse potential parameters for MoF_6, IF_5, and WF_6 gases were obtained using a nonlinear least-squares fitting algorithm based on Lennard–Jones (12–6) interaction energy data, where the root-mean-square error (RMSE) was used as the minimization criterion. The obtained parameters were validated by calculating the second virial coefficient, heat capacity at constant pressure, and speed of sound, and comparing the results with available experimental data over the temperature range 298–400 K. Quantitative accuracy was assessed using RMSE, mean relative error (MRE), and correlation coefficient (R). For the second virial coefficient, RMSE values were 31, 264, and 149 $cm^3 \cdot mol^{-1}$ for MoF_6, IF_5, and WF_6, respectively, with corresponding MRE values of 3.3 %, 11 %, and 18.5 %, and strong correlations ($R \geq 0.978$). In addition, deviations for speed of sound and heat capacity remained within 1–2 % and below 1 %, respectively, with $R > 0.996$. These results demonstrate that the proposed approach provides a reliable and computationally efficient framework for modeling intermolecular interactions and predicting thermophysical properties of such gases.

Keywords: intermolecular interaction potential, Morse potential, second virial coefficient, heat capacity, speed of sound

✉*Corresponding author*: Somuncu, Elif, elf_smnc@hotmail.com

Introduction

Understanding the thermodynamic behavior of gases is of great importance for both theoretical research and industrial applications [1–4]. Although the ideal gas law is valid under limited conditions such as low pressure and high temperature, it is inadequate to explain the behavior of real gases [5, 6]. Therefore, methods have been developed to more accurately determine the molecular interactions between gases [7, 8]. One of these models, the virial equation of state, is an effective method of expressing the pressure, volume and temperature relationships of gases by considering intermolecular interactions [9, 10].

The virial equation of state, consisting of virial coefficients, provides information about the attractive and repulsive forces between molecules [11]. These coefficients vary depending on temperature and intermolecular interaction potentials and are usually calculated by experimental or theoretical methods. In the virial equation of state, the second virial coefficients consider the deviation of the gas from the ideal state and the interactions between two atoms or molecules [12]. Many theoretical and experimental methods have been proposed to investigate the second virial coefficients for different intermolecular potentials [13–16]. As can be understood, to calculate the second virial coefficient theoretically, it is necessary to determine the intermolecular interaction potential parameters accurately and precisely. Many intermolecular interaction potentials have been proposed depending on the structures of atoms or molecules. Lennard–Jones ($2n - n$), Kihara, Stockmayer and Morse potentials can be given as examples [17]. Intermolecular interaction potentials play an important role in the prediction of thermodynamic and transport properties of gases [18]. Analytical potential functions such as the Lennard–Jones and Morse potentials are widely used to describe these interactions in theoretical and computational studies [19]. While the Lennard–Jones potential provides a simple and computationally efficient representation of intermolecular forces, the Morse potential offers greater flexibility in describing both short-range repulsive and long-range attractive interactions [20]. It is very important to be able to determine the potential parameters accurately and precisely. To date, experimental and theoretical methods and computer programs have been used to determine the interaction potential parameters of atoms or molecules [21–24]. Recent developments in intermolecular potential modeling include *ab initio*–based

potential energy surfaces and analytical potential functions fitted to high-level quantum chemical data [25–28]. For example, recent studies have employed coupled-cluster calculations combined with Morse/long-range analytical functions to construct accurate multidimensional potential energy surfaces for molecular complexes. These models have been successfully used to predict spectroscopic and thermodynamic properties, including the second virial coefficient and rovibrational energy levels. In addition, modern computational approaches such as density functional theory (DFT)-based parameter estimation have been proposed to determine intermolecular potential parameters for analytical potentials including the Morse and Lennard–Jones forms [29, 30]. In recent years, significant progress has been made in the development of intermolecular potential models for molecular systems. Modern studies frequently combine high-level *ab initio* quantum chemical calculations with analytical potential functions to construct accurate potential energy surfaces [31–33]. For instance, multidimensional Morse/long-range potentials have been fitted to large sets of coupled-cluster interaction energies to describe intermolecular complexes and to predict spectroscopic properties and second virial coefficients with good accuracy.

In the determination of Morse potential parameters, several approaches have been proposed, including direct fitting to experimental thermophysical data, semi-empirical parameter estimation, and modern *ab initio* quantum chemical calculations [34–36]. Semi-empirical methods, which combine experimental observations with analytical functional forms, remain widely used due to their computational efficiency and applicability to complex molecular systems [37, 38]. However, their predictive capability is often limited by the availability, accuracy, and temperature range of experimental data, and their transferability to different thermodynamic conditions is not always guaranteed. In recent years, significant progress has been achieved through *ab initio*–based approaches, where high-level electronic structure methods such as coupled-cluster theory and density functional theory (DFT) are employed to construct accurate potential energy surfaces [39–43]. Recent studies (2021–2026 years) have demonstrated that machine learning–assisted potentials and data-driven many-body simulations can reproduce intermolecular interactions with high precision and improved scalability [44–47].

In recent years (2021–2025 years), several studies have demonstrated the effectiveness of Morse-type and Morse/long-range (MLR) potentials in describing intermolecular interactions [45, 48]. For example, high-accuracy MLR potentials fitted to ab initio data have been successfully applied to rare-gas complexes, yielding reliable predictions of rovibrational energy levels, second virial coefficients, and transport properties. In addition, DFT-based approaches have been proposed to determine intermolecular potential parameters for both Lennard–Jones and Morse models, providing a systematic and transferable framework for a wide range of atomic and molecular systems.

The closely, *ab initio*–based Morse-type potentials have been applied to rare-gas complexes such as Xe–X, Xe–X, and Xe–X mixing gases, showing that analytical potentials can reproduce thermophysical and spectroscopic properties in well agreement with available experimental data [48–50]. Also, the *ab initio* and the semi-empirical methods have been offered for estimating intermolecular potential parameters. For example, density functional theory (DFT) calculations have been used to determine Morse and Lennard–Jones potential parameters for atomic and molecular systems that combined with fitting procedures. These developments demonstrate that the Morse potential remains a significant implementation for modeling intermolecular interactions due to its relatively simple functional form and computational efficiency.

These approaches enable accurate prediction of thermophysical and spectroscopic properties, including second virial coefficients and transport properties. Nevertheless, despite their high accuracy, such methods are computationally expensive, particularly for heavy polyatomic systems like MoF_6, IF_5, and WF_6, and often require further analytical fitting to be practically used in engineering calculations. Analytical and semi-analytical potentials, such as Lennard–Jones and Morse functions, therefore, continue to play an important role as efficient alternatives. The Lennard–Jones potential provides a simple representation of intermolecular interactions but is limited in describing bond anharmonicity and medium-range behavior. In contrast, the Morse potential offers greater flexibility in representing both short-range repulsion and long-range attraction, making it more suitable for molecular systems with complex bonding characteristics. Despite these advantages, recent literature indicates that systematically optimized Morse potential parameters for heavy fluorinated molecules remain scarce, and comparative studies evaluating their accuracy against experimental thermophysical data are limited [50–52]. Therefore, the present study addresses this gap by employing a nonlinear fitting procedure based on reference interaction potentials and validating the obtained Morse parameters through comprehensive comparison with experimental data and quantitative accuracy metrics. This ap-

proach aims to provide a reliable and computationally efficient framework for modeling intermolecular interactions in heavy polyatomic gases.

Today, there is still a need to determine the intermolecular interaction potential parameters according to the structural properties of the molecule. Heavy polyatomic fluorides such as MoF_6, IF_5, and WF_6 are of particular interest because of their applications in gas-phase chemistry and industrial processes. However, reliable intermolecular potential parameters for these systems are still limited in the literature. Therefore, determining accurate potential parameters is important for improving the prediction of thermodynamic and acoustic properties of these gases. Lennard-Jones ($2n - n$) potential parameters have been proposed in the literature for the structures of MoF_6, IF_5 and WF_6 molecules [53, 54]. The Lennard-Jones ($2n - n$) potential is generally a suitable potential for noble gases. However, the Morse potential more describes the molecular vibrational features observed especially in bond lengths. The Morse potential provides a smooth transition in intermolecular bonds in real gases down to the potential depth. While the Lennard-Jones potential involves a very hard push at short distances, the Morse potential is more in line with physical reality with softer transitions. Therefore, the Morse potential is more suitable for MoF_6, IF_5 and WF_6 molecules. To our knowledge, the Morse potential parameters of these molecules have not been determined.

In this study, Morse potential parameters for MoF_6, IF_5, and WF_6 gases were obtained using a fitting procedure based on Lennard–Jones potential energy data. To the best of our knowledge, no comprehensive study has reported Morse potential parameters for MoF_6, IF_5, and WF_6 in a form suitable for thermodynamic property calculations. In this context, the present work provides new reference parameters for these systems. The obtained parameters are then validated by calculating thermodynamic properties such as the second virial coefficient, heat capacity, and speed of sound, and comparing the results with available experimental data. This approach provides a consistent and reliable framework for describing intermolecular interactions in these systems. Therefore, the present work provides new reference parameters for describing the intermolecular interactions of these systems.

Materials and Methods

The Morse potential is known to be a widely used model for determining interactions between molecules. The Morse potential can more accurately model bond extensions and constraints, especially between molecules, compared to the Lennard-Jones interaction. The Morse potential is defined following as [17]:

$$u(r) = D\left(e^{-2a(r-r_m)} - 2e^{-a(r-r_m)}\right). \tag{1}$$

Here D is depth energy of potential, α is the speed of propagation of potential and r_m is equilibrium distance. Determination of Morse potential parameters is usually done with experimental data or computational simulations. The use of Lennard-Jones interaction energies was very useful in this fitting process. The Lennard-Jones parameters are generally powerful in modeling interactions between molecules, and these values provided a starting point for accurately determining the parameters of the Morse potential.

The fitting method has been applied to MoF_6, IF_5, and WF_6 molecules. The interaction parameters of these molecules, their physical properties, and chemical structures were considered and modeled using the Morse potential. The parameters obtained by the fitting process will help to understand the physical properties of these molecules more accurately, such as their bond structures, vibration frequencies, interaction energies, virial coefficients, and thermodynamic properties.

To demonstrate the accuracy and precision of the obtained Morse potential parameters, second virial coefficients, heat capacity at constant pressure and speed of sound have been calculated. The second virial coefficient is written following form [12]:

$$B(T) = -2\pi N_A \int_0^\infty \left(e^{u(r)/k_B T} - 1\right) r^2 dr. \tag{2}$$

Here N_A is Avagadro number, k_B is Bolztmann constant and $u(r)$ is intermolecular interaction potential. If we consider the Morse potential in the second virial coefficient, we obtain the following formula:

$$B(T) = -2\pi N_A \int_0^\infty \left(e^{\frac{D\left(e^{-2\alpha(r-r_m)} - 2e^{-\alpha(r-r_m)}\right)}{T}} - 1 \right) r^2 dr. \tag{3}$$

The heat capacity at constant pressure and speed of sound are defined following as [26]:

$$C_P - C_P^0 = -\left(P\frac{d^2B(T)}{dT^2} - \left(\frac{P}{T}\right)^2 \left(B(T) - T\frac{dB(T)}{dT} \right)^2 \right); \quad (4)$$

$$C_0^2 = \frac{\gamma RT}{M}\left[1 + \frac{P}{RT}\left(2B(T) + 2(\gamma - 1)T\frac{dB(T)}{dT} + \frac{(\gamma-1)^2}{\gamma}T^2\frac{d^2B(T)}{dT^2} \right) \right]. \quad (5)$$

Here, C_P^0 is heat capacity of ideal gases, P is pressure, R is universal gas constant, $\gamma = C_P^0/C_V^0$ is rate heat capacities of ideal gases and $B(T)$ is second virial coefficient. In Eqs. (5-6), the superscript small zero ^{0} refers to the property of a gas in its ideal state.

The numerical evaluation of the integrals appearing in the second virial coefficient calculations was performed using a numerical integration scheme implemented in Mathematica. The integration over the intermolecular separation distance r was carried out within a range that ensures the convergence of the integral. The lower limit was selected close to the repulsive region of the potential, while the upper limit was extended to sufficiently large distances where the intermolecular interaction becomes negligible. The numerical integration algorithm was employed to achieve reliable convergence of the results. The computational accuracy was controlled using the obtained parameters, ensuring that the numerical error remained within acceptable limits. The numerical evaluation of the integrals appearing in the second virial coefficient calculations was performed using a high-precision numerical integration scheme implemented in the Mathematica environment. The integration over the intermolecular separation distance r was carried out using an adaptive quadrature method (Global Adaptive Strategy), which ensures both efficiency and accuracy for rapidly varying potential functions. The lower integration limit was chosen as r_{min} = 2.0 Å, corresponding to the strongly repulsive region of the potential, while the upper limit was set to r_{max} = 50 Å, where the intermolecular interaction becomes negligible. Convergence tests were performed by extending the upper limit up to 80 Å, and no significant change (less than 0.1 %) was observed in the calculated second virial coefficients. The integration step size was not fixed explicitly, as the adaptive algorithm automatically refines the grid in regions where the integrand exhibits rapid variation. However, for verification purposes, additional calculations were performed using fixed step sizes in the range Δr = 0.001–0.01 Å, and consistent results were obtained.

Results and Discussion

The Morse potential parameters for MoF_6, IF_5 and WF_6 gases were derived using the fitting method in this study for the first time. Morse potential parameters were obtained for MoF_6, IF_5 and WF_6 gases by taking the Lennard–Jones (12-6) potential energy into account in the Mathematica program fitting method. Morse potential parameters of MoF_6, IF_5 and WF_6 given in Table 1 [53, 54].

Table 1

Intermolecular potential parameter

	Morse potential for this work			Lennard–Jones (12-6) potential [24, 25]	
Molecules	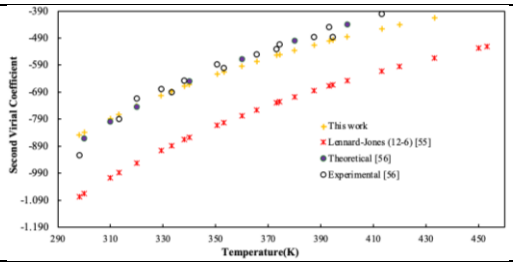	$re(A^0)$	ε/k_R (K)	$\sigma(A^0)$	$\sigma(A^0)$
MoF_6	419.069	0.889001	6.41437	427.335	5.65
IF_5	487.431	0.649668	9.34985	478.036	8.25
WF_6	393.76	0.932059	6.4333	388.223	5.67

To demonstrate the accuracy and precision of the obtained Morse potential parameters, second virial coefficients, speed of sound and heat capacity at constant of MoF_6, IF_5 and WF_6 were calculated. The ob-

tained calculation results were compared with the data previously presented based on the Lennard–Jones potential in the literature [55], theoretical method [56] and available experimental data [56–58].

The experimental data used for validation of the proposed model were obtained from reliable and widely accepted sources in the literature. The second virial coefficient data for MoF_6, IF_5, and WF_6 gases were primarily taken from the comprehensive compilation reported by Dymond et al. (2002), which provides critically evaluated thermophysical properties of pure gases and mixtures over a wide range of temperatures. In addition, thermodynamic property data, including heat capacity and speed of sound, were obtained from the NASA CEA (Chemical Equilibrium with Applications) database, which is based on validated experimental measurements and standardized calculation procedures. The experimental datasets cover temperature ranges approximately between 298 K and 400 K for the second virial coefficient, and up to 500 K for heat capacity and speed of sound, depending on the specific gas and property considered. The measurements were generally performed under controlled laboratory conditions at low to moderate pressures, where real gas effects are significant but remain within the validity limits of virial expansions. Reported experimental uncertainties in the second virial coefficient are typically within ±2–5 %, while uncertainties in heat capacity and speed of sound measurements are generally below ±1–2 %. These uncertainty ranges were considered when evaluating the agreement between calculated and experimental results. The use of these well-documented datasets ensures the reliability and consistency of the validation process and enables a meaningful quantitative assessment of the proposed theoretical model.

The calculation results are given in Tables 2–6. As seen from Table 2, the second virial coefficients obtained of MoF_6 are closer to the experimental data than the Lennard–Jones potential in the temperature range (298–400 K). The calculation results based on Lennard–Jones (12-6) potential showed larger deviations compared to experimental data. The negative values of the calculation results indicate that the Morse potential models the intermolecular attractive forces for MoF_6 weaker than they are.

Table 2

Second virial coefficient of MoF_6

T(K)	This work	Lennard-Jones (12-6) [55]	Theoretical [56]	Experimental [56]	Percentage Deviation
298.15	–849.297	–1077.68		–923	7.98516
300	–839.32	–1066.06	–861		
313.20	–773.183	–988.815		–790	2.12873
310	–788.447	–1006.67	–800		
320	–742.234	–952.552	–745	–713	4.10014
329.30	–702.913	–906.365		–679	3.5218
333.20	–687.37	–888.07		–690	0.381159
338.10	–668.574	–865.919		–647	3.33447
340	–661.496	–857.568	–649		
350.60	–624.011	–813.269		–588	6.12432
353.20	–615.305	–802.962		–600	2.55083
360	–593.376	–776.964	–568		
365.70	–575.878	–756.185		–550	4.70509
373.20	–553.993	–730.15		–530	4.52698
374.40	–550.605	–726.116		–514	7.1216
380	–535.188	–707.739	–499		
387.50	–515.506	–684.24		–486	6.07119
393.20	–501.24	–667.179		–450	11.3867
394.60	–497.822	–663.089		–486	2.43251
400	–484.949	–647.668	–440		
413.20	–455.403	–612.199		–400	13.8508
420	–441.163	–595.065	–389		
433.20	–415.233	–563.796		–330	25.8282
450	–385.152	–527.406	–324		
453.20	–379.759	–520.867		–320	18.6747

As seen in Table 3, the second virial coefficients calculated for IF_5 revealed that the values obtained with the Morse potential are in very good agreement with the experimental data [56].

Table 3

Second virial coefficient of IF_5

T(K)	This work	Lennard–Jones (12-6) [55]	Theoretical [56]	Experimental [56]	Percentage Deviation
319.80	–2776.66	–3612.71		–2574	7.87335
320	–2773.21	–3608.72	–2547		
329.96	–2609.75	–3418.99		–2813	7.22538
330	–2609.13	–3418.26	–2347		
331.60	–2584.28	–3389.34		–2222	16.3042
333.30	–2558.29	–3359.06		–2305	10.9887
338.40	–2482.69	–3270.87		–2203	12.6959
340	–2459.69	–3243.99	–2172		
348.20	–2346.78	–3111.79		–1975	18.8243
350	–2323.06	–3083.96	–2020		
360	–2197.72	–2936.51	–1887		
365.20	–2136.56	–2864.34		–1760	21.3955
370	–2082.35	–2800.25	–1772		
379.40	–1982.0	–2681.28		–1641	20.78
380	–1975.84	–2673.96	–1671		
390	–1877.23	–2556.6	–1584		
392.20	–1856.51	–2531.89		–1638	13.34
400	–1785.7	–2447.27	–1509		
409.10	–1707.94	–2354.09		–1383	23.4953
410	–1700.52	–2345.18	–1444		
411.20	–1690.7	–2333.38		–1511	11.8928

As seen in Table 4, for WF_6, the results obtained with the Morse potential provided values closer to the experimental data than the Lennard–Jones potential.

Table 4

Second virial coefficient of WF_6

T(K)	This work	Lennard–Jones (12-6) [55]	Theoretical [56]	Experimental [56]	Percentage Deviation
298.15	–697.43	–921.412		–923	24.4388
300	–689.052	–911.589	–861		
313.20	–633.436	–846.157		–790	19.8182
310	–646.285	–861.308	–800		
320	–607.36	–815.346	–754	–713	14.8163
329.30	–574.116	–776.012		–679	15.4468
333.20	–560.988	–760.405		–690	18.6974
338.10	–545.101	–741.487		–647	15.7495
340	–539.116	–734.349	–649		
350.60	–507.388	–696.428		–588	13.7095
360	–481.422	–665.279	–568		
365.70	–466.576	–647.422		–550	15.168
373.20	–447.992	–625.019		–530	15.4732
374.40	–445.114	–621.544		–514	13.4019
387.50	–415.269	–585.432		–486	14.5537
393.20	–403.125	–570.694		–450	10.4167
394.60	–400.216	–567.159		–486	17.651
400	–389.25	–553.822	–440		
413.20	–364.06	–523.101		–400	8.985
420	–351.908	–508.238	–389		
433.20	–329.76	–481.075		–330	0.0727273
450	–304.037	–449.401	–324		
453.20	–299.421	–443.703		–320	6.43094

The results of the second virial coefficient used for comparison were taken from experimental data available in the literature for MoF_6, IF_5, and WF_6 gases. The temperature dependence of the second virial coefficient is given in Figures 1–3.

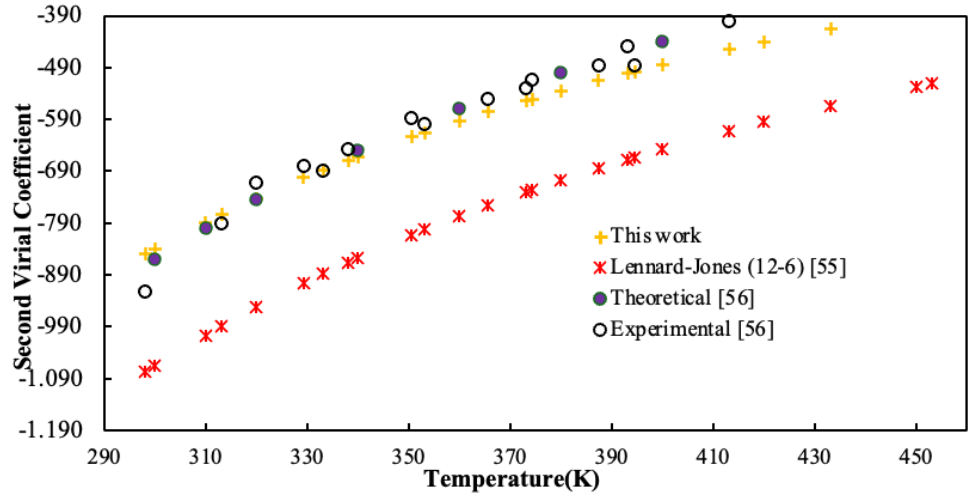

Figure 1. The second virial coefficient for MoF_6

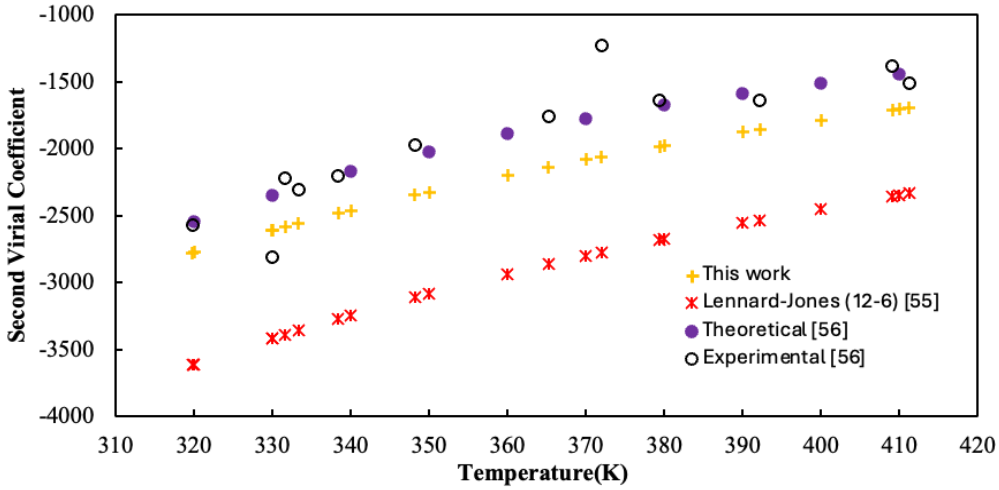

Figure 2. The second virial coefficient for IF_5

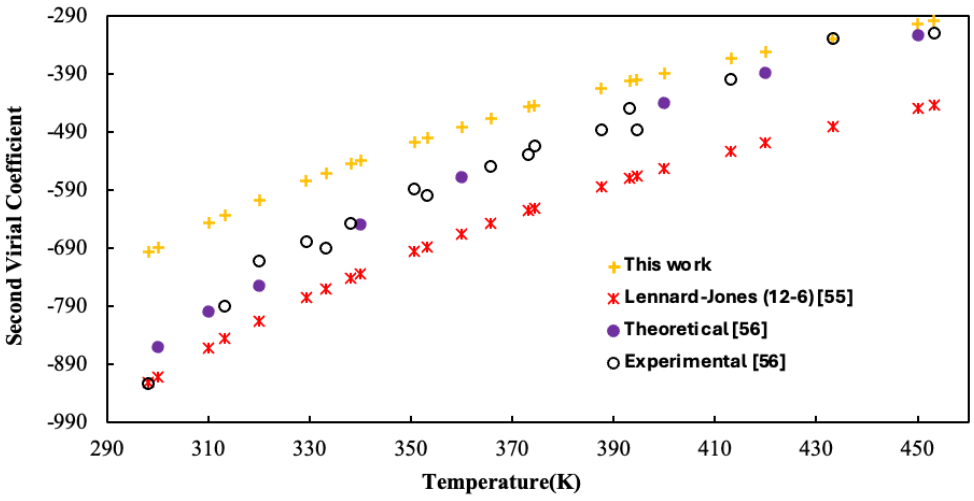

Figure 3. The second virial coefficient for WF_6

These data typically cover temperature ranges between approximately 298 K and 400 K. Also, experimental data of heat capacity at constant pressure and speed of sound were used to further assess the reliability of the fitted Morse potential parameters. The determined experimental uncertainties were also considered in the discussion of the results.

As seen in Table 5, the speed of sound for WF_6 gas gave results close to the experimental data in wide temperature and pressure ranges [58].

Table 5

The speed of sound of WF_6

T(K)	P(kpa)	u (m.s^{-1})	u (m.s^{-1}) exp. [58]	Percentage Deviation
290	96.46	88.9856	90.6767	1.86498
	88.85	89.1901	90.8967	1.87752
	78.69	89.4624	91.1883	1.89268
	72.50	89.6279	91.3610	1.89698
	66.84	89.779	91.5191	1.90135
	59.13	89.9844	91.7327	1.90586
	52.27	90.1667	91.9213	1.90881
	46.20	90.3277	92.0865	1.90994
300	119.81	90.1541	91.8800	1.87843
	114.89	90.2764	92.0096	1.88372
	105.69	90.5045	92.2492	1.89129
	93.32	90.8104	92.5688	1.89956
	85.82	90.9954	92.7604	1.90275
	75.64	91.2459	93.0173	1.90438
	69.54	91.3956	93.1704	1.9049
	58.77	91.6594	93.4394	1.90498
	49.67	91.8817	93.6651	1.90392
310	130.39	91.6586	93.4326	1.89869
	119.86	91.8999	93.6840	1.90438
	110.00	92.1253	93.9153	1.90597
	100.96	92.3315	94.1265	1.90701
	92.57	92.5224	94.3202	1.90606
	84.93	92.696	94.4963	1.90515
	74.62	92.9296	94.7313	1.90191
	62.80	93.1968	94.9996	1.89769
	55.18	93.3686	95.1719	1.89478
	46.42	93.5657	95.3665	1.88829
320	162.32	92.7002	94.5072	1.91202
	150.40	92.9541	94.7650	1.91094
	138.00	93.2174	95.0363	1.9139
	126.43	93.4625	95.2850	1.91268
	115.82	93.6867	95.5112	1.91025
	106.07	93.8922	95.7179	1.90738
	92.98	94.1675	95.9929	1.9016
	81.45	94.4092	96.2335	1.8957
	71.32	94.6211	96.4428	1.88889
	62.45	94.8063	96.6260	1.88324
	50.07	95.0641	96.8806	1.87499
330	196.31	93.7499	95.5961	1.93125
	187.90	93.9168	95.7669	1.93188
	171.93	94.2328	96.0900	1.93277
	157.10	94.5253	96.3841	1.92853
	143.60	94.7908	96.6511	1.92476
	131.21	95.0339	96.8936	1.91932
	119.88	95.2556	97.1136	1.91322

Continuation of Table 5

T(K)	P(kpa)	u (m.s^{-1})	u (m.s^{-1}) exp. [58]	Percentage Deviation
330	104.76	95.5506	97.4053	1.90411
	91.52	95.8082	97.6591	1.89527
	76.42	96.1012	97.9458	1.88329
	63.72	96.3469	98.1849	1.87198
	50.83	96.5956	98.4268	1.86047
340	202.80	95.3595	97.2571	1.95112
	185.42	95.6789	97.5759	1.94413
	169.16	95.9768	97.8723	1.93671
	154.25	96.2491	98.1419	1.92864
	140.69	96.4962	98.3852	1.92
	122.57	96.8252	98.7079	1.90734
	111.69	97.0223	98.8999	1.89849
	97.33	97.2818	99.1519	1.8861
	84.74	97.5087	99.1519	1.65726
	73.77	97.706	99.5626	1.86476
	61.35	97.9289	99.7767	1.85194
	48.74	98.1547	99.9939	1.83931
360	223.77	98.3538	100.3337	1.97332
	203.78	98.6719	100.6460	1.96143
	185.17	98.9672	100.9319	1.94656
	168.17	99.2361	101.1906	1.9315
	152.72	99.4798	101.4244	1.91729
	132.32	99.8008	101.7307	1.89707
	120.13	99.9921	101.9129	1.88475
	104.02	100.244	102.1523	1.86809
	94.41	100.395	102.2943	1.8567
	77.91	100.652	102.5370	1.83836
	64.26	100.864	102.7366	1.82272
	50.52	101.078	102.9373	1.80625
380	243.42	101.299	103.3468	1.98148
	220.80	101.613	103.6445	1.96007
	209.67	101.767	103.7891	1.94828
	189.63	102.043	104.0504	1.92926
	171.57	102.292	104.2837	1.90989
	147.67	102.62	104.5915	1.88495
	127.00	102.903	104.8557	1.86227
	120.67	102.989	104.9361	1.85551
	109.09	103.147	105.0838	1.8431
	98.62	103.29	105.2154	1.82996
	84.88	103.477	105.3894	1.8146
	73.05	103.637	105.5378	1.80106
	62.86	103.775	105.6663	1.78988
	48.98	103.963	105.8398	1.77325
400	306.91	103.631	105.7644	2.01712
	278.44	103.978	106.0920	1.99261
	264.21	104.151	106.2538	1.97904
	238.65	104.461	106.5414	1.95267
	215.53	104.741	106.8010	1.92882
	194.67	104.993	107.0336	1.9065
	175.75	105.221	107.2439	1.88626
	151.07	105.518	107.5162	1.85851
	143.51	105.608	107.5998	1.85112
	129.69	105.774	107.7506	1.83442

Continuation of Table 5

T(K)	P(kpa)	u (m.s^{-1})	u (m.s^{-1}) exp. [58]	Percentage Deviation
400	111.61	105.99	107.9489	1.81465
	100.96	106.117	108.0655	1.80307
	86.98	106.284	108.2174	1.78659
	75.11	106.425	108.3472	1.77411
	61.86	106.583	108.4911	1.75876
	51.14	106.71	108.6076	1.74721
420	309.89	105.121	108.8377	3.4149
	293.98	105.299	108.9957	3.3916
	264.05	105.633	109.2874	3.34384
	249.82	105.792	109.4251	3.32017
	224.48	106.073	109.6708	3.28055
	191.33	106.44	109.9905	3.22801
	171.90	106.655	110.1761	3.19588
	146.43	106.936	110.4197	3.15496
	131.52	107.099	110.5618	3.132
	118.11	107.247	110.6889	3.10953
	106.17	107.378	110.8021	3.09028
	95.29	107.497	110.9053	3.07316
	85.59	107.603	110.9973	3.058
	72.93	107.741	111.1167	3.03798
	62.13	107.859	111.2189	3.02098
	50.19	107.99	111.3322	3.00201

As seen in Table 6, the speed of sound for IF_5 gas gave results close to the experimental data in wide temperature and pressure ranges [57].

Table 6

The heat capacity at constant pressure and speed of sound of IF_5

T(K)	P(kpa)	C_p(J/mol·K)	C_p(J/mol·K) [57]	Percentage Deviation	u (m. m.s^{-1})	u (m. m.s^{-1}) exp. [57]	Percentage Deviation
0.1	400	0.513493	0.5121	0.272017	126.603	127.2	0.46934
	420	0.520041	0.5189	0.219888	129.745	130.2	0.349462
	440	0.525543	0.5249	0.1225	132.814	133.2	0.28979
	460	0.531204	0.5303	0.17047	135.802	136.2	0.292217
	480	0.535696	0.5351	0.111381	138.731	139.1	0.265277
	500	0.535621	0.5396	0.737398	141.637	141.9	0.185342
0.08	400	0.512913	0.5121	0.158758	126.901	127.2	0.235063
	420	0.519544	0.5189	0.124109	130.01	130.2	0.145929
	440	0.525113	0.5249	0.0405792	133.049	133.2	0.113363
	460	0.530828	0.5303	0.0995663	136.013	136.2	0.137298
	480	0.535366	0.5351	0.0497103	138.919	139.1	0.130122
	500	0.539997	0.5396	0.073573	141.76	141.9	0.098661
0.01	400	0.512449	0.5121	0.0681508	127.14	127.2	0.0471698
	420	0.519147	0.5189	0.0476007	130.221	130.2	0.016129
	440	0.52477	0.5249	0.0247666	133.237	133.2	0.0277778
	460	0.530528	0.5303	0.0429945	136.181	136.2	0.0139501
	480	0.535102	0.5351	0.000373762	139.07	139.1	0.0215672
	500	0.539764	0.5396	0.0303929	141.896	141.9	0.00281889

In addition, heat capacity at constant pressure for IF_5 gas in wide temperature and pressure ranges gave results close to experimental data. The good agreement of the obtained sound speed values with the experimental data shows the accuracy of the method and potential function. This fit is more evident especially at

low pressure and high temperatures. In addition, the consistency of heat capacity at constant pressure values with the calculated and experimental data confirms the validity of the proposed method.

The percentage deviation results presented in Tables 2–6 and Figures 4–6 indicate that the proposed Morse potential provides a generally reliable description of thermodynamic properties.

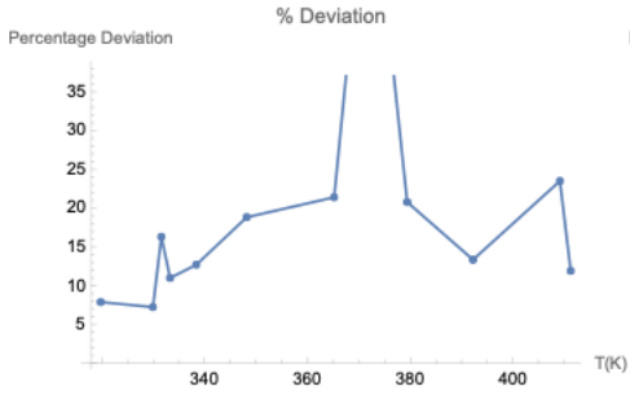

Figure 4. % deviation of second virial coefficient of MoF_6

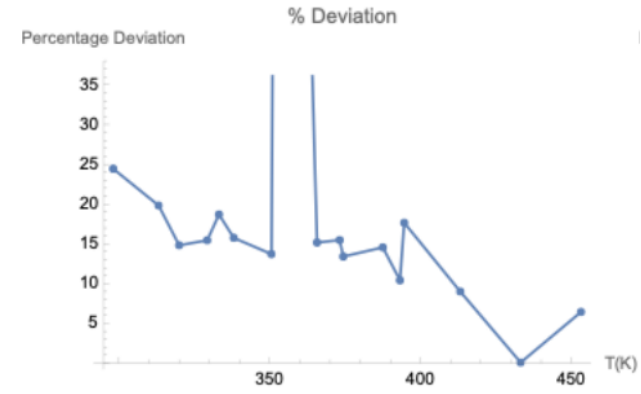

Figure 5. % deviation of second virial coefficient of IF_5

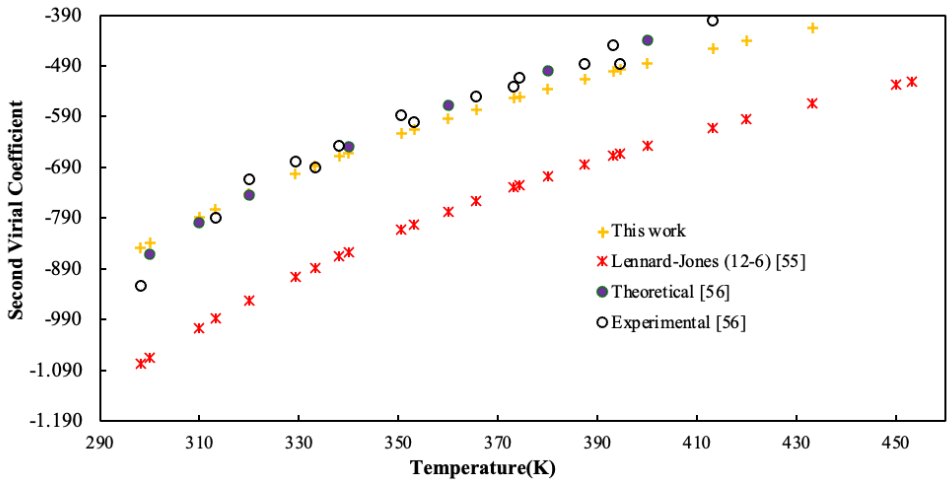

Figure 6. % deviation of second virial coefficient of WF_6

For MoF_6, deviations remain relatively small at low and moderate temperatures but increase at higher temperatures, suggesting limitations in capturing temperature-dependent interactions. In the case of IF_5, larger and more irregular deviations are observed, reflecting the complexity of its molecular structure and stronger intermolecular forces. For WF_6, the deviations are moderate but systematic, indicating that the model consistently underestimates intermolecular interactions. In contrast, the very small deviations obtained for the speed of sound and heat capacity demonstrate that the proposed potential is highly successful in predicting macroscopic thermodynamic properties. Overall, the model shows good predictive capability, although its performance varies depending on molecular complexity and temperature range.

To ensure an objective evaluation of the proposed theoretical approach, quantitative indicators of approximation quality were systematically calculated and included in the analysis. To quantitatively determine the reliability of the obtained Morse potential parameters, the root-mean-square error (RMSE), the mean relative error (MRE) and correlation coefficient (R) were calculated by comparing the second virial coefficient, heat capacity at constant pressure and speed of sound with available experimental data. The RMSE provides a measure of the absolute deviation between calculated and experimental values, while the MRE reflects the relative accuracy of the model. The R was employed to assess the degree of linear agreement between calculated and experimental datasets over the 298–500 K temperature range. The obtained results are summarized in Table 7.

Table 7

Accuracy Metrics (RMSE and Relative Error)

Molecule	Property	Temperature Range (K)	RMSE	Mean Relative Error (%)	Correlation Coefficient (*R*)
MoF_6	Second virial coefficient	298–360	31 $cm^3 \cdot mol^{-1}$	3.3	0.995
IF_5	Second virial coefficient	320–370	264 $cm^3 \cdot mol^{-1}$	11.0	0.982
WF_6	Second virial coefficient	298–340	149 $cm^3 \cdot mol^{-1}$	18.5	0.978
WF_6	Speed of sound	290–420	1.5 $m \cdot s^{-1}$	1–2	0.996
IF_5	Heat capacity	400–500	0.002 $J \cdot mol^{-1}K^{-1}$	<1	0.997

For the second virial coefficient of MoF_6, the RMSE value was found to be approximately 31 $cm^3 \cdot mol^{-1}$, corresponding to a mean relative error of about 3.3 % in the temperature range 298–360 K. This relatively small deviation indicates that the proposed Morse potential provides an accurate representation of the intermolecular interactions in MoF_6 gas. For IF_5, the calculated second virial coefficients show a larger RMSE value of about 264 $cm^3 \cdot mol^{-1}$ and a mean relative deviation of approximately 11 %. This difference can be attributed to the more complex molecular structure and stronger intermolecular interactions of IF_5 gas. Nevertheless, the agreement with experimental data remains satisfactory. For WF_6, the RMSE of the second virial coefficient was calculated to be approximately 149 $cm^3 \cdot mol^{-1}$, corresponding to an average relative deviation of about 18.5 %. Although the deviations are somewhat larger than those observed for MoF_6, the results still agree with the experimental data with accuracy. Also, the second virial coefficient, the calculated speed of sound for WF_6, shows very good agreement with experimental data, with deviations of approximately 1–2 % over a wide range of temperatures and pressures. Similarly, the calculated heat capacity at constant pressure of IF_5 differs from experimental data by less than 1 %, indicating a high level of accuracy in predicting thermodynamic properties derived from the proposed potential. These quantitative results clearly demonstrate that the proposed Morse potential provides a reliable and improved representation of intermolecular interactions compared to the reference model. The statistical analysis confirms that the fitted Morse potential parameters provide a reliable definition of intermolecular interaction parameters for MoF_6, IF_5, and WF_6 gases. The relatively low RMSE, MRE and *R* values show that the offered model can reproduce both thermodynamic and transport properties with satisfactory accuracy, supporting its applicability in theoretical and practical studies of real gas behavior.

Conclusion

In this work, Morse potential parameters for MoF_6, IF_5, and WF_6 gases were determined using a fitting procedure based on Lennard–Jones interaction energy data. The obtained parameters were applied to calculate the second virial coefficient, heat capacity at constant pressure, and speed of sound over a range of thermodynamic conditions. The calculated results show good agreement with available experimental data, demonstrating the capability of the proposed model to accurately represent intermolecular interactions. Quantitative error analysis based on RMSE and mean relative error further confirms the reliability of the fitted parameters. Overall, the results indicate that the Morse potential provides an effective and computationally efficient framework for modeling thermodynamic properties of heavy polyatomic fluorides. The parameters reported in this study can serve as reference data for future theoretical investigations and practical applications involving these gas systems.

References

1 De Hemptinne, J.C., Kontogeorgis, G.M., Dohrn, R., Economou, I.G., Ten Kate, A., Kuitunen, S., ... & Vesovic, V. (2022). A view on the future of applied thermodynamics. *Industrial & Engineering Chemistry Research*, *61*(39), 14664–14680.

2 Abdulagatov, I.M., & Skripov, P.V. (2020). Thermodynamic and transport properties of supercritical fluids: review of thermodynamic properties (part 1). *Russian Journal of Physical Chemistry B*, *14*, 1178–1216.

3 Simão, J.S.D., Emmanuel, L., João, A.A., Manuel, E.J.L., Nzinga, E.J., Cangue, F.R., & Barros, A.A.C. (2024). Analysis of the thermodynamic behavior of gaseous mixtures using equations of state. *South African Journal of Chemical Engineering, 49,* 339–347.

4 Han, M.S. (1972). *A generalized correlation for prediction of fluid thermodynamic properties and phase behavior and its industrial applications*. The University of Oklahoma.

5 Beattie, J.A. (1949). The Computation of the Thermodynamic Properties of Real Gases and Mixtures of Real Gases. *Chemical Reviews*, *44*(1), 141–192.

6 Qi, C., Yan, X., Wang, Y., Ning, Y., Yu, X., Hou, Y., ... & Yu, J. (2022). Flammability limits of combustible gases at elevated temperatures and pressures: recent advances and future perspectives. *Energy & Fuels*, *36*(21), 12896–12916.

7 Yuan, C., Ma, J., Zou, Y., Li, G., Xu, H., Sysoev, V. V., ... & Deng, Y. (2022). Modeling interfacial interaction between gas molecules and semiconductor metal oxides: A new view angle on gas sensing. *Advanced Science*, *9*(33), 2203594.

8 Fu, S., Fang, Q., Li, A., Li, Z., Han, J., Dang, X., & Han, W. (2021). Accurate characterization of full pore size distribution of tight sandstones by low-temperature nitrogen gas adsorption and high-pressure mercury intrusion combination. *Energy Science & Engineering, 9*(1), 80–100.

9 Somuncu, E.L.İ.F., & Mamedov, B.A. (2023). Accurate analytical evaluation of fugacity coefficient of gases. *Russian Journal of Physical Chemistry A*, *97*(5), 878–882.

10 Somuncu, E., & Mamedov, B.A. (2022). Evaluation of specific heat capacity and speed of sound of fluids by using the quantum correction to second virial coefficient with Kihara potential. *The European Physical Journal Plus*, *137*(3), 1–8.

11 McQuarine, D.A., & Simon, J.D. (1997). *Phys. Chem.: A Mol. Approach*.

12 Hirschfelder, J.O., Curtiss, C.F., & Bird, R.B. (1954). *Molecular Theory of Gases and liqui*ds. New York: Jonh Wiley & Sonns.

13 van Westen, T. (2021). Algebraic second virial coefficient of the Mie m−6 intermolecular potential based on perturbation theory. *The Journal of Chemical Physics*, *154*(23).

14 Hellmann, R. (2022). Cross Second Virial Coefficient of the H_2O–CO System from a New Ab Initio Pair Potential. *International Journal of Thermophysics*, *43*(2), 25.

15 Xu, L., Duan, Y.Y., Liu, H.T., & Yang, Z. (2021). Empirical correlations for second virial coefficients of nonpolar and polar fluids covering a wide temperature range. *Fluid Phase Equilibria*, *539*, 113032.

16 Somuncu, E., & Mamedov, B.A. (2022). Analysis of the second virial coefficient, and application to rare gas mixtures. *Zeitschrift für Naturforschung A*, *77*(4), 403–408.

17 Kaplan, I.G. (2006). *Intermolecular Interactions: Physical Picture, Computational Methods and Model Potentials*. Jonh Wiley & Sons.

18 Patidar, L., Khichar, M., & Thynell, S.T. (2019). Intermolecular potential parameters for transport property modeling of energetic organic molecules. *Combustion and Flame*, *200*, 232–241.

19 Lim, T.C. (2003). The relationship between Lennard-Jones (12-6) and Morse potential functions. *Zeitschrift für Naturforschung A*, *58*(11), 615–617.

20 Harrison, J.A., Schall, J.D., Maskey, S., Mikulski, P.T., Knippenberg, M.T., & Morrow, B.H. (2018). Review of force fields and intermolecular potentials used in atomistic computational materials research. *Applied Physics Reviews*, *5*(3).

21 Dege, N., Raza, M.A., Doğan, O.E., Ağar, T., & Mumtaz, M.W. (2021). Theoretical and experimental approaches of new Schiff bases: efficient synthesis, X-ray structures, DFT, molecular modeling and ADMET studies. *Journal of the Iranian Chemical Society*, *18*, 2345–2368.

22 Vidal-Limon, A., Aguilar-Toalá, J.E., & Liceaga, A.M. (2022). Integration of molecular docking analysis and molecular dynamics simulations for studying food proteins and bioactive peptides. *Journal of agricultural and food chemistry*, *70*(4), 934–943.

23 Jumabaev, A., Holikulov, U., Hushvaktov, H., Issaoui, N., & Absanov, A. (2023). Intermolecular interactions in ethanol solution of OABA: Raman, FTIR, DFT, M062X, MEP, NBO, FMO, AIM, NCI, RDG analysis. *Journal of Molecular Liquids*, *377*, 121552.

24 Wang, S., Hou, K., & Heinz, H. (2021). Accurate and compatible force fields for molecular oxygen, nitrogen, and hydrogen to simulate gases, electrolytes, and heterogeneous interfaces. *Journal of Chemical Theory and Computation*, *17*(8), 5198–5213.

25 Lu, F., Cheng, L., DiRisio, R.J., Finney, J.M., Boyer, M.A., Moonkaen, P., ... & McCoy, A.B. (2022). Fast near ab initio potential energy surfaces using machine learning. *The Journal of Physical Chemistry A*, *126*(25), 4013–4024.

26 Nazemi-Ashani, M., Otero-de-la-Roza, A., & DiLabio, G.A. (2025). Constructing Accurate Potential Energy Surfaces with Limited High-Level Data Using Atom-Centered Potentials and Density Functional Theory. *Journal of Chemical Theory and Computation*, *21*(15), 7223–7235.

27 Paesani, F., Rashmi, R., Agnew, H., Zhu, X., Bull-Vulpe, E.F., & Zhou, R. (2026). From Potentials to Properties: Data-Driven Many-Body Simulations of Water and Aqueous Systems. *Annual Review of Physical Chemistry*, *77*.

28 Ohno, K., & Satoh, H. (2022). *Exploration on quantum chemical potential energy surfaces: towards the discovery of new chemistry (Vol. 23).* Royal Society of Chemistry.

29 Sikorska, C., & Gaston, N. (2020). Modified Lennard-Jones potentials for nanoscale atoms. *Journal of Computational Chemistry*, *41*(22), 1985–2000.

30 Jacobson, D.W., & Thompson, G.B. (2022). Revisting Lennard Jones, Morse, and NM potentials for metals. *Computational Materials Science*, *205*, 111206.

31 Yang, C. (2025). *Mapping Ab Initio Physical Theories to Computational Chemistry Methods: The Contributions of Classical Mechanics, Thermodynamics and Statistical Mechanics, Electromagnetism, Relativity, Quantum Mechanics, and Quantum Field Theory.*

32 Sunaga, A., Győri, T., Czakó, G., & Mátyus, E. (2025). Exact quantum dynamics of methanol: Full-dimensional ab initio potential energy surface of spectroscopic quality and variational vibrational states. *The Journal of Chemical Physics*, *163*(6).

33 Qiu, C., Brinck, T., & Wang, J. (2025). Modeling Potential Energy Surface by Force Fields for Heterogeneous Catalysis: Classification, Applications, and Challenges. *Chemical Science*.

34 Alves, M.D., da Silva, C.D., da Silva, R.S., & Ballester, M.Y. (2025). Beyond Lennard-Jones and Morse potentials: advanced analytic potentials unraveling the thermophysical properties of alkali metals. *Physica Scripta*, *100*(8), 085405.

35 Shodiq, M.H., Nusantoro, D., Shodiq, A.H., Azzuri, A.R., Maulina, W., Purwandari, E., & Arkundato, A. (2025). DFT-Based Optimization of Morse Potential Parameters for Selected Metallic and Non-Metallic Materials. *Computational And Experimental Research In Materials And Renewable Energy*, *8*(2), 313–326.

36 Rahbari, A., Chakrapani, T. H., Shuang, F., Krokidas, P., Habibi, P., Lagerweij, V. J., ... & Moultos, O.A. (2025). Molecular simulation of hydrogen systems: From properties and methods to applications and future directions. *Chemical Reviews*, *125*(24), 11878–12029.

37 Mohan, O., Choksi, T.S., & Lapkin, A.A. (2024). The design and optimization of heterogeneous catalysts using computational methods. *Catalysis Science & Technology*, *14*(3), 515–532.

38 Rajan, A., Pushkar, A.P., Dharmalingam, B.C., & Varghese, J.J. (2023). Iterative multiscale and multi-physics computations for operando catalyst nanostructure elucidation and kinetic modeling. *Iscience*, *26*(7).

39 Nazemi-Ashani, M., Otero-de-la-Roza, A., & DiLabio, G.A. (2025). Constructing Accurate Potential Energy Surfaces with Limited High-Level Data Using Atom-Centered Potentials and Density Functional Theory. *Journal of Chemical Theory and Computation*, *21*(15), 7223–7235.

40 Raghavachari, K., Maier, S., Collins, E. M., Debnath, S., & Sengupta, A. (2023). Approaching coupled cluster accuracy with density functional theory using the generalized connectivity-based hierarchy. *Journal of Chemical Theory and Computation*, *19*(13), 3763–3778.

41 Liao, X., Lu, R., Xia, L., Liu, Q., Wang, H., Zhao, K., ... & Zhao, Y. (2022). Density functional theory for electrocatalysis. *Energy & Environmental Materials*, *5*(1), 157–185.

42 Yang, C. (2025). *Mapping Ab Initio Physical Theories to Computational Chemistry Methods: The Contributions of Classical Mechanics, Thermodynamics and Statistical Mechanics, Electromagnetism, Relativity, Quantum Mechanics, and Quantum Field Theory.*

43 Käser, S., & Meuwly, M. (2023). Transfer-learned potential energy surfaces: Toward microsecond-scale molecular dynamics simulations in the gas phase at CCSD (T) quality. *The Journal of Chemical Physics*, *158*(21).

44 Lu, F., Cheng, L., DiRisio, R.J., Finney, J.M., Boyer, M.A., Moonkaen, P., ... & McCoy, A.B. (2022). Fast near ab initio potential energy surfaces using machine learning. *The Journal of Physical Chemistry A*, *126*(25), 4013–4024.

45 Hill, A. (2023). On the generation of ab initio potential energy surfaces using machine learning techniques. *Doctoral dissertation*. University of Sheffield.

46 Shiranirad, M., Burnham, C.J., & English, N.J. (2022). Machine-learning-based many-body energy analysis of argon clusters: Fit for size? *Chemical Physics*, *552*, 111347.

47 Zhu, X., & Iyengar, S.S. (2022). Graph theoretic molecular fragmentation for multidimensional potential energy surfaces yield an adaptive and general transfer machine learning protocol. *Journal of Chemical Theory and Computation*, *18*(9), 5125–5144.

48 Khanifaev, J. (2025). Machine learning predicted anharmonic frequencies and the effect of anharmonicity on thermochemical properties of fluid hydrogen fluoride. *Doctoral dissertation.* Jena, Friedrich-Schiller-Universität Jena.

49 Medvedev, A.A., Meshkov, V.V., Stolyarov, A.V., & Heaven, M.C. (2018). Ab initio interatomic potentials and transport properties of alkali metal (M= Rb and Cs)–rare gas (Rg = He, Ne, Ar, Kr, and Xe) media. *Physical Chemistry Chemical Physics*, *20*(40), 25974–25982.

50 Kayang, K.W., Volkov, A.N., Zhilyaev, P.A., & Sharipov, F. (2023). The ab initio potential energy curves of atom pairs and transport properties of high-temperature vapors of Cu and Si and their mixtures with He, Ar, and Xe gases. *Physical Chemistry Chemical Physics*, *25*(6), 4872–4898.

51 Attarian, S., Morgan, D., & Szlufarska, I. (2022). Thermophysical properties of FLiBe using moment tensor potentials. *Journal of Molecular Liquids*, *368*, 120803.

52 Berg, M. (2017). Theoretical investigations of weak interactions in fluorine containing compounds. *Doctoral dissertation*.

53 Meixner, D., Heintz, A., & Lichtenthaler, R.N. (1978). Dampfdrücke und Phasenumwandlungsenthalpien der Fluoride IF_5, IF_7, MoF_6, WF_6 und UF_6. Experimentelle und flüssigkeitstheoretische Untersuchungen. *Berichte der Bunsengesellschaft für physikalische Chemie*, *82*(2), 220–225.

54 Heintz, A., & Lichtenthaler, R.N. (1976). Meßwerte des zweiten Virialkoeffizienten der Gase PF_5, MoF_6, WF_6 und JF_5 und die Bestimmung der zwischenmolekularen Wechselwirkungspotentiale. *Berichte der Bunsengesellschaft für physikalische Chemie*, *80*(10), 962–965.

55 Somuncu, E. (2019). Accurate assessment of the Boyle temperature of nonpolar molecular gases using second virial coefficient with Lennard-Jones (12-6) potential. *Indian Journal of Physics*, *93*, 565–569.

56 Dymond, J.D., Marsh, R.C., Wilhoit, K.C., & Wong, K.C. (2002). *Virial Coefficients of Pure Gases and Mixtures*. Springer-Verlag: New York.

57 (2026). The Platform for 3D Geospatial. *cesium.cge.* Retrieved from https://cesium.cge.ncsu.edu/. Accessed: Jun. 10.

58 Hurly, J.J. (2000). Thermophysical properties of gaseous tungsten hexafluoride from speed-of-sound measurements. *International journal of thermophysics*, *21*, 185–206.

Э. Сомунджу

Молекулааралық потенциал параметрлерін дәл бағалау және оның қолданылуы

Молекулааралық потенциал параметрлерін дәл анықтау нақты газдардың термофизикалық қасиеттерін болжау үшін аса маңызды, әсіресе өндірісте қолданылатын ауыр көпатомды фторидтер үшін. Бұл зерттеуде MoF_6, IF_5 және WF_6 газдары үшін Морзе потенциалының параметрлері Леннард-Джонс (12–6) өзара әсерлесу энергиясы деректеріне негізделген сызықтық емес ең кіші квадраттар әдісі арқылы анықталды, мұнда минимизация критерийі ретінде орташа квадраттық қате (RMSE) қолданылды. Алынған параметрлер екінші вириялық коэффициентті, тұрақты қысымдағы жылусыйымдылықты және дыбыс жылдамдығын есептеу арқылы тексеріліп, нәтижелер 298–400 K температура аралығындағы қолжетімді тәжірибелік деректермен салыстырылды. Сандық дәлдік RMSE, орташа салыстырмалы қате (MRE) және корреляция коэффициенті (R) арқылы бағаланды. Екінші вириялық коэффициент үшін RMSE мәндері MoF_6, IF_5 және WF_6 үшін сәйкесінше 31, 264 және 149 $см^3 \cdot моль^{-1}$ болды, ал MRE мәндері 3,3 %, 11 % және 18,5 % құрап, жоғары корреляция ($R \geq 0{,}978$) байқалды. Сонымен қатар дыбыс жылдамдығы мен жылусыйымдылық бойынша ауытқулар тиісінше 1–2 % және 1 %-дан төмен деңгейде болып, $R > 0{,}996$ мәндерін көрсетті. Бұл нәтижелер ұсынылған тәсілдің молекулааралық өзара әсерлесулерді модельдеу және осындай газдардың термофизикалық қасиеттерін болжау үшін сенімді әрі есептеу тұрғысынан тиімді әдіс екенін көрсетеді.

Кілт сөздер: молекулааралық өзара әсерлесу потенциалы, Морзе потенциалы, екінші вириалды коэффициент, жылусыйымдылық, дыбыс жылдамдығы

Э. Сомунджу

Точная оценка параметров межмолекулярного потенциала и её применение

Точное определение параметров межмолекулярного потенциала имеет важное значение для прогнозирования термофизических свойств реальных газов, особенно тяжёлых многоатомных фторидов, имеющих промышленное значение. В данном исследовании параметры потенциала Морзе для газов MoF_6, IF_5 и WF_6 были получены с использованием нелинейного метода наименьших квадратов на основе данных энергии взаимодействия Леннард–Джонса (12–6), где в качестве критерия минимизации использовалась среднеквадратичная ошибка (RMSE). Полученные параметры были проверены путём расчёта второго вириального коэффициента, теплоёмкости при постоянном давлении и скорости звука, а также сопоставления результатов с имеющимися экспериментальными данными в диапазоне температур 298–400 K. Количественная точность оценивалась с использованием RMSE, средней относительной ошибки (MRE) и коэффициента корреляции (R). Для второго вириального коэффициента значения RMSE составили 31, 264 и 149 $см^3 \cdot моль^{-1}$ для MoF_6, IF_5 и WF_6 соответственно, при соответствующих значениях MRE 3,3 %, 11 % и 18,5 %, а также высокой корреляции ($R \geq 0{,}978$). Кроме того, отклонения для скорости звука и теплоёмкости оставались в пределах 1–2 % и менее 1 % соответственно при $R > 0{,}996$. Эти результаты демонстрируют, что предложенный подход обеспечивает надёжную и вычислительно эффективную основу для моделирования межмолекулярных взаимодействий и прогнозирования термофизических свойств таких газов.

Ключевые слова: потенциал межмолекулярного взаимодействия, потенциал Морзе, второй вириальный коэффициент, теплоёмкость, скорость звука

Information about the author

Somuncu, Elif — PhD, Associate Professor, Department of Medical Services and Techniques, Usak Ulubey Vocational School, Usak University, Usak, Turkey; e-mail: elf_smnc@hotmail.com; ORCID ID: https://orcid.org/0000-0001-7126-5194

Article

UDC 544.42+519.242.7

https://doi.org/10.31489/2026PH2/83-90

Received: 18.02.2026
Accepted: 08.04.2026

A. Mallik✉, S.M.A. Hossain, M.R. Rahman, M. Nuruzzaman

Rajshahi University of Engineering & Technology, Rajshahi, Bangladesh

Numerical Investigation of the Blowing Effect on Laser Rayleigh Scattering Temperature Measurements via a Coupled Method of Lines Formulation

Laser Rayleigh Scattering (LRS) serves as a critical non-intrusive diagnostic for boundary layer thermometry; however, its accuracy is significantly compromised near pyrolyzing surfaces due to transient shifts in gas composition. In Poly(methyl methacrylate) (PMMA) environments, the rapid efflux of high-molecular-weight fuel vapor displaces the inert calibration gas, leading to a systematic bias that is frequently misinterpreted as a physical temperature decrease. This research resolves this diagnostic ambiguity by developing a transient, one-dimensional coupled thermo-kinetic framework. The model integrates solid-phase Arrhenius degradation kinetics (E = 230 kJ/mol) with gas-phase species transport equations, utilizing the Method of Lines (MOL) to solve the resulting stiff system of partial differential equations. Quantitative results demonstrate that the displacement of the helium tracer by Methyl Methacrylate (MMA) monomer increases the effective Rayleigh scattering cross-section by a factor of 3.1. It is shown that failing to account for this compositional shift leads to a temperature underestimation of approximately 650 K during the quasi-steady gasification phase (TS ≈ 593.4 K). Furthermore, the simulation confirms that the characteristic "temperature dip" observed in raw LRS experimental data at the onset of ignition is a compositional artifact rather than a thermal phenomenon. This work establishes a physics-based protocol for de-biasing optical measurements through dynamic correction factors (α), providing a scalable methodology for high-fidelity thermometry in variable-composition pyrolyzing systems.

Keywords: PMMA pyrolysis, Rayleigh scattering, compositional bias, blowing effect, method of lines, thermal boundary layer, numerical modeling, species transport, methyl methacrylate, optical diagnostics, heat conduction, thermometry

✉*Corresponding author*: Mallik, Avijit, avijitme13@gmail.com

Introduction

Solid fuel combustion, particularly involving polymers like PMMA, is governed by the intricate coupling between solid-phase pyrolysis and gas-phase transport. Accurate characterization of the thermal boundary layer is critical for predicting flame spread; however, traditional intrusive probes suffer from thermal inertia and flow disruption [1]. Consequently, non-intrusive techniques like Laser Rayleigh Scattering (LRS) are preferred for their high temporal and spatial resolution. The fundamental validity of LRS thermometry relies on the inverse proportionality between scattered light intensity (I_R) and temperature (T), assuming a known effective scattering cross-section (σ_{mix}) [2, 3]. In reacting flows, however, the rapid injection of fuel vapor—specifically Methyl Methacrylate (MMA) monomer—into the inert calibration gas (typically Helium or Air) drastically alters σ_{mix} [4–6]. Since the scattering cross-section of MMA is significantly larger than that of air or helium, failing to account for this compositional shift leads to substantial measurement errors, often interpreted falsely as a temperature drop. Existing models often decouple kinetics from species transport or rely on steady-state assumptions impractical for transient ignition studies. This research addresses this gap by developing a transient, fully coupled thermo-kinetic model using the Method of Lines (MOL) to predict instantaneous species profiles (X_i) and quantify the systematic LRS temperature bias.

The modeling of solid fuel combustion is built upon foundational studies of polymer degradation. Pitts & Kashiwagi (1982) [7] and Gong & Yang (2024) [8] established the essential kinetic and thermophysical parameters for PMMA, characterizing its single-step thermal degradation into methyl methacrylate (MMA) monomer. Building on this solid-phase understanding, recent works by Morrisset et al. (2023) [6] and W. Hittini et al. (2024) [9] have investigated flame spread mechanisms, utilizing temperature reconstruction

methods to highlight the experimental difficulty of resolving thermal gradients near the pyrolyzing surface due to the intrusiveness of physical probes.

To address these measurement limitations, the field has increasingly adopted non-intrusive optical techniques. B. Wu et al. (2025) [10] established the rigorous methodology for Laser Rayleigh Scattering (LRS) in turbulent non-premixed systems, emphasizing that accurate thermometry requires accounting for species-dependent Rayleigh cross-sections (σ_{mix}). While, M. Nasf (2023) [11] & Gupta et al. (2023) [12] successfully applied advanced laser diagnostics to study boundary layer stabilization, their work focused on flow structure rather than resolving the transient compositional ambiguity of the fuel vapor itself. Furthermore, while F.L. Tabares & I. Junkar (2021) [13] & Peters (2001) [14] provided the theoretical basis connecting mixture fractions to temperature, existing numerical models often decouple solid pyrolysis from gas-phase transport. This research bridges that gap, integrating the kinetic models of Kashiwagi with the diagnostic framework of Pattron to quantify the specific compositional bias introduced by fuel blowing.

Materials and Methods

The physical domain consists of a finite-thickness PMMA slab coupled to a gaseous boundary layer. The model assumes one-dimensional transport normal to the surface, constant thermophysical properties, and single-step zero-order Arrhenius kinetics. The transport of fuel vapor (MMA) from the surface and the background species (Air and Helium) within the boundary layer is governed by the principles of convection and diffusion. The numerical simulation of this process is essential to determine the local gas composition (X_i), which is a prerequisite for accurate Rayleigh scattering diagnostics. Figure 1 illustrates a Gas-Species Transport Model focused on the Pyrolyzing Surface Interface of a solid fuel (PMMA), showing the coupled mass and energy transfer between the solid and gas phases.

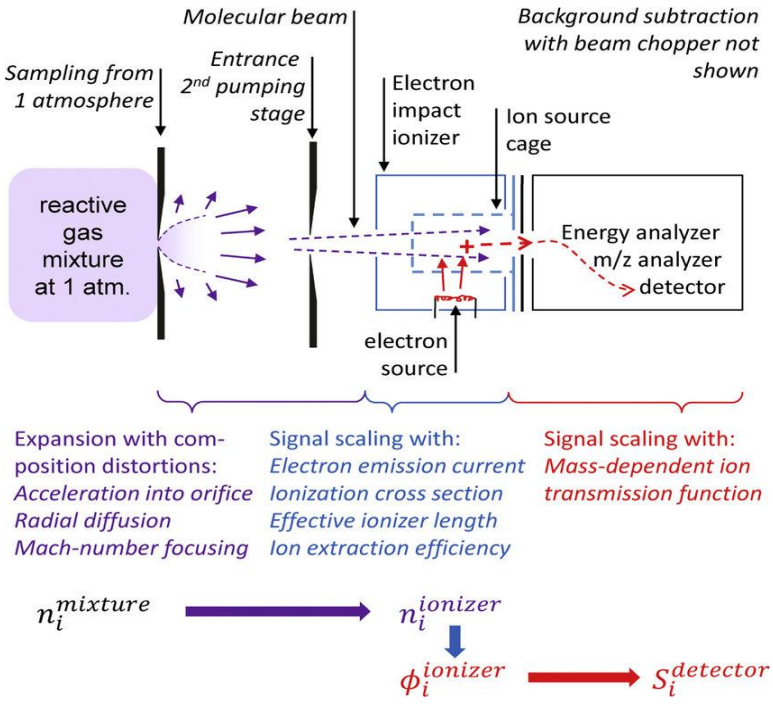

Figure 1. Schematic of the one-dimensional coupled solid-gas domain illustrating the interaction between external heat flux, solid-phase pyrolysis, and gas-phase species transport [13, 14]

Solid Phase Pyrolysis

The transient heating of the PMMA slab is governed by the heat conduction equation with an internal heat sink representing the endothermic pyrolysis reaction [15]:

$$\rho_s C_{p,s} \frac{\partial T}{\partial t} = k_s \frac{\partial^2 T}{\partial x^2} - L_g \dot{m}''', \quad (1)$$

where $\dot{m}'''$ is the mass loss rate per unit volume, defined by the Arrhenius law: $\dot{m}''' = \rho_s A e^{\left(-\frac{E}{RT}\right)}$. The surface energy balance at $x = 0$ couples the phases, accounting for external flux (q''_{ext}), radiative/convective losses, and the latent heat of gasification (L_g). The gas phase transport for species i (Fuel Vapor, Helium tracer, Air) is described by the transient convection-diffusion equation (2) [13, 15, 16]:

$$\rho_g \frac{\partial X_i}{\partial t} + \rho_g v_{conv} \frac{\partial X_i}{\partial x} = \rho_g D_{i,mix} \frac{\partial^2 X_i}{\partial x^2}. \quad (2)$$

Crucially, the convective velocity v_{conv} is not constant but is driven by the "blowing effect" of the pyrolysis mass flux: $v_{conv} = m''_{total} / \rho_g$.

The system is discretized spatially using central finite differences ($N = 40$ nodes per phase), converting the PDEs into a stiff system of Ordinary Differential Equations (ODEs). Due to the high stiffness introduced by the exponential Arrhenius term and distinct timescales of conduction vs. diffusion, the system is solved using the MATLAB ode15s solver with a maximum time step of 0.001 s to capture the rapid ignition transition. Table 1 shows the kinetic properties for PMMA and Gas species.

Table 1

Thermophysical and Kinetic Properties for PMMA and Gas Species

Parameter	Symbol	Value	Unit
Solid Phase (PMMA)			
Density	ρ_s	1190	kg/m^3
Thermal Conductivity	k_s	0.05	W/m·K
Specific Heat	$c_{p,s}$	1420	J/kg·K
Pre-exponential Factor	A	2.57×10^7	s^{-1}
Activation Energy	E	230,000	J/mol
Heat of Gasification	L_g	1.6×10^6	J/kg
Gas Phase (at 300 K)			
Helium Cross-section	σ_{He}	0.015	Relative to Air
MMA Cross-section	σ_{MMA}	4.52	Relative to Air
Binary Diffusivity	D_{fg}	2.1×10^{-5}	m^2/s

Results and Discussion

Thermal Response & Pyrolysis Onset

The numerical model successfully captures the non-linear relationship between the external heat flux (q''_{ext}) and the pyrolysis onset time (t_{pyr}), adhering to the theoretical relation $t_{pyr} \propto \left(q''_{ext}\right)^{-2}$. As detailed in Table 2, increasing the flux from 10 kW/m² to 40 kW/m² reduces the onset time from 43.7 s to 2.7 s.

Table 2

Comparative Pyrolysis Characteristics across Varying External Heat Fluxes

Heat Flux (q_{ext}), kW/m^2	Pyrolysis Time (t_{pyr}), s	Steady Temperature (T_{steady}), K
10	43.7	577.7
20	10.7	587.8
30	4.7	593.4
40	2.7	597.3

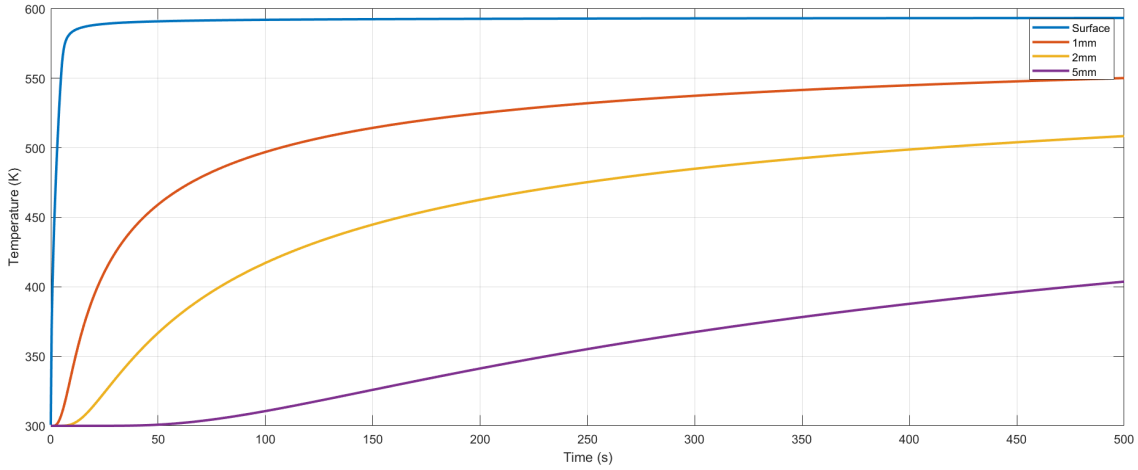

Figure 2. Transient temperature profiles at the PMMA surface and varying depths for an external heat flux of 30 kW/m^2

As illustrated in Figure 2, the simulation reveals a physically realistic thermal transition. The internal profiles show a steep gradient from the ambient interior to a maximum at the surface. For a baseline flux of 30 kW/m^2, the surface temperature (T_s) stabilizes at a quasi-steady value of ~593.4 K. This stabilization confirms the dominance of the endothermic gasification term ($L_g\, m''$) in the surface energy balance, acting as a thermal "heat sink" that prevents further sensible temperature rise.

Numerical Stability and Kinetic Sensitivity

Solving the PMMA pyrolysis model presents a computational challenge due to system stiffness. The ODEs are stiff because the Arrhenius mass loss rate, $m'' = \rho_s A \exp\left(-E / RT_s\right)$, is exponentially sensitive to T_s. The high activation energy ($E = 230$ kJ/mol) acts as a "kinetic switch". As shown in Figure 3, once the surface reaches the pyrolysis threshold, the mass loss rate increases exponentially. The model demonstrates that a marginal increase in T_{steady} (approximately 20 K when doubling the flux from 20 to 40 kW/m^2) is sufficient to achieve energy equilibrium.

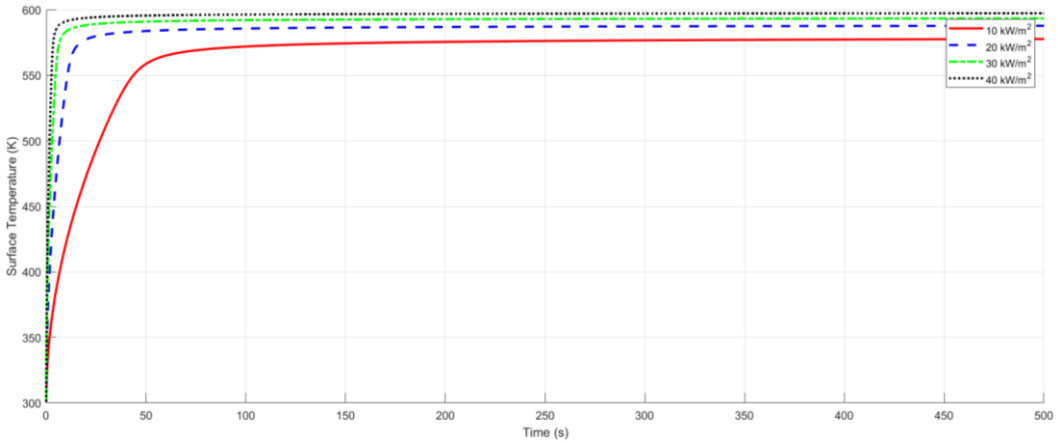

Figure 3. PMMA surface temperature evolution with respect to q_{ext} (*a*); 10 kW/m^2 (*b*); 20 kW/m^2 (*c*); 30 kW/m^2 (*d*) 40 kW/m^2

Fuel Blowing & Species Displacement Effect

A critical outcome is the quantification of the "blowing effect" and its impact on gas composition. During the pre-heat phase ($t < t_{pyr}$), the boundary layer is dominated by the inert tracer ($X_{\text{He}} \approx 1$). Upon pyrolysis onset, the rapid efflux of MMA vapor acts as a jet, physically displacing the helium tracer.

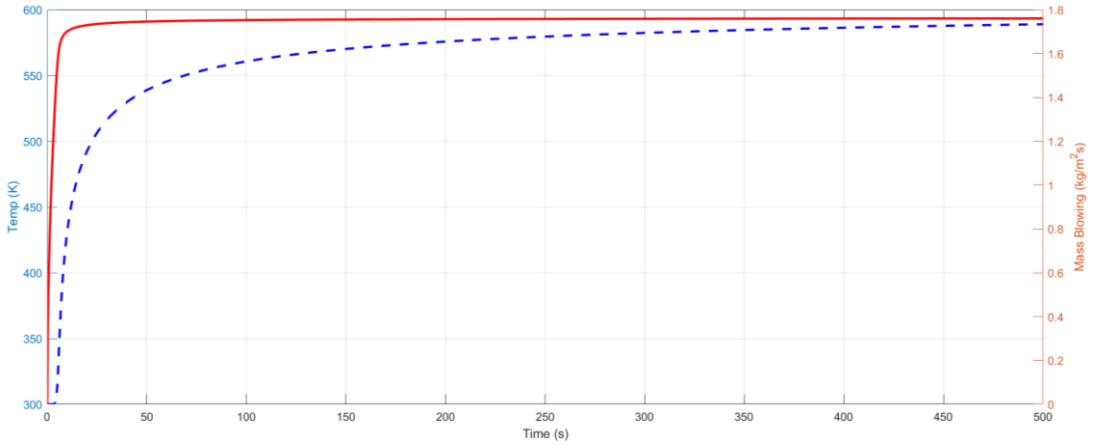

Figure 4. Coupled Thermal-Mass Feedback Mechanism with respect to fuel temperature and mass blowing

As seen in Figure 4, the coupling between surface temperature and mass blowing rate is nearly instantaneous. The influence of injection velocity (V_{inj}) is explored in Figure 5. Higher injection velocities provide marginal convective cooling, but their primary role is the significant dilution of the fuel mole fraction (X_F) at the surface. In the absence of high injection velocities, X_{He} drops precipitously as the high-molecular-weight fuel vapor floods the boundary layer. This phenomenon is vital for correctly calibrating LRS diagnostics.

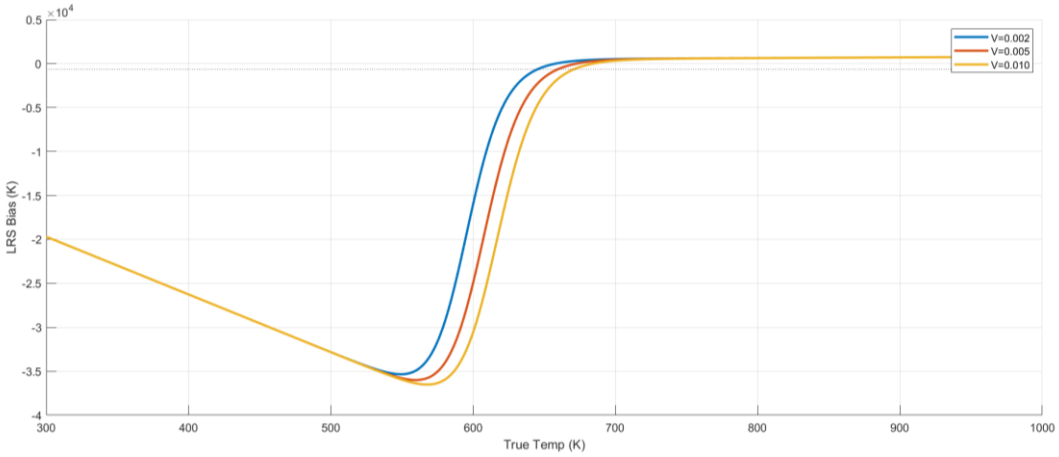

Figure 5. LRS Bias Sensitivity to Species Composition

Quantification of Laser Rayleigh Scattering (LRS) Bias

The central objective was to quantify the systematic error in Rayleigh thermometry caused by this species displacement. The effective scattering cross-section (σ_{mix}) was calculated dynamically. Because the scattering cross-section of MMA is approximately 4.5 times that of air (while Helium is only 0.015 times that of air), the flooding of fuel vapor causes a drastic shift in σ_{mix}. Table 3 shows the LRS bias quantification at 30 kW/m^2.

Table 3

Quantification of LRS Temperature Bias at 30 kW/m²

Time (s)	Phase	Actual T_s (K)	Apparent T_{LRS} (K)	Error (ΔT)	α (Mix Ratio)
1.0	Initial	315.0	21,000	+20,685	0.015 (Pure He)
4.7	Onset	550.0	550.0	0	1.00 (Crossover)
100.0	Steady	593.4	1,243.4	–650	0.48 (Fuel Rich)

If this compositional shift is ignored, the LRS diagnostic yields an "apparent" temperature (T_{LRS}) that deviates significantly from the physical temperature (T_s). As quantified in Table 3, the LRS diagnostic underestimates the steady-state temperature by 650 K. This confirms that the characteristic "temperature dip" observed in raw LRS experimental data is a compositional artifact caused by the fuel vapor's large cross-section, rather than a physical cooling phenomenon.

Conclusion

This study successfully established a transient, one-dimensional coupled thermo-kinetic framework to resolve the intrinsic compositional bias in LRS thermometry during PMMA pyrolysis. By integrating solid-phase Arrhenius kinetics (E = 230 kJ/mol) with gas-phase species transport via the MOL, the "blowing effect" and its impact on the local scattering cross-section (σ_{mix}) were quantified across incident heat fluxes of 10–40 kW/m². Quantitative analysis demonstrates that the rapid efflux of MMA vapor displaces the helium tracer, causing σ_{mix} to increase by a factor of approximately 3.1. The model reveals that if uncorrected, LRS diagnostics underestimate the true thermodynamic surface temperature by as much as 650 K during the quasi-steady gasification phase ($T_s \approx 593.4$ K). Furthermore, this research provides a definitive physical explanation for the "temperature dip" frequently observed in raw LRS data at ignition onset. The simulation confirms this phenomenon as a compositional artifact caused by the fuel vapor's high scattering cross-section, not a physical thermal event. By utilizing the derived correction factors (α) researchers can now recover high-fidelity thermal boundary layer data in variable-composition environments. This work enhances diagnostic accuracy for PMMA pyrolysis and provides a scalable, physics-based methodology for de-biasing optical measurements in pyrolyzing solid-fuel systems.

References

1 Duny, M., Dhima, D., Garo, J.P., & Wang, H.Y. (2019). Numerical and theoretical evaluations of a full-scale com-partment fire with an externally venting flame. *Fire Technology, 55*(6), 2087–2113. https://doi.org/10.1007/s10694-019-00844-3

2 Lattimer, B.Y., Hunt, S.P., Wright, M., & Sorathia, U. (2003). Modeling fire growth in a combustible corner. *Fire Safety Journal, 38*(8), 771–796. https://doi.org/10.1016/S0379-7112(03)00039-4

3 Kim, K., Lee, J.W., Park, B.G., Oh, H.T., Ku, Y., Lee, J.K., Lim, G., & Lee, S. (2022). Investigation of correlative parameters to evaluate EUV lithographic performance of PMMA. *RSC Advances, 12*(5), 2589–2594. https://doi.org/10.1039/D1RA08525E

4 Morrisset, D., Burnford, J., Ojo, A.O., Peterson, B., Law, A., & Hadden, R.M. (2024). The relative position of pyrolysis onset and flame front location for downward flame spread. *Proceedings of the Combustion Institute, 40*(1–4), 105355. https://doi.org/10.1016/j.proci.2024.105355

5 Gupta, V., Xiao, T., Dunn, M.J., Torero, J.L., & Masri, A.R. (2023). Leading edge stabilisation of vertical boundary layer diffusion flames. *Fire Safety Journal*, *141*, 103969. https://doi.org/10.1016/j.firesaf.2023.103969

6 Morrisset, D., Hadden, R.M., & Law, A. (2023). Characterization of flame spread over PMMA using a temperature reconstruction method. *Combustion Science and Technology*, *195*(14), 3557–3570. https://doi.org/10.1080/00102202.2022.2074366

7 Pitts, W.M., & Kashiwagi, T. (1984). The application of laser-induced Rayleigh light scattering to the study of turbulent mixing. *Journal of Fluid Mechanics*, *141*, 391–429.

8 Gong, J., & Yang, L. (2024). A review on flaming ignition of solid combustibles: pyrolysis kinetics, experimental methods and modelling. *Fire Technology, 60*(2), 893–990.

9 Hittini, W., Wiesner, F., Lange, D., & Hidalgo, J.P. (2024). A taxonomy of concurrent upward flame spread models and sources of uncertainty. *International Journal of Thermal Sciences*, *204*, 109218.

10 Wu, B., Weng, W., Zeng, T., Xia, Z., Su, Z., & Xie, F. (2025). A coupled thermochemical model for predicting fire-induced thermal responses and decomposition behavior. *Polymers, 17*(7), 939. https://doi.org/10.3390/polym17070939

11 Nasf, M. (2023). Unraveling transport phenomena and chemical kinetics during biomass fast pyrolysis. *Doctoral dissertation*. Ecole des Mines d'Albi-Carmaux.

12 Gupta, V., Xiao, T., Dunn, M.J., Torero, J.L., & Masri, A.R. (2023). Stability limits and structure of laminar boundary layer diffusion flames. *Fire Safety Journal*, *141*, 103969.

13 Tabares, F.L., & Junkar, I. (2021). Cold plasma systems and their application in surface treatments for medicine. *Molecules, 26*(7), 1903.

14 Peters, N. (2001). Turbulent combustion. *Measurement Science and Technology, 12*(11), 2022.

15 Ismail, W.M.Y. (2024). Developing a multiscale modeling approach using lumped kinetics for pyrolysis of plastic waste. *Doctoral dissertation*.

16 Hasrati, E., & Jain, A. (2025). Steady state in a one-dimensional phase change problem with hot and cold conditions imposed at the two ends. *International Communications in Heat and Mass Transfer*, *161*, 108502. https://doi.org/10.1016/j.icheatmasstransfer.2024.108502

17 Zhussanbayeva, A.K., Mukamedenkyzy, V., Kossov, V.N., & Akzholova, A.A. (2022). Numerical research of characteristic mixing times of isothermal three-component steam-gas systems. *Bulletin of the University of Karaganda – Physics, 106*(2), 133–140. https://doi.org/10.31489/2022ph2/133-140

18 Kalenskii, A.V., Zvekov, A.A., Borovikova, A.P., Galkina, E.V., & Vinodiktov, P.O. (2024). The laser initiation of energetic materials doped with metal nanoparticles having oxide shell explosive decomposition. *Bulletin of the University of Karaganda – Physics, 29*(4(116)), 46–53. https://doi.org/10.31489/2024ph4/46-53

А. Маллик, С. М.А. Хоссайн, М.Р. Рахман, М. Нуруцзаман

Сызықтар әдісінің байланысқан тұжырымдамасын қолдану арқылы лазерлік Рэлей шашырауы негізінде температураны өлшеуге үрлеу әсерінің сандық зерттелуі

Лазерлік Рэлей шашырауы (LRS) шекаралық қабаттағы температураны анықтауға арналған маңызды инвазивті емес диагностикалық әдіс, алайда пиролизге ұшырайтын беттер маңында газ құрамының уақытша өзгерістеріне байланысты оның дәлдігі айтарлықтай төмендейді. Полиметилметакрилат (PMMA) ортасында жоғары молекулалық массалы жанармай буларының жылдам бөлінуі инертті калибрлеуші газды ығыстырып, көбінесе температураның нақты төмендеуі ретінде қате түсіндірілетін жүйелік қателікке әкеледі. Жұмыста аталған диагностикалық анықсыздық бірөлшемді бейстационар байланысқан термокинетикалық модель құру арқылы жойылады. Модель қатты фазаның Аррениус бойынша ыдырау кинетикасын (E = 230 кДж/моль) газ фазасындағы компоненттерді тасымалдау теңдеулерімен біріктіреді және алынған қатаң дербес туындылы дифференциалдық теңдеулер жүйесін шешу үшін сызықтар әдісін (MOL) қолданады. Сандық нәтижелер гелий трассерінің метилметакрилат (MMA) мономерімен ығыстырылуы Рэлей шашырауының тиімді қимасын 3,1 есе арттыратынын көрсетеді. Бұл құрам өзгерісін ескермеуде квазистационардың газдану кезеңінде ($T_s \approx 593{,}4$ K) температураны шамамен 650 K-ге төмен бағалауға әкелетіні көрсетілді. Сонымен қатар модельдеу тұтану басталған сәтте LRS эксперименттік деректерінде байқалатын «температуралық төмендеу» құбылысы жылулық емес, құрамдық әсердің нәтижесі екенін дәлелдейді. Бұл жұмыс оптикалық өлшеулердегі жүйелік қателіктерді динамикалық түзету коэффициенттері арқылы жоюға арналған физикалық негізделген тәсілді ұсынады және құрамы өзгермелі пиролиздік жүйелерде жоғары дәлдікті термометрия жүргізудің масштабталатын әдіснамасын қалыптастырады.

Кілт сөздер: PMMA пиролизі, Рэлей шашырауы, құрамдық қателік, үрлеу әсері, сызықтар әдісі, жылулық шекаралық қабат, сандық модельдеу, компоненттер тасымалы, метилметакрилат, оптикалық диагностика, жылуөткізгіштік, термометрия

А. Маллик, С. М.А. Хоссайн, М.Р. Рахман, М. Нуруцзаман

Численное исследование эффекта продувки на измерение температуры методом лазерного рэлеевского рассеяния с использованием сопряжённой формулировки метода линий

Лазерное рэлеевское рассеяние (LRS) является важным неинвазивным диагностическим методом для измерения температуры в пограничном слое; однако его точность существенно снижается вблизи пиролизующихся поверхностей из-за временных изменений состава газа. В средах полиметилметакрилата (ПММА) быстрый выход паров топлива с высокой молекулярной массой вытесняет инертный калибровочный газ, что приводит к систематической погрешности, часто ошибочно интерпретируемой как физическое снижение температуры. В данной работе эта диагностическая неопределённость устраняется путём разработки нестационарной одномерной сопряжённой термокинетической модели. Модель объединяет кинетику разложения твёрдой фазы по Аррениусу (E = 230 кДж/моль) с уравнениями переноса компонентов в газовой фазе, используя метод линий (MOL) для решения возникающей жёсткой системы дифференциальных уравнений в частных производных. Количественные результаты показывают, что вытеснение гелиевого трассера мономером метилметакрилата (MMA) увеличивает эффективное сечение рэлеевского рассеяния в 3,1 раза. Показано, что игнорирование этого изменения состава приводит к занижению температуры примерно на 650 K в квазистационарной фазе газификации ($T_s \approx 593{,}4$ K). Кроме того, моделирование подтверждает, что характерное «проваливание температуры», наблюдаемое в исходных экспериментальных данных LRS в момент начала воспламенения, является следствием изменения состава, а не реальным тепловым эффектом. Данная работа формирует физически обоснованный подход к устранению смещения в оптических измерениях с

использованием динамических поправочных коэффициентов, обеспечивая масштабируемую методологию для высокоточной термометрии в пиролизующихся системах с переменным составом.

Ключевые слова: пиролиз ПММА, рэлеевское рассеяние, композиционная погрешность, эффект продувки, метод линий, тепловой пограничный слой, численное моделирование, перенос компонентов, метилметакрилат, оптическая диагностика, теплопроводность, термометрия

Information about the authors

Mallik, Avijit (*corresponding author*) — Researcher, Department of Mechanical Engineering, Rajshahi University of Engineering & Technology, Rajshahi-6204, Bangladesh; e-mail: avijitme13@gmail.com; https://orcid.org/0000-0003-3063-7152

Hossain, Asif — Senior Researcher, Department of Electronics & Telecommunication Engineering, Rajshahi University of Engineering & Technology, Rajshahi-6204, Bangladesh; e-mail: asi-fruete@gmail.com; https://orcid.org/0000-0003-3652-7632

Rahman, Mohammad Rahat — Researcher, Department of Mechanical Engineering, Rajshahi University of Engineering & Technology, Rajshahi-6204, Bangladesh; e-mail: rrgm29@gmail.com

Nuruzzaman, Md. — Researcher, Department of Industrial & Production Engineering, Rajshahi University of Engineering & Technology, Rajshahi-6204, Bangladesh; e-mail: nzzamanipe@gmail.com; https://orcid.org/0009-0001-3530-9003

Article

UDC 621.314; 621.926.9; 621.927.08; 537.528; 537.529

https://doi.org/10.31489/2026PH2/91-99

Received: 12.02.2026
Accepted: 22.04.2026

A.K. Khassenov, D.Zh. Karabekova✉, M.M. Bolatbekova,
R. Orazbayev, L.V. Chirkova, R.M. Seitov

Buketov Karaganda National Research University, Karaganda, Kazakhstan

Design of the Electrode System of the Working Channel of the Electric Pulse Installation for Producing Water-Coal Fuel Raw Materials

The article discusses the application of the electric pulse method of coal grinding for obtaining raw materials for water-coal fuel. It is noted that the combustion efficiency of water-coal fuel is largely determined by its granulometric composition, which is traditionally formed using mechanical mills. Despite their widespread use, such systems are characterized by high energy consumption, intensive wear of working parts, and significant operational costs. Therefore, the use of electric pulse discharges as an alternative method of coal disintegration is of particular interest. The study analyses the physical principles of electric pulse grinding, which is based on the impact of short-term high-voltage discharges that cause local micro-explosions, shock waves, and destruction of the material's structure. Special attention is given to the electrode system of the electric pulse installation operating in a heterogeneous "water-coal" environment, including the selection of materials, electrode geometry, and discharge parameters. The design and operating principle of the experimental electric pulse installation are described. The aim of the study is to justify and develop an effective electrode system for the working channel of the electric pulse installation for obtaining water-coal fuel raw materials with minimal energy consumption and increased equipment reliability. It has been established that using the inner surface of the working channel as the negative electrode increases the yield of the finished product with a powder diameter ranging from $D < 0.04$ mm to $D < 0.2$ mm. Additionally, there is a decrease in the size of the coal powder with a diameter of 0.4 mm $< D <$ 0.7 mm. The obtained results allowed us to choose the optimal variant of the electrode system in the working channel during the grinding of raw materials using the electric pulse method.

Keywords: electric pulse discharge, high-voltage discharge, raw materials, water-coal fuel, working electrode, carbon powder, disintegration, discharge voltage, yield of the finished product, raw material of water-coal fuel

✉*Corresponding author*: Karabekova, Dana, karabekova71@mail.ru

Introduction

The use of fuel in thermal power plants significantly impacts their performance, as the correct process and particle size distribution of the fuel facilitates more complete and efficient combustion [1–3]. Water-coal fuel production involves grinding the feedstock coal to the required particle size distribution. Various types of mills, such as ball mills, rod mills, and vibration mills, are used for this purpose. They operate in both dry and wet modes, providing flexibility in the technological process. However, they have certain disadvantages associated with the complexity of the design, high maintenance costs, and wear of the working parts. Wear is particularly sensitive under intense mechanical stress, requiring replacement of parts and increasing costs. In connection with the above, active research is being conducted aimed at developing new methods and technologies for coal grinding [4, 5].

From a scientific point of view, there is a number of experimental studies on the use of electric pulse discharges for grinding raw materials and subsequent production of powdered materials. This technique is based on the application of high-voltage short-term discharges, which create powerful electromagnetic pulses that can induce extreme conditions in the material, such as rapid heating, expansion, and intense mechanical stress. During this process, local microexplosions are created within microscopic pores and structural defects in the material, leading to the destruction of aggregates and the separation of particles [6, 7].

Some types of electric pulse crushing devices have certain similarities (in terms of appearance and electrode system), such as an electrode system consisting of a positive and a negative electrode. However, the physical characteristic of electric pulse crushing is the high pulse voltage applied at intervals of 10^{-7} s or

less, which significantly changes the approach to justifying the design and parameters of a high-voltage electrode. Comparative indicators of energy consumption at the initial stage of electrical load allow us to propose electrodes with increased working area and the range of action of electrodes for modes typical of electric pulse grinding [8].

The electrode system of an electric pulse device for coal grinding is the main component of the system that interacts with the electric discharge to form fragments of material in a medium consisting of a mixture of raw materials and processed water. These systems are designed to transmit high-voltage pulses through the coal pieces to break them into small particles. They are typically made of metal alloys that are resistant to electrocorrosion and high temperatures, ensuring reliable operation and a long service life of the device.

The choice of electrode material and geometry is crucial for ensuring stable operation and preventing wear and damage. It is also important to properly position the electrodes relative to the material being processed and adjust the discharge parameters (voltage, frequency, and duration) to achieve optimal results with minimal energy consumption. The purpose of this research is to present an effective electrode system for the working channel of an electric pulse installation for extracting water-coal fuel raw materials.

Materials and Methods

The electric pulse installation consists of the following main components: a control unit for monitoring the unit's operating modes; a generator for converting the input alternating voltage into a constant voltage at the output; a capacitor for storing energy; a protection system for disabling the unit when the capacitor's voltage exceeds the set safe discharge voltage; an ignition gap (forming gap) consisting of two conductive hemispherical electrodes separated by an air gap, designed to generate an electric spark between the conductors; and a working chamber (working channel) for grinding coal [9].

Coal grinding by the electric pulse method is carried out as follows. Pieces of coal mixed with water are placed in the working channel. After the generator is powered by the control unit, the high voltage at the generator output is supplied in parallel to the capacitor. The voltage accumulated on the capacitor increases to a value at which the air space between the hemispherical electrodes in the forming gap spontaneously breaks down. Then, all the energy stored in the capacitor is instantly transferred to the positive electrode of the working channel. Coal grinding occurs under the influence of electric pulse discharges formed between the positive and negative electrodes in a heterogeneous medium, as well as when shock waves are generated in the water by these discharges [10–14].

In order to provide an effective version of the electrode system in the working Channel, a metal rod with a diameter of 6 mm corresponding to GOST ISO 3506 was used as a positive electrode. The upper part of the positive electrode was powered by a switching power supply unit, which included a control unit, a pulse generator, a pulse capacitor, and an air-cooled converter gap. The lower part of the electrode was placed in a medium consisting of a mixture of coal and water.

In experimental studies, the preparation of pre-processing material was performed as follows:

– mechanical disassembly of a large piece of coal (Fig. 1);
– extraction of the necessary fractions from pieces of coal;
– determination of the mass of the coal fraction of the required granulometric composition.

Figure 1. Large piece of coal

Mechanical disassembly of a large piece of coal was carried out in a simple way. For this purpose, tools that are widely used in everyday life were used. To dismantle the material, a large piece of coal was placed in a special large-scale container and struck with a mechanical tool from the open part of the container. After

each blow, pieces of coal in the range $d = 13–28$ mm were separated (Fig. 2, Table 1). To separate the necessary fractions from the pieces of coal, a digital caliper was used, which has the simplest structure, one of the most common measuring instruments and is distinguished by its versatility, high accuracy.

Figure 2. Pieces of coal between 13–28 mm

Determination of the mass of the coal fraction in granulometric composition was performed using electronic scales (maximum load — 1000 g; discreteness 0,001 g). *d* — in the table is the average diameter of the coal fraction, mm; *m* is the average mass of the sorted coal fractions, g.

Table 1

Granulometric composition of the original product and mass of sorted pieces

Coal fragments №	*d*, mm	*m*, g	Coal fragments №	*d*, mm	*m*, g
1	13–28	7.326	26	13–28	6.265
2		7.727	27		7.827
3		6.215	28		6.443
4		6.412	29		6.892
5		6.947	30		7.364
6		8.768	31		7.767
7		6.037	32		6.095
8		7.044	33		6.564
9		7.330	34		8.028
10		7.181	35		6.934
11		6.166	36		6.362
12		6.355	37		8.146
13		7.163	38		7.861
14		7.889	39		7.384
15		8.762	40		7.576
16		8.282	41		8.343
17		7.273	42		8.124
18		8.937	43		7.565
19		7.099	44		8.129
20		6.129	45		6.662
21		6.902	46		6.433
22		6.831	47		6.927
23		7.917	48		8.851
24		6.761	49		7.744
25		6.386	50		6.583

In the work, the sorting of coal fractions in the range of 13–28 mm allows you to determine the yield of the finished product after grinding the studied raw materials in electric pulse technology, select electrical and geometric parameters of the material processing technology, design the structure of the disassembly and grinding device. The mass of the coal fractions was assumed to be approximately the same before processing.

Results and Discussion

For the design of the working channel electrode system, various options for electrodes were considered. The negative electrode was offered in variants such as:

– sole of the inner surface of the working channel made of steel;

– negative electrode height h = 4 mm, diameter d = 10 mm;

– negative electrode height h = 8 mm, diameter d = 10 mm.

The tests were performed at the following parameters: pulsed capacitor capacity C = 0.4 μF; pulsed discharges formed in the air converter interval voltage U = 25 kV, number of pulsed discharges N = 1000 discharges (Fig. 3).

After coal crushing works by the electric pulse method, the crushed raw materials were separated from the water and dried. The granulometric composition of coal powder was determined by Standard sieves according to GOST 12536-2014 “Methods for laboratory determination of Granulometric and micro-unit composition”. The yield of the finished product was calculated as follows: $K = (m/M)$. 100 %, where M is the mass of the primary raw material, m is the mass of the powder material obtained by the electric pulse method). The mass of the initial raw materials was constant for each experiment (M = 100 g).

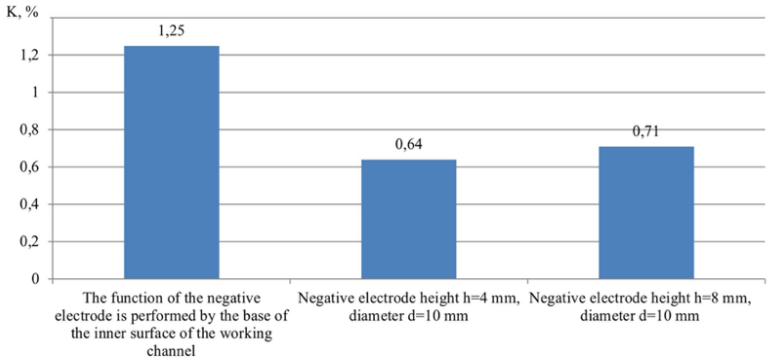

0,02<D<0,04 mm

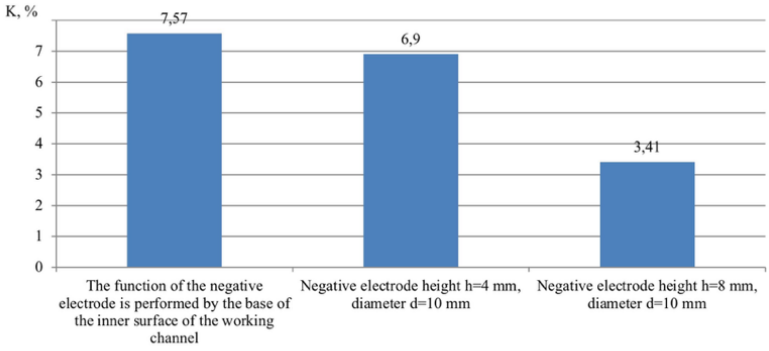

0,04<D<0,06 mm

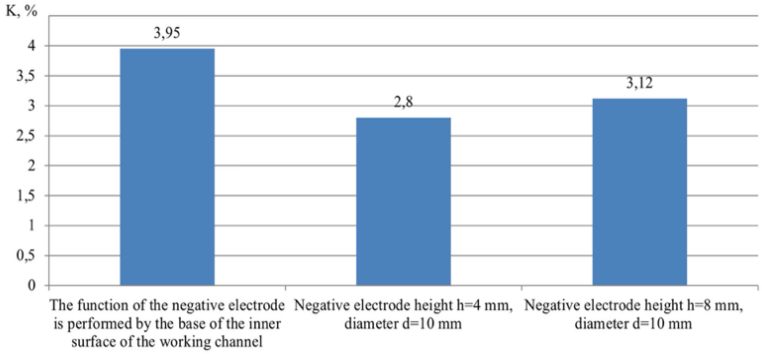

0,06<D<0,1 mm

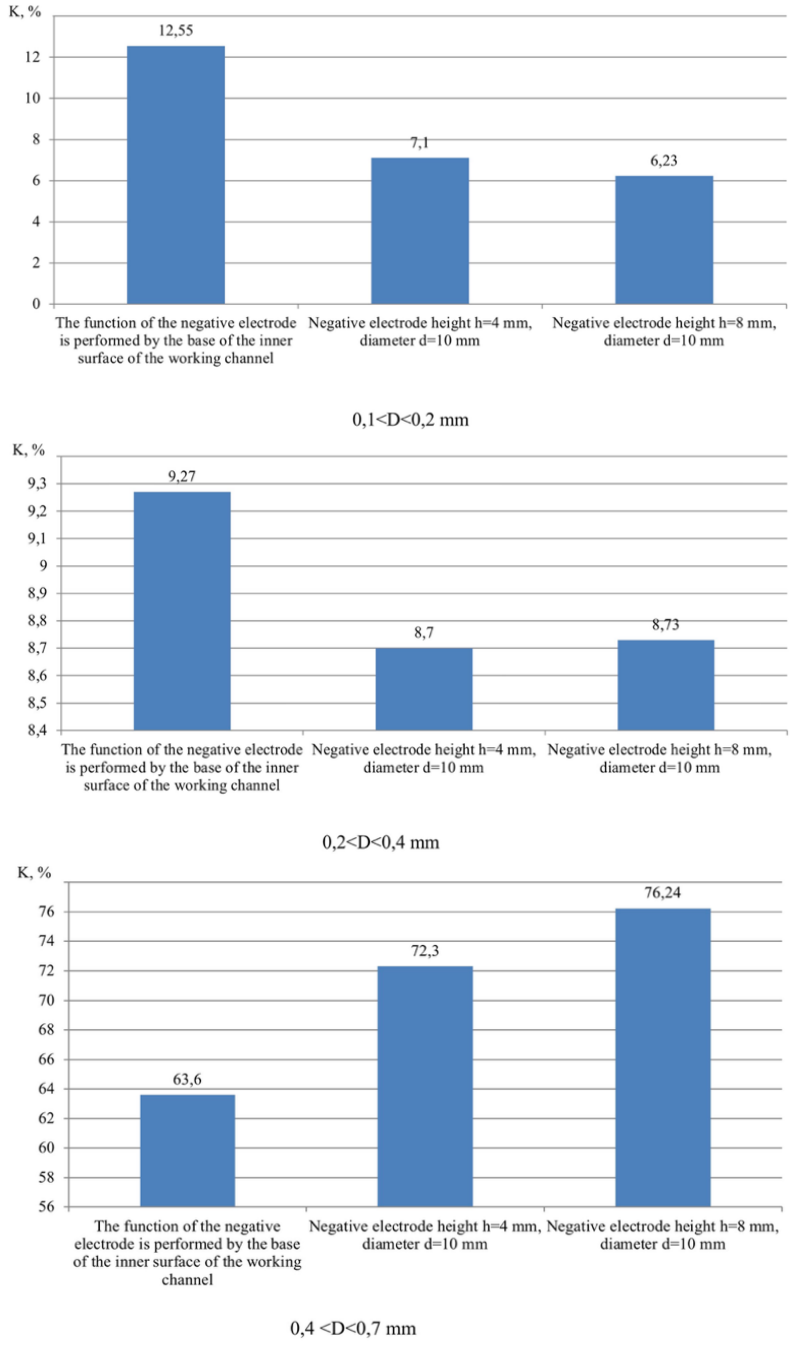

Figure 3. The output of the finished product, which depends on the type of negative electrode in the working channel for crushing coal by the method

From the results of the research, it follows that the yield of the smallest product ($0.02 < D < 0.04$ mm) when the base of the inner surface of the working channel performed the negative electrode function was 1.25 %, for the largest product ($0.4 < D < 0.7$ mm) — 63.6 %. When the negative electrode function was performed by a metal rod with a height of $h = 4$ mm $d = 10$ mm, the smallest coal yield was 0.64 %, the largest — 72.3 %. When increasing the height of the negative electrode $h = 8$ mm, these indicators changed at intervals as follows: 0.71 % for coal powder $0.02 < D < 0.04$ mm, 76.24 % for coal powder $0.4 < D < 0.7$ mm.

Experimental studies show that the configuration of the electrodes is important for the formation of favorable discharges in an environment consisting of a mixture of water and coal. In particular, when creating such a discharge, the active area of the positive electrode is minimized, and the active area of the negative electrode is increased. Such a circuit makes it possible to develop long and extensive electrical circuits—the

so-called ultra-long discharges between the electrodes. The basic idea is that by reducing the active part of the positive electrode (that is, the part where direct contact with the liquid occurs) and simultaneously increasing the area of the negative electrode, conditions are created to maintain a stable long discharge. This change allows the discharge to "germinate" over long distances inside the liquid, and also promotes the formation of thin luminous channels called streamers. These processes make it possible to form discharges with a long length and a significant channel area capable of intensively releasing energy into the surrounding space [11, 15–17].

Conclusion

Coal was crushed under the influence of electric pulse discharges, and the granulometric composition of the resulting powdered product was analyzed. The yield of the finished product was determined and the coal grinding was studied depending on the type of electrode in the working channel for coal grinding using the electric pulse method. According to experimental data, it was found that using the bottom of the inner surface of the working channel as a negative electrode increases the yield of the finished product with a powder diameter from $D < 0.04$ mm to $D < 0.2$ mm. At the same time, a decrease in the amount of coal powder with a diameter of 0.4 mm $< D <$ 0.7 mm was observed. The results obtained made it possible to choose the optimal version of the electrode system in the working channel for grinding raw materials using the electric pulse method. Analysis of experimental data has shown that the intensity of grinding of raw materials can be increased using the proposed electrode system. The results of the study can be used in the design of new types of devices that improve the energy efficiency of the technology of electric pulse processing of natural raw materials.

Acknowledgements

This research was funded by the Science Committee of the Ministry of Science and Higher Education of the Republic of Kazakhstan (Grant No. AP23488837).

References

1 Ходаков Г.С. Водоугольные суспензии в энергетике / Г.С. Ходаков // Теплоэнергетика. — 2007. — № 1. — С. 35–45.

2 Серант Ф.А. Приготовление водоугольного топлива и технологии его сжигания / Ф.А. Серант, А.И. Цепенок, Ю.В. Овчинников, С.В. Луценко, Е.Г. Карпов // Современная наука: исследования, идеи, результаты, технологии. — 2011. — Т. 1(6). — Р. 95–101.

3 Ильин А.К. О дисперсном составе водотопливных эмульсий / А.К. Ильин, Р.А. Ильин, Т.Р. Горбанов // Известия вузов. Проблемы энергетики. — 2012. — № 11-12. — С. 33–40.

4 Зайденберг В.Е. Производство и использование водо-угольного топлива / В.Е. Зайденберг, К.Н. Трубецкой, В.И. Мурко, И.Х. Нехороших. — 2001. — М.: Академия горных наук. — 176 с.

5 Ризун А.Р. Разработка и внедрение электроразрядного процесса дезинтеграции компонентов водно-угольного топлива / А.Р. Ризун, Ю.В. Голень, Т.Д. Денисюк, В.Ю. Кононов // Наука та інновації. — 2009. — Т. 5. — С. 42–46.

6 Курец В.И. Электроразрядные технологии обработки и разрушения материалов / В.И. Курец, М.А. Соловьев, А.И. Жучков, А.В. Барская. — Томск: Томский политехнический университет, 2012. — 272 с.

7 Chornyi V. Investigation of particle size distribution of grinded amber by electropulse discharges in a liquid medium / V. Chornyi, Y. Kharchenko, T. Mysiura, N. Popova, V. Zavialov // Archive of mechanical engineering. — 2021. — No. 68(3). — P. 337–348.

8 Усов А.Ф. Опыт разработки средств электроимпульсной дезинтеграции материалов / А.Ф. Усов, В.А. Цукерман, В.И. Курец // Горный информационно-аналитический бюллетень (научно-технический журнал). — 2011. — № 12. — С. 310–318.

9 Khassenov A.K. Development of Electrode of Electric Impulse Chamber for Coal Grinding / A.K. Khassenov, D.Z. Karabekova, M.M. Bolatbekova, A.S. Kudussov, S.S. Kassymov, L.V. Chirkova // Appl. Sci. — 2025. — 15(7). — P. 3607. https://doi.org/10.3390/app15073607

10 Khassenov, A. Development of an Electric Pulse Device for Coal Grinding / A. Khassenov, D. Karabekova, M. Bolatbekova, B. Nussupbekov, P. Kissabekova, R. Orazbayev // Appl. Sci. — 2025. — No. 15(10). — P. 5548. https://doi.org/10.3390/app15105548

11 Юткин Л.А. Электрогидравлический эффект и его применение в промышленности / Л.А. Юткин. — Ленинград, 1986. — 253 с.

12 Shaimerdenova K. Electrohydropulse method for destruction of natural minerals / K. Shaimerdenova, B. Nussupbekov, G. Bulkairova, M. Stoev, A. Khassenov, D. Karabekova // Bulgarian Chemical Communications. — 2020. — Vol. 52. — Iss. A. — P. 185–187. https://bcc.bas.bg/BCC_Volumes/Volume_52_Special_A_2020/BCC-52-A-2020-185-187-Khassenov-192.pdf

13 Nussupbekov B.R. Coal pulverization by electric pulse method for water-coal fuel / B.R. Nussupbekov, A.K. Khassenov, D.Zh. Karabekova, U.B. Nussupbekov, M. Stoev, M.M. Bolatbekova // Bulletin of the University of Karaganda — Physics. — 2019. — № 4(96). — P. 80–84. https://doi.org/10.31489/2019ph4/80-84

14 Kurytnik I.P. Development of a grinding device for producing coal powder-raw materials of coal-water fuel / I.P. Kurytnik, A.K. Khassenov, D.Z. Karabekova, U.B. Nussupbekov, B.R. Nussupbekov, M. Bolatbekova // Archive of Mechanical Engineering. — 2022. — 69(2). — P. 259–268. https://doi.org/10.31489/2023PH2/93-99

15 Корженевский С.Р. Выбор режимов электрогидравлического селективного дробления кварцевой руды / С.Р. Корженевский, В.А. Бессонова, А.А. Комарский, В.А. Мотовилов, А.С. Чепусов // Физико-технические проблемы разработки полезных ископаемых. — 2016. — № 3. — С. 70–74.

16 Ситников А.В. Формирование разрядного импульса в системах на базе электрогидравлического эффекта / А.В. Ситников, И.А. Ситников, И.А. Швецов, А.Ю. Курбатов // Радиостроение. — 2018. — № 01. — С. 9–28.

17 Усов А.Ф. Перспективы технологий разрушения горных пород и руд / А.Ф. Усов // Известия РАН. Энергетика. — 2001. — №1. — С. 54–62.

А.К. Хасенов, Д.Ж. Карабекова, М.М. Болатбекова,
Р. Оразбаев, Л.В. Чиркова, Р.М. Сеитов

Көмір-су отыны шикізатын алудың электримпульсті қондырғысы жұмыс арнасының электродтық жүйесін жобалау

Мақалада көмір-су отынының шикізатын алу үшін көмірді ұнтақтаудың электримпульсті әдісін қолдану қарастырылды. Көмір-су отынының жану тиімділігі көбінесе оның гранулометриялық құрамымен анықталады, оның қалыптасуы дәстүрлі түрде механикалық диірмендерді қолдану арқылы жүзеге асырылады. Кең таралғанына қарамастан, мұндай қондырғылар жоғары энергия сыйымдылығымен, жұмыс бөліктерінің қарқынды тозуымен және айтарлықтай пайдалану шығындарымен сипатталады. Осыған байланысты көмірді дезинтеграциялаудың балама әдісі ретінде электримпульсті разрядтарды қолдану ерекше қызығушылық тудыруда. Жұмыста жергілікті микрожарылыстарды, соққы толқындарын және материал құрылымының бұзылуын тудыратын қысқа мерзімді жоғары вольтты разрядтардың әсеріне негізделген электримпульсті ұсақтаудың физикалық негіздері талданды. «Көмір-су» гетерогенді ортасында орналасатын электримпульсті қондырғының электродтық жүйесіне, сондай-ақ материалдарды таңдауға, электродтардың геометриясына және разряд параметрлеріне ерекше назар аударылды. Тәжірибелік электримпульсті қондырғының құрылымы және оның жұмыс принципі сипатталды. Зерттеудің мақсаты минималды энергетикалық шығындармен және жабдықтың сенімділігін арттыра отырып, көмір-су отынының шикізатын алу үшін электримпульсті қондырғының жұмыс арнасының электрод жүйесінің тиімді нұсқасын негіздеу және әзірлеу. Жұмыс арнасының ішкі бетін теріс электрод ретінде пайдаланған кезде ұнтақ диаметрі $D < 0{,}04$ мм-ден $D < 0{,}2$ мм-ге дейінгі дайын өнімнің шығымы артатыны анықталды. Сондай-ақ, диаметрі $0{,}4$ мм $< D < 0{,}7$ мм көмір ұнтағының мөлшерінің азаюы байқалды. Алынған нәтижелер шикізатты электроимпульсті әдіспен ұнтақтау кезінде жұмыс арнасындағы электродтар жүйесінің оңтайлы нұсқасын таңдауға мүмкіндік берді.

Кілт сөздер: электримульсті разряд, жоғары вольтты разряд, шикізат, көмір-су отыны, жұмыс электроды, көмір ұнтағы, дезинтеграция, разряд кернеуі, дайын өнім шығымы, көмір-су отынының шикізаты

А.К. Хасенов, Д.Ж. Карабекова, М.М. Болатбекова,
Р. Оразбаев, Л.В. Чиркова, Р.М. Сеитов

Проектирование электродной системы рабочего канала электроимпульсной установки для получения сырья угольно-водяного топлива

В статье рассматривается применение электроимпульсного метода измельчения угля для получения сырья угольно-водяного топлива. Отмечено, что эффективность сгорания угольно-водяного топлива во многом определяется его гранулометрическим составом, формирование которого традиционно осуществляется с использованием механических мельниц. Несмотря на широкое распространение, такие установки характеризуются высокой энергоёмкостью, интенсивным износом рабочих органов и значительными эксплуатационными затратами. В связи с этим особый интерес представляет использование электроимпульсных разрядов как альтернативного способа дезинтеграции угля. В работе проанализированы физические основы электроимпульсного измельчения, основанные на воздействии

кратковременных высоковольтных разрядов, вызывающих локальные микровзрывы, ударные волны и разрушение структуры материала. Особое внимание уделено электродной системе электроимпульсной установки, функционирующей в гетерогенной среде «уголь–вода», а также выбору материалов, геометрии электродов и параметров разряда. Описана конструкция экспериментальной электроимпульсной установки и принцип её работы. Целью исследования является обоснование и разработка эффективного варианта электродной системы рабочего канала электроимпульсной установки для получения сырья угольно-водяного топлива с минимальными энергетическими затратами и повышенной надёжностью оборудования. Установлено, что при использовании внутренней поверхности рабочего канала в качестве отрицательного электрода увеличивается выход готового продукта диаметром порошка от $D < 0{,}04$ мм до $D < 0{,}2$ мм. Также отмечено уменьшение размеров угольного порошка диаметром 0,4 мм $< D <$ 0,7 мм. Полученные результаты позволили выбрать оптимальный вариант системы электродов в рабочем канале при измельчении сырья электроимпульсным методом.

Ключевые слова: электроимульсный разряд, высоковольтный разряд, сырье, угольно-водяное топливо, рабочий электрод, угольный порошок, дезинтеграция, напряжение разряда, выход готового продукта, сырье угольно-водяного топлива

References

1 Khodakov, G.S. (2007). Vodougolnye suspenzii v energetike [Coal-water suspensions in power engineering]. *Teploenergetika — Thermal Power Engineering,* 1, 35–45 [in Russian].

2 Serant, F.A., Tsepenok, A.I., Ovchinnikov, Yu.V., Lutsenko, S.V., & Karpov, E.G. (2011). Prigotovlenie vodougolnogo topliva i tekhnologii ego szhiganiia [Preparation of water–coal fuel and technologies for its combustion]. *Sovremennaia nauka: issledovaniia, idei, rezultaty, tekhnologii — Modern Science: Research, Ideas, Results, Technologies*, *1*(6), 95–101 [in Russian].

3 Ilyin, A.K., Ilyin, R.A., & Gorbanov, T.R. (2012). O dispersnom sostave vodotoplivnykh emulsii [On the dispersed composition of water–fuel emulsions]. *Izvestiia vuzov. Problemy energetiki — Proceedings of Higher Educational Institutions. Problems of Power Engineering,* 11-12, 33–40 [in Russian].

4 Zaydenberg, V.E., Trubetskoy, K.N., Murko, V.I., & Nekhoroshikh, I.Kh. (2001). *Proizvodstvo i ispolzovanie vodo-ugolnogo topliva* [Production and use of water–coal fuel]. Moscow: Akademiia gornykh nauk [in Russian].

5 Rizun, A.R., Goleny, Yu.V., Denisyuk, T.D., & Kononov, V.Yu. (2009). Razrabotka i vnedrenie elektrorazriadnogo protsessa dezintegratsii komponentov vodno-ugolnogo topliva [Development and implementation of the electrical discharge process for disintegration of water–coal fuel components]. *Nauka i innovatsii — Science and Innovations*, *5*, 42–46 [in Russian].

6 Kurets, V.I. Solovyev, M.A., Zhuchkov, A.I., & Barskaya, A.V. (2012). *Elektrorazriadnye tekhnologii obrabotki i razrusheniia materialov* [Electrical discharge technologies for processing and destruction of materials]. Tomsk: Tomskii Politechnicheskii Universitet [in Russian].

7 Chornyi, V., Kharchenko, Y., Mysiura, T., Popova, N., & Zavialov V. (2021). Investigation of particle size distribution of grinded amber by electropulse discharges in a liquid medium. *Archive of mechanical engineering*, 68(3), 337–348.

8 Usov, A.F., Tsukerman, V.A., & Kurets, V.I. (2011). Opyt razrabotki sredstv elektroimpulsnoi dezintegratsii materialov [Experience in the development of electrical–pulse material disintegration methods]. *Gornyi informatsionno-analiticheskii biulleten (nauchno-tekhnicheskii zhurnal) — Mining Information and Analytical Bulletin (scientific–technical journal),* 12, 310–318 [in Russian].

9 Khassenov, A.K., Karabekova, D.Z., Bolatbekova, M.M., Kudussov, A.S., Kassymov, S.S., & Chirkova, L.V. (2025). Development of Electrode of Electric Impulse Chamber for Coal Grinding. *Appl. Sci., 15*(7), 3607. https://doi.org/10.3390/app15073607

10 Khassenov, A., Karabekova, D., Bolatbekova, M., Nussupbekov, B., Kissabekova, P., & Orazbayev, R. (2025). Development of an Electric Pulse Device for Coal Grinding. *Appl. Sci.,* 15(10), 5548. https://doi.org/10.3390/app15105548

11 Yutkin, L.A. (1986). *Elektrogidravlicheskii effekt i ego primenenie v promyshlennosti* [Electrohydraulic effect and its application in industry]. Leningrad [in Russian].

12 Shaimerdenova, K., Nussupbekov, B., Bulkairova, G., Stoev, M., Khassenov, A., & Karabekova, D. (2020). Electrohydropulse method for destruction of natural minerals. *Bulgarian Chemical Communications, 52*(A), 185–187. https://bcc.bas.bg/BCC_Volumes/Volume_52_Special_A_2020/BCC-52-A-2020-185-187-Khassenov-192.pdf

13 Nussupbekov, B.R., Khassenov, A.K., Karabekova, D.Zh., Nussupbekov, U.B., Stoev, M., & Bolatbekova, M.M. (2019). Goal pulverization by electric pulse method for water-coal fuel. *Bulletin of the University of Karaganda-Physics,* 4(96), 80–84. https://doi.org/10.31489/2019ph4/80-84

14 Kurytnik, I.P., Khassenov, A.K., Karabekova, D.Z., Nussupbekov, U.B., Nussupbekov, B.R., & Bolatbekova, M. (2022). Development of a grinding device for producing coal powder-raw materials of coal-water fuel. *Archive of Mechanical Engineering*, 69(2), P. 259–268. https://doi.org/10.31489/2023PH2/93-99

15 Korzhenevsky, S.R., Bessonova, V.A., Komarsky, A.A., Motovilov, V.A., & Chepusov A.S. (2016). Vybor rezhimov elektrogidravlicheskogo selektivnogo drobleniia kvartsevoi rudy [Selection of modes for electrohydraulic selective crushing of quartz ore]. *Fiziko-tekhnicheskie problemy razrabotki poleznykh iskopaemykh — Physical–Technical Problems of Mineral Resource Development,* 3, 70–74 [in Russian].

16 Sitnikov, A.V., Sitnikov, I.A., Shvetsov, I.A., & Kurbatov, A.Yu. (2018). Formirovanie razriadnogo impulse v sistemakh na baze elektrogidravlicheskogo effekta [Formation of discharge pulse in systems based on the electrohydraulic effect]. *Radiostroenie — Radiostructure,* 01, 9–28 [in Russian].

17 Usov, A.F. (2001). Perspektivy tekhnologii razrusheniia gornykh porod i rud [Prospects of technologies for rock and ore destruction]. *Izvestiia Rossiiskoi akademii nauk. Energetika — Proceedings of the Russian Academy of Sciences. Energy,* 1, 54–62 [in Russian].

Information about the authors

Khassenov, Ayanbergen — PhD, Professor, Buketov Karaganda National Research University, Karaganda, Kazakhstan; e-mail: ayanbergen@mail.ru; ORCID ID: https://orcid.org/0000-0002-5220-9469

Karabekova, Dana (*corresponding author*) — PhD, Professor, Buketov Karaganda National Research University, Karaganda, Kazakhstan; e-mail: karabekova71@mail.ru; ORCID ID: https://orcid.org/0000-0001-8776-4414

Bolatbekova, Madina — MSc (Physics), Senior Lecturer, Buketov Karaganda National Research University, Karaganda, Kazakhstan; e-mail: r.bolatbekova.madina@gmail.com; ORCID ID: https://orcid.org/0000-0002-0169-3430

Orazbayev, Rahman — Master Student, Buketov Karaganda National Research University, Karaganda, Kazakhstan.

Chirkova, Lyubov — Candidate of Technical Sciences, Buketov Karaganda National Research University, Karaganda, Kazakhstan; e-mail: lubov.chirkova.53@mail.ru, ORCID ID: https://orcid.org/0000-0002-5197-3875

Seitov, Ruslan — Senior Lecturer, Department of Transport and Logistics Systems, Buketov Karaganda National Research University, Karaganda, Kazakhstan; e-mail: ruslanekb71@gmail.com, ORCID ID: https://orcid.org/0000-0002-8957-1453